Mechanical Approach to Active Matter: Reverse Osmotic Effect and Motility-Induced Phase Separation

Thesis by
Hyeongjoo Row

In Partial Fulfillment of the Requirements for the
Degree of
Doctor of Philosophy

CALIFORNIA INSTITUTE OF TECHNOLOGY
Pasadena, California

2022
Defended May 13, 2022

Hyeongjoo Row
ORCID: 0000-0003-3623-512X

ACKNOWLEDGEMENTS

I would like to express my sincere gratitude to the amazing people I met during my journey at Caltech. First, I cannot express my gratitude enough to my thesis advisor Prof. John Brady and Prof. Zhen-Gang Wang, who had co-advised me throughout the most of my graduate study. I am privileged to have had the opportunity to learn from and work with both John and Zhen-Gang who imparted their unique perspectives to me. Aside from John and Zhen-Gang's exceptional scientific guidance, illuminating lectures, and unbelievable physical insights, I deeply appreciate them most for their respect, trust, and encouragement in offering me intellectual freedom. I thank John especially for his generosity with his time. Before the COVID-19 pandemic broke out, I was always welcome to visit John's office and even spend even several hours discussing science with him, which was invaluable training for me.

I would like to thank the members of my thesis committee: Prof. Mikhail Shapiro and Prof. Matt Thomson. I thank Prof. Mikhail Shapiro for his committee service and hospitality whenever I run into him on the campus. He generously offered access to his laboratory to experimentally verify my theoretical work, which regretfully I did not have enough time to. I also learned much about communication skills by watching him ask thoughtful and critical questions at the end of almost every seminar. I also thank Prof. Matt Thomson for his committee service and valuable scientific advice. Prof. Thomson's inspiring works on active matter systems made me think about the practical applications of my works.

I would like to thank the Chemical Engineering Staff. I thank Allison Kinard, Martha Hepworth, Sohee Lee, and Kathy Bubash for their hospitality to make me feel like home at Spalding and also for their administrative assistance throughout my time at Caltech. I thank Suresh Guptha for managing the computational resources of the Brady group and Wang group.

My time in Brady group and Wang group was vastly more enjoyable thanks to the members and visitors: Dr. Stewart Mallory, Dr. (Edmond) Tingtao Zhou, Dr. Kevin Marshall, Dr. Eric Burkholder, Dr. Austin Dulaney, Dr. Camilla Kjeldberg, Zhiwei Peng, Dr. Pengfei Zhang, Dr. Jian Jiang, Dr. Huikuan Chao, Dr. Chang Yun Son, Dr. Sriteja Mantha, Dr. Yasemin Basdogan, Dr. Shensheng Chen, Dr. Xuepeng Wang, Dr. Kevin Shen, Dr. Ahmad Omar, Andy Ylitalo, Chris Balzer, Linghui

Wang, Dorian Bruch, Alec Glisman, Benjamin Ye, Alexandros Tsamopoulos, Sam Varner, Pierre Walker, Dr. Frank Bates, Dr. Gwynn Elfring, Dr. Karol Makuch, Dr. Mario Sandoval, Dr. Tyler Ross, Dr. Zengju Lian, and Dr. Leying Qing. I owe special thanks to Stew and Ahmad, who were always sources of guidance, advice, and laughs. Zhiwei was an amazing office mate and I really enjoyed countless productive discussions with him. Adventures to nearby cities with Dorian, Ben, Sam, and Edmond were unforgettable moments in my time at Caltech. There were so many memorable moments with these amazing people that I cannot list all of them here.

Life at Caltech would not have been the same without my friends and classmates, including Jin Mo Koo and Seungkyeum (Sean) Kim. I would like to make a special note to thank Dr. Yoon Woo Lee and Dr. In Seok Kang, who encouraged and helped me to start my journey to Caltech by sharing their invaluable stories. I would also like to express my gratitude for the Kwanjung Educational Foundation, which supported me with scholarship during my graduate study.

Most importantly, I would like to thank my family in Korea for their love and support. My parents and grandmother have made enormous sacrifices throughout my life and have always been supportive of all the decisions I have made throughout my academic career. My brother has been my great supporter as well. I would also like to thank my mother-in-law for her tremendous support and for welcoming me into her family.

I owe all of my accomplishments at Caltech to my wife Yoon Hee Lee. Thank you for your love and support in following me to the US even without fluent English while leaving family and friends back in Korea, just to be with me. Words cannot express my gratitude and appreciation.

ABSTRACT

The defining feature of active matter, self-propulsion requires constant consumption of energy to be maintained. As a result, active matter systems are inherently out of equilibrium and some principles that are accepted as common knowledge, particularly from thermodynamics, do not apply to the active matter systems. Arguably the most popular example is the motility-induced phase separation (MIPS) – active matter can spontaneously phase separate into liquid-like dense phase and gas-like sparse phase even without any attractive interactions between the self-propelling constituents. In this thesis, I demonstrate the utility of a mechanical perspective in revealing and understanding the underlying physics of seemingly confounding behaviors of active matter systems. In Chapters 2 and 3, I consider the mechanics of a suspension of active colloidal particles when the transport properties (self-propelling speed and diffusivities) vary spatially. The mechanical analysis reveals the reverse-osmotic nature of active matter systems with a spatial variation in activity. I provide an explanation for why physical processes governed by the osmotic pressure of particles can appear in a reversed manner in active matter systems, e.g. a fluid can flow from regions of high concentration to low in a suspension of active colloids. In Chapter 4, I develop a mechanical theory of phase coexistence that applies to both equilibrium and nonequilibrium systems. By applying the mechanical theory to MIPS, I find phase coexistence conditions of the MIPS that allow a construction of a phase diagram, which excellently agrees with the results from computer simulations. The mechanical theory also allows access to the microscopic structure of phase interfaces. By investigating the interfacial structure, I discover interesting nonequilibrium interfacial behavior of the MIPS. I find that the width of the MIPS interface varies nonmonotically with the activity of particles and provide a mechanical explanation for the phenomena.

PUBLISHED CONTENT AND CONTRIBUTIONS

[1] H. Row and J. F. Brady, "Reverse osmotic effect in active matter," *Physical Review E*, vol. 101, no. 6, p. 062 604, 2020. DOI: 10.1103/PhysRevE.101.062604,
H.R. participated in the conception of the project, performed the calculations, analyzed the data, and participated in the writing of the manuscript.

TABLE OF CONTENTS

Acknowledgements . . . iii
Abstract . . . v
Published Content and Contributions . . . vi
Table of Contents . . . vi
List of Illustrations . . . viii
Chapter I: Introduction . . . 1
1.1 Active Matter Systems . . . 1
1.2 Active Brownian Particles . . . 2
1.3 Mechanics of Active Suspensions . . . 4
1.4 Thesis Outline . . . 7
Chapter II: Active Matter with Spatially Varying Transport Properties . . . 13
2.1 Introduction . . . 13
2.2 Infinite Active Suspensions . . . 14
2.3 Active Suspensions Confined by Planar Walls . . . 23
2.4 Active Suspensions Confined by a Circular Wall . . . 28
2.5 Transient Behavior of Microswimmers with Abrupt Variation in Activity . . . 32
2.6 Conclusions . . . 37
2.7 Appendix: Brownian Dynamics Simulations of Active Brownian Particles . . . 38
Chapter III: Reverse Osmotic Effects in Active Matter . . . 42
3.1 Particle Phase Pressure on Walls . . . 42
3.2 Mechanical Description of Active Matter with Spatially Varying Activity . . . 43
3.3 Reverse Osmotic Effect in Active Matter . . . 46
3.4 Reverse Diffusiophoresis in Active Bath . . . 47
3.5 Conclusions . . . 52
Chapter IV: Mechanical Theory of Phase Coexistence . . . 55
4.1 Phase Equilibrium Conditions . . . 55
4.2 Microscopic Structure of Phase Interfaces . . . 59
4.3 Mechanical Description of Phase Interfaces . . . 63
4.4 Motility-Induced Phase Separation . . . 67
4.5 Conclusions . . . 76
4.6 Appendix: Classical Density Functional Theory . . . 78
4.7 Appendix: Orientational Moment Equations of Interacting Active Brownian Particles . . . 81
4.8 Appendix: Effects of Correlation between Collisional Stress and Orientation . . . 89

LIST OF ILLUSTRATIONS

Number *Page*

2.1 A schematic of an infinite suspension of ABPs with an abrupt change in activity. In regions 1 ($x < 0$) and 2 ($x \geq 0$) the ABPs have swim speeds U_i, translational diffusivities D_{Ti}, and rotational diffusivities D_{Ri}, where the subscript i (= 1 or 2) represents the index of a region. 15

2.2 Color map of $n^{+\infty}/n^{-\infty}$ for $U_2/U_1 = 5$. The modified Péclet numbers $C_i = 0$ when $Pe_i = 0$ and $C_i \to 1$ when $Pe_i \to \infty$. The black line represents the case when diffusivities are the same in the two regions. When activities in both regions are high ($C_1,\ C_2 \approx 1$), $n^{+\infty}/n^{-\infty} \approx U_1/U_2 = 0.2$ i.e. nU = constant. If either of the two regions is diffusion-dominated ($C_i \approx 0$), the number density becomes constant throughout the whole suspension: $n^{+\infty} = n^{-\infty}$. 17

2.3 (a) Number densities scaled with the overall number density $\langle n \rangle$, (b) the product of the number density and swim speed scaled with the overall number density and the harmonic mean of the swim speeds ($U_h = 2(U_1^{-1} + U_2^{-1})^{-1}$), and (c) polar orders scaled with the overall number density versus the position x scaled with the run length in the region 2 $\ell_2 = U_2/D_{R2}$ when the swim speed abruptly changes at $x = 0$: $U_1/U_2 = 2$, $D_{T1} = D_{T2}$, and $D_{R1} = D_{R2}$. The translational diffusivity D_T is systematically changed to show the effect of the Brownian motion. Markers are BD simulations and solid lines are the analytic solutions of eqs. (2.5)-(2.8) with $\boldsymbol{Q} = \mathbf{0}$ ((2.9)-(2.14)). . . 18

2.4 Relative magnitude of the nematic order Q_{xx} compared to the number density n as a function of the position x scaled with the run length in the region 2 $\ell_2 = U_2/D_{R2}$ obtained by BD simulations. The swim speed abruptly changes at $x = 0$ so that $U_1/U_2 = 2$, $D_{T1} = D_{T2}$, and $D_{R1} = D_{R2}$. The translational diffusivity D_T is systematically changed to show the effect of the Brownian motion. When $Pe < 100$ the nematic order is three orders of magnitude smaller than the number density allowing the simple closure $\boldsymbol{Q} = \mathbf{0}$ to result in the highly accurate analytical solution. 19

2.5 (a) Number densities and (b) polar orders scaled with $\langle n \rangle$. Black dashed line represents the analytical solution obtained by the $\boldsymbol{Q} = \boldsymbol{0}$-closure ((2.9)-(2.14)) and the other lines are obtained by solving the full Smoluchowski equation with the finite element method. The position x is scaled with the run length ℓ_2 in region 2. In region 1 ($x < 0$), $Pe = 2$ and in region 2 ($x \geq 0$), $Pe = 1$. The number density changes only when there exists variation of swim speed. 20

2.6 (a) Number densities and (b) polar orders scaled with the overall number density $\langle n \rangle$ versus the position x scaled with the microscopic length in region 1 $\delta_1 = \sqrt{D_{T1}/D_{R1}}$ in 2D. Particles are active ($Pe_1 = 10$) in region 1 and the transnational diffusivity is the same in the two regions. When both regions are active (blue), the number density is nearly constant even though swim speeds in the two regions differ ($U_1/U_2 = 10$) due to the passive-like ($Pe_2 = 10^{-4}$) character in region 2. When particles are not active in region 2 (black) the number density abruptly jumps at the boundary. The global Péclet number $Pe_{1,2} = U_1^2/(2D_{T2}D_{R2}) = 5$ in the passive region. Markers are BD simulations and solid lines are the analytic solutions ((2.16)-(2.23)). 22

2.7 A schematic of a suspension of ABPs with an abrupt change in activity bounded between two parallel planar walls. In regions 1 ($-L_1 \leq x < 0$) and 2 ($0 \leq x \leq L_2$) the ABPs have swim speeds U_i, translational diffusivities D_{Ti}, and rotational diffusivities D_{Ri}, where the subscript i (= 1 or 2) represents the index of a region. 23

2.8 A schematic of the singular perturbation analysis with matched asymptotic expansions when the length of a region is much larger than the boundary-layer thickness $L_i \gg D_{Ti}/U_i$. Red lines represent the number density in boundary layers near the walls. The leading order solution insided the boundary layers has been obtained by Yan and Brady [15] for the number density of ABPs near a wall. The blue line represents the number density in the boundary layer where transport properties change. To leading order, the suspension can be treated as an infinite suspension with a step change in transport properties inside the boundary layer at $x = 0$. The number densities in the boundary layers are matched with number densities in the bulk, or outer regions, where the number density is constant to leading order. 25

2.9 (a) Number densities, (b) polar orders, and (c) nematic orders of ABPs confined between parallel walls when transport properties abruptly changes at $x = 0$. The number densities and polar orders are scaled with the overall number density $\langle n \rangle$ and the nematic orders are scaled with the local number densities: $Q_{xx}/n = \langle q_x^2 \rangle - 1/2$. Markers are BD simulations and lines are analytic solutions obtained by a singular perturbation analysis (2.33)-(2.36). In all cases, the two regions have the same translational and rotational diffusivities and length ($L/2$), but the swim speeds differ: $Pe_1/Pe_2 = (U_1/U_2)^2$. The coordinate x is scaled with L, which is 10 times longer than the microscopic length scale $\delta = \sqrt{D_T \tau_R}$. 27

2.10 A schematic of a suspension of ABPs with an abrupt change in activity bounded by a circular wall of radius R. In regions 1 ($r < \Delta R$; $0 < \Delta < 1$) and 2 ($\Delta R \leq r < R$) the ABPs have swim speeds U_i, translational diffusivities D_{Ti}, and rotational diffusivities D_{Ri}, where the subscript i (= 1 or 2) represents the index of a region. 29

2.11 (a) Number densities, (b) polar orders, and (c) nematic orders of ABPs confined by a circular wall when transport properties abruptly changes at $r = R/2$. The number densities and polar orders are scaled with the overall number density $\langle n \rangle$ and the nematic orders are scaled with the local number densities: $Q_{rr}/n = \langle q_r^2 \rangle - 1/2$. Markers are BD simulations and lines are analytic solutions obtained by a singular perturbation analysis ((2.44)-(2.48)). In all cases, the two regions have the same translational and rotational diffusivities, but the swim speeds differ: $Pe_1/Pe_2 = (U_1/U_2)^2$. The coordinate r is scaled with the radius of the container R, which is 25 times longer than the microscopic length scale $\delta = \sqrt{D_T \tau_R}$. 31

2.12 (Left) Snapshots from BD simulations of purely active particles released at $t = 0$ from the center (white dashed line) where the reorientation time or swim speed abruptly changes. The colormap shows the local number density of particles. The length of the simulation box is 5 times longer than the run length in region 1 ($x < 0$). (Right) Transient number densities, polar orders, and nematic orders multiplied by the run length in region 1 ℓ_1 obtained by BD simulations when purely active particles released at $t = 0$ from $x = 0$ where the reorientation time or swim speed abruptly changes. The probability density is normalized so that $\int_{-\infty}^{\infty} n\, dx = 1$ and the position is scaled with ℓ_1 as well. The shape of number densities shows transition from wave-like ($t \leq \tau_R$) to diffusion-like ($t > \tau_R$) dynamics. When a step change in the swim speed occurs the even-ordered orientational moments (e.g. n, $\boldsymbol{Q}$, etc.) are discontinuous at the jump for the continuity of the translational flux $\boldsymbol{j}_T = UP\boldsymbol{q}$. 34

2.13 The ratio of numbers of purely active particles in the two regions after randomly oriented particles are released at the interface of the two regions with different transport properties. Black and blue represent a step change in the reorientation time ($\ell_1/\ell_2 = \tau_{R,1}/\tau_{R,2}$) and the swim speed ($\ell_1/\ell_2 = U_1/U_2$), respectively. Markers are from BD simulations and lines are the analytical prediction $N_1/N_2 = \sqrt{\tau_{R,1}/\tau_{R,2}}$. In the BD simulations the numbers of particles are measured $\sim 3\tau_{R,1}$ after the release of particles to ensure the values have reached constant. 35

2.14 BD simulation results of transient (a) number densities, (b) polar orders, and (c) nematic orders multiplied by the local run length versus the position x scaled with the local run length when randomly oriented purely active particles are released from $x = 0$ at $t = 0$. The probability density is normalized so that $\int_{-\infty}^{\infty} n\, dx = 1$ and the reorientation time is the same in the two regions. Even though the swim speeds differ in the two regions, orientational moments of the rescaled density $A = PU$ are symmetric on the domain x/ℓ resulting in the even partitioning of particles. Furthermore, the rescaled solutions are independent of the swim speeds and fall on a single curve as predicted by eqs. (2.57)-(2.59). The style and color of markers represent the time and ratio of swim speeds U_1/U_2, respectively. . . 36

3.1 The ratio of the pressures exerted by ABPs on wall 1 ($z = -L_1$) and wall 2 ($z = L_2$) scaled with the ratio of corresponding run lengths when an active suspension is bounded by the two parallel walls as described in Fig. 2.7. The transport properties in the two regions are the same except for (a) the swim speed ($Pe_1/Pe_2 = U_1^2/U_2^2$) or (b) the rotational diffusivity ($Pe_1/Pe_2 = D_{R2}/D_{R1}$). The two regions have the same length ($L_1 = L_2$) and the distance between the walls $L = L_1 + L_2$ is 100 times longer than the microscopic length scale $\delta_2 = \sqrt{D_{T2}/D_{R2}}$ in region 2. Markers are from pressures directly measured from BD simulations and lines are from the analytical solution (2.33)-(2.36). In the both cases the ratio of pressures exerted by particles on the walls is ℓ_1/ℓ_2 when activity is high ($Pe \gg 1$).. . . 43

3.2 A schematic of a suspension of ABPs with an abrupt change in activity confined between two parallel planar walls (see Fig. 2.7 for detailed description of the system). The whole active suspension enclosed by the red dashed box is taken as a control volume. Since ABPs undergo a force-free motion, the net pressure on the left and right (or top and bottom) sides of the control volume must be identical to satisfy a macroscopic mechanical force balance. 44

3.3 (Left) A schematic of the pressure distributions. The pressure exerted by active particles $\Pi = nk_BT$ on a wall is larger in the region with the faster swim speed. Since the total pressure p in a force-free active suspension is constant for a mechanical force balance, the fluid pressure p_f is lower at the wall in the region with the faster swim speed generating a fluid pressure difference at the two walls Δp_f^w. (Right) A schematic of a novel pumping device powered by the activity of suspended particles. When two regions with different swim speeds are connected by a tube and the walls are semi-permeable membranes, the fluid pressure difference Δp_f^w will generate a flow of fluid from the slower to the faster region — from regions of high concentration to low! 46

3.4 A schematic of reverse diffusiophoresis in a bath of active hard-spheres. When the swim speed U_0 of highly active ($Pe \gg 1$) bath particles varies spatially, the number density is lower in the faster than in the slower region satisfying $nU_0 \approx$ constant. Due to the reverse osmotic behavior of active particles, the osmotic pressure at the contact surface $\Pi|_{S_c} \propto \ell_0$ is higher on the lower concentration side. The resulted phoretic motion is from regions of low concentration to high even though interparticle interactions are repulsive: the reverse diffusiophoresis. 49

3.5 The total osmotic force $\boldsymbol{F}^{osmo} = -\oint_{r=R_c} \Pi \boldsymbol{n}\, dS$ on a circular phoretic body fixed at $x = 0$ in a bath of purely active particles versus the linear swim speed gradient dU_0/dx of active bath particles. The osmotic force is scaled with the product of the swim force $\zeta U_0(0)$, background number density $n^\infty(0)$ at the center of the phoretic particle, and area pervaded by the phoretic particle and the swim speed gradient is scaled with the rotational diffusivity. The contact radius R_c is 10 times longer than the run length at the center $\ell_0(0)$. The results obtained by the BD simulations confirm Brady's prediction [7] of the reverse diffusiophoresis that the total osmotic force and hence the phoretic speed is linearly proportional to the swim speed gradient. . . 51

4.1 (a) A schematic description of the double-tangent construction on an isotherm in the diagram of the molar Helmholtz free energy $\overline{F}$ versus the molar volume v at a fixed temperature T. The points at contact with the common tangent line (blue) correspond to the coexisting phases. The slope and y-intercept of the common tangent represents the the coexistence pressure $(\partial\overline{F}/\partial v)_T = -p$ and the coexistence chemical potential $\overline{F} - v(\partial\overline{F}/\partial v)_T = \mu$. The red region of the curve indicates unstable region from the stability condition (4.5). (b) A schematic description of the Maxwell construction on an isotherm in the $p - v$ diagram. A horizontal line that cuts equal areas from the isotherm above (shaded blue) and below (shaded red) gives the coexistence pressure. The intersections of the horizontal line and isotherm correspond to the coexisting phases. The red region of the curve indicates unstable region from the stability condition (4.5). . . 57

4.2 (a) Generalized equal-area construction from the mechanical theory (eqs. (4.53) and (4.56)) in the $(\Pi^{act} = [\Pi^c + \Pi^{swim}]\,,\ \Pi^c)$ plane and (b) Maxwell construction for $\ell_0/D = 35 \times 2^{-1/6}$ in 2D. Pressures are normalized by $\zeta U_0/(\pi D)$. The shaded areas are visual guides for equal-area constructions. 72

4.3 Mechanical theory prediction for the phase behavior of active suspensions (solid line) compared with simulations (open circles). Here, $\ell_0/D = U_0\tau_R/D$ and $\phi = \pi D^2 n/4$, is the area fraction of active particles of diameter D. Also shown is the phase boundary from using a Maxwell construction (dotted line). 73

4.4 Interfacial profiles of the number density, polar order, and nematic order scaled by the volume of a particle $V_p = \pi D^3/6$ at the interface for $\ell_0/D = 50$ in 3D obtained by the a) Brownian Dynamics (BD) simulation and (b) mechanical theory. 74

4.5 Nonmonotonic trend of interfacial width w with activity ℓ_0/D obtained by the mechanical theory and the Brownian Dynamics simulations (inset). The interfacial width is scaled with the diameter of particles D and the reduced activity indicates the departure from the critical activity ℓ_0^{cr}/D, which is the minimum activity required to observe MIPS. 75

4.6 A schematic description of the nonmonotonic trend in the interfacial width in MIPS. For the mechanical force balance, the difference of the collisional pressures in two coexisting phases $\Delta\Pi^c$ is balanced by the self-generated swim force from the interface $\int \zeta U_0 m_z\ dz$. (a)→(b) For low activities, extra swim force required for increased collisional pressure difference can be obtained by aligning orientations of the particles at the interface toward the liquid-like phase. Consequently, the interface becomes more compact. (b)→(c) The swim force density per layer is bounded above by $\phi_0\zeta U_0$, i.e. every particle perfectly aligns toward the liquid-like phase, where ϕ_0 is the maximum packing fraction. To compensate huge difference in the collisional pressures in the two phases, more layer of particles are required and the interfacial width increases. 76

4.7 A schematic of Π^{act}-Π^{c} plot with a van-der Waals-like loop. The correlation between the collisional stress and orientation leads to $\int \Pi^{act} - \Pi^{act}_{coex}\, d\Pi^{c} > 0$ resulting in a drop in the coexistence active pressure. 90

4.8 Binodals obtained by the mechanical theory for MIPS in 3D with the stress-orientation correlation $\upsilon \nabla \cdot (\boldsymbol{\sigma}^{c} \boldsymbol{m}/n)$ included in the polar order flux. Here, υ is a parameter used to systematically control the weight of the correlation term in the in the flux. The correlation between the stress and orientation increases the width of the binodal as predicted. However, the widening effect saturates rapidly even at $\upsilon = 1$. 91

Chapter 1

INTRODUCTION

1.1 Active Matter Systems

It might be a human nature to relate the self-propelling motion to the life. When Brown reported his first observations of spontaneous random motions of pollen grains suspended in water in 1827 [1], he had to write another paper [2] in the following year to clarify that he did not intend to mean the pollen grains are alive or 'animated'. Thanks to Einstein's theory of Brownian motion [3], we now well-understand that the random motion observed by Brown is not a self-propelled motion but originates from the microscopic thermal motion of the suspending water molecules. Recent advances in material processes even allow non-living synthetic particles to self-propel [4–14]. Clearly, self-propulsion is not a unique feature of life.

Yet self-propulsion is still crucial in many living systems at a variety of length scales. Survival of many organisms depends on their motility [15]; fertilization requires progressive swimming of spermatozoa [16]; and motor proteins [17–19] and enzymes [20] self-propel inside a cell. Self-propulsion, which is the defining feature of active matter, is ubiquitously observed in living systems and this is one of the reasons why research interest in active matter systems has grown considerably over the past decade.

One of the main questions in the field of active matter research is about the consequences of self-propulsion. While active matter systems at large length scales exhibit fascinating collective phenomena such as flocking of birds, schooling of fish, cycloning of reindeer [21], and shimmering of bees [22], such behaviors result from complex interplay between motility and intellectual and/or social abilities [23]. Pure effects of self-propulsion can be more easily isolated and studied by considering active matter at a colloidal scale, such as motile bacteria and synthetic self-propelling colloids, which are not able to 'think'.

Active (colloidal) suspensions exhibit a number of intriguing behaviors: spontaneous directed motion of an asymmetric object immersed in an active suspension [24–28], self-enrichment of microswimmers in the presence of chevron-shaped structures [29–32], motility-induced phase separation (MIPS) [33–36], upstream

swimming [37–39], superfluidic flow without external forces [40, 41], etc. Surprisingly, some of these phenomena are against our intuitions gained from thermodynamics. For example, purely repulsive self-propelling particles can phase separate into gas- and liquid-like phases [34–36] — the so-called MIPS — while it is well-known that attractive interactions are essential for such phase separations in usual systems described by thermodynamics [42]. The confounding behaviors of active colloids originates from their nonequilibrium nature. Active matter constantly converts energy from internal or external sources to the mechanical self-propulsive motion. Therefore, active matter systems are inherently out of equilibrium and the framework of equilibrium thermodynamics may not be directly applied.

It is notable that many of above phenomena are universally observed in active suspensions regardless of the mechanisms of self-propulsion, which indicates that the self-propulsion itself is the most significant factor of the underlying physics. In the following section, we introduce the minimal model of self-propelling particles that can be helpful in illuminating the fundamental physics of active suspensions.

1.2 Active Brownian Particles

To describe active suspensions, we require a model for the microswimmers. The simplest possible description of microswimmers is offered by the active Brownian particle (ABP) model [43–45], which captures the essential features of the motion of microswimmers: self-propulsion and random reorientations. The model is surprisingly simple. ABPs self-propel, or swim, at intrinsic speed U_0 in direction $\boldsymbol{q}$ ($|\boldsymbol{q}| = 1$). In addition to the swimming motion, ABPs undergoes translational Brownian motion characterized by translational diffusivity D_T. Simultaneously, the swimming orientation $\boldsymbol{q}$ undergoes a random reorientation process, which is characterized by the rotational diffusivity D_R. The rotational diffusivity defines the times scale of reorientations $\tau_R = 1/D_R$.

In usual passive colloidal systems, the translational and rotational diffusions are both of thermal origin: the Brownian motion. Consequently, the translational and rotational diffusivities are coupled to each other via the thermal energy k_BT as described by the Stokes-Einstein-Sutherland relation: $\zeta D_T = \zeta_R D_R = k_BT$, where ζ and ζ_R are the Stokes translational and rotational drag coefficients. In this thesis we let the rotational diffusivity D_R be uncoupled from the thermal energy, and hence independent from the translational diffusivity, in order to allow considerations of reorientations from athermal sources such as autonomous rotations of motile

bacteria e.g. tumbling of *Escherichia coli* [46]. We note that the reorientation of ABPs is modeled as a continuous random process as we will discuss below, but microswimmers undergoing discrete random reorientations (e.g. the run-and-tumble motion of *Escherichia coli* [46]) are also well described by the ABP model at a long time scale $t \gg \tau_R$ [47, 48].

The transport properties of ABPs U_0, D_T, and D_R define two important length scales in the ABP model: the microscopic length $\delta = \sqrt{D_T \tau_R}$ and intrinsic run length $\ell_0 = U_0 \tau_R$ [49]. The behavior of an active suspension is governed the Péclet number $Pe = U_0 \ell_0 / D_T = (\ell_0/\delta)^2$, which acts as a measure of the activity of ABPs. In this introductory Chapter we provide a brief description of dilute suspensions of ABPs to demonstrate general features of the ABP model and neglect the effects of interparticle interactions among particles, i.e., *ideal* ABPs. We present a detailed treatment of interactions between active particles in Chapter 4.

While the size of a particle D is mostly immaterial in understanding the behavior of ideal ABPs, we note that it is still fundamentally important in some basic assumptions in the ABP model. We assume low Reynolds number $Re = \rho_f U_0 D / \mu \ll 1$ based on the colloidal size and speed of microswimmers, where ρ_f and μ are the density and viscosity of the suspending medium; the typical Reynolds number in aqueous active colloidal suspensions is on the order of $O(10^{-4})$ [50]. Also, the motion of ABPs is assumed to be overdamped by neglecting inertial effects. This assumption is valid when the Stokes number $St = \rho_p / \rho_f \cdot Re$ and the rotational Stokes number $St_R = St \cdot Pe_R$ are small, where ρ_P is the density of ABPs and $Pe_R = D/\ell_0$ is the reorientation Péclet number. For systems with a large Stokes number, the inertia of particles should be considered since their underdamped dynamics may result in different behaviors [51–58].

The overdamped stochastic motion of ABPs can be described in two manners. One can write the equations of motion for the particles including stochastic forces and torques for the Brownian motion and random reorientation. Such equations are called the (overdamped) Langevin equations (see appendix 2.7 for details) and are useful when performing Brownian Dynamics (BD) simulations of ABPs. An alternative and equivalent approach is to consider the probability density $P(\boldsymbol{x}, \boldsymbol{q}, t)$ of finding an ABP with position $\boldsymbol{x}$ and orientation $\boldsymbol{q}$ at time t. The evolution of the probability density in the phase space $(\boldsymbol{x}, \boldsymbol{q})$ is governed by the Smoluchowski

equation:

$$\frac{\partial P}{\partial t} + \nabla \cdot \boldsymbol{j}_T + \nabla_R \cdot \boldsymbol{j}_R = 0 \,, \tag{1.1}$$

$$\boldsymbol{j}_T = U_0 \boldsymbol{q} P - D_T \nabla P \,, \tag{1.2}$$

$$\boldsymbol{j}_R = -D_R \nabla_R P \,, \tag{1.3}$$

where $\boldsymbol{j}_T$ is the translational flux in the spatial domain, $\boldsymbol{j}_R$ is the rotational flux in the orientational domain, and $\nabla_R = \boldsymbol{q} \times \partial/\partial \boldsymbol{q}$ is the rotational gradient operator.

There is no general analytical solution methods known for the Smoluchowski equation (1.1)-(1.3) but the essential physics can be understood by considering the orientational moments of the probability density [59, 60].[1] The zeroth order moment is simply the concentration of the particles, or the number density $n = \int P d\boldsymbol{q}$. From eq. (1.1), the number density satisfies

$$\frac{\partial n}{\partial t} + \nabla \cdot \boldsymbol{j}_n = 0, \tag{1.4}$$

$$\boldsymbol{j}_n = U_0 \boldsymbol{m} - D_T \nabla n. \tag{1.5}$$

The first order moment, or the polar order $\boldsymbol{m} = \int P \boldsymbol{q} d\boldsymbol{q}$, represents the net orientation of the particles and it satisfies

$$\frac{\partial \boldsymbol{m}}{\partial t} + \nabla \cdot \boldsymbol{j}_m + (d-1) D_R \boldsymbol{m} = \boldsymbol{0}, \tag{1.6}$$

$$\boldsymbol{j}_m = U_0 \boldsymbol{Q} + \frac{1}{d} U_0 n \boldsymbol{I} - D_T \nabla \boldsymbol{m}. \tag{1.7}$$

Here, d is the spatial dimension for reorientation, $\boldsymbol{Q} = \int P(\boldsymbol{q}\boldsymbol{q} - \boldsymbol{I}/d) d\boldsymbol{q}$ is the traceless second order moment, or the nematic order tensor, and $\boldsymbol{I}$ is the second-order isotropic tensor. We note that the coupling between the orientational moments of neighboring orders (n & $\boldsymbol{m}$, $\boldsymbol{m}$ & $\boldsymbol{Q}$, etc.) arises from the active convective contribution $U_0 \boldsymbol{q} P$ in the translational flux (1.2) and brings about a hierarchical structure of orientational moments [59, 60], which requires a closure approximation for a closed set of equation. The appropriateness of a closure heavily depends on the character of individual problem [37, 60–62] and can be confirmed by numerical solutions of the full Smoluchowski equation (1.1)-(1.3) or BD simulations.

1.3 Mechanics of Active Suspensions

The expression for the number density flux (1.5) provides a starting point for a mechanical description of active suspensions. Multiplying the translational Stokes

[1] See appendix 4.7 for detailed derivations of the orientational moment equations.

drag coefficient ζ eq. (1.5) becomes

$$\mathbf{0} = -\zeta \boldsymbol{j}_n + \zeta U_0 \boldsymbol{m} + \nabla \cdot \boldsymbol{\sigma}^{osmo} , \tag{1.8}$$

where $\boldsymbol{\sigma}^{osmo} = -n\zeta D_T \boldsymbol{I} = -nk_BT\boldsymbol{I}$ is the osmotic stress of the particles. Equation (1.8) is a mechanical force balance on the ABPs. The first and second terms on the right-hand side represent the net hydrodynamic drag on the ABPs and average of the swim force $\boldsymbol{F}^{swim} = \zeta U_0 \boldsymbol{q}$ for the self-propulsive motion and the net force density is balanced by the divergence of the stress.

It is important to note that both the drag and swim forces originate from the suspending medium around an ABP. In the description of ABPs using Langevin and/or Smoluchowski equations, the existence of a medium is prone to be forgotten since it does not explicitly appear in the equations but only implicitly as the drag coefficients and Brownian diffusion. Yet the self-propulsion of microswimmers is fundamentally enabled by the presence of a medium. An individual active unit generates a propulsive force on its body by essentially 'pushing' a medium (whether it is a 'wet' fluid or a 'dry' surface) backwards and the resulted forward motion relative to the medium produces a drag force that is also exerted by the medium. From a mechanical perspective, the self-propulsion of microswimmers is not much different from us swimming in a pool — a body is propelled by pushing water with strokes and is simultaneously resisted also by the water. The only differences are that for microswimmers, the motion of a suspending fluid follows the Stokes equation due to the low Reynolds number environment and consequently the swim strokes require subtle mechanisms. The same logic applies to the reorientation torque for the rotational motion.

The particle force balance (1.8) shows that the average swim force $\zeta U_0 \boldsymbol{m}$ acts as an internal [50] or self-generated 'body' force [63]. Owing to the form of the polar order equation (1.6)-(1.7), the average swim force density can be written as a divergence at steady state: $\boldsymbol{m} = -\nabla \cdot (\boldsymbol{j}_m \tau_R/(d-1))$. This motivates us to treat the average swim force as an (divergence of) effective stress and the steady state force balance becomes

$$\mathbf{0} = -\zeta \boldsymbol{j}_n + \nabla \cdot \boldsymbol{\sigma}^{act}, \quad \boldsymbol{\sigma}^{act} = \boldsymbol{\sigma}^{swim} + \boldsymbol{\sigma}^{osmo} , \tag{1.9}$$

$$\boldsymbol{\sigma}^{swim} = -\frac{\zeta U_0 \ell}{d-1} \boldsymbol{j}_m = -\frac{\zeta U_0 \ell_0}{d-1} \boldsymbol{Q} - \Pi^{swim} \boldsymbol{I} + k_B T \ell_0 \nabla \boldsymbol{m} , \tag{1.10}$$

where $\boldsymbol{\sigma}^{act}$ is the active stress of the ABPs, $\boldsymbol{\sigma}^{swim}$ is the swim stress, and $\Pi^{swim} = \zeta U_0 \ell_0 n/(d(d-1))$ is the swim pressure [64]. In this mechanical formulation it is

clear that the swim pressure or stress is analogous to the equivalent (or dynamic) pressure in fluid mechanics [65] or the Maxwell stress in electrostatics [66].

The utility of the swim pressure can be clearly revealed by considering the concept of equivalent pressure. For a static incompressible fluid under an external potential ϕ^{ext} a mechanical force balance is given by: $\mathbf{0} = -\rho\nabla\phi^{ext} - \nabla p$, where ρ is the fluid density and p is the 'true' pressure of the fluid. One can combine the body force density $-\rho\nabla\phi^{ext}$ and the pressure gradient ∇p to rewrite the force balance as $\mathbf{0} = -\nabla\mathcal{P}$, where $\mathcal{P} = \rho\phi^{ext} + p$ is the equivalent pressure. When the external potential is unidirectional, say the familiar gravity field $\phi^g = gz$ (gravity acting in $-z$ direction, where g is the gravity acceleration constant), the force balance results in constant equivalent pressure throughout the whole fluid $\mathcal{P} = \rho gz + p =$ cosntant. Thus, the static condition of a fluid is described by the equivalent pressure in an intuitive fashion: there is no fluid motion if the equivalent pressure is constant. The real meaning of the constant equivalent pressure is, however, that there is a gradient in the 'true' pressure p; in order to resist motion induced by gravity and to maintain the static condition — the fluid pressure gradient develops toward the direction of the gravity. When computing the pressure exerted by the fluid on a wall, one needs to use the 'true' pressure of the fluid p not the equivalent pressure. Nevertheless, the equivalent pressure does not lose its utility because it allows us to think about the 'true' pressure only with the height of the static fluid.

Similarly the swim pressure provides a convenient way to compute the pressure exerted by ABPs on a simple no-flux boundary [60].[2] Suppose a suspension of ideal ABPs ($z > 0$) with the bulk concentration n^∞ is dammed by a flat no-flux wall at $z = 0$. Integrating eq. (1.9) from the wall ($z = 0$) to an arbitrary position ($z = L$), we obtain $[\sigma_{zz}^{swim} + \sigma_{zz}^{osmo}]_{z=0} = [\sigma^{swim} + \sigma_{zz}^{osmo}]_{z=L}$. At the wall, the no-flux condition $j_{m,zz} = 0$ results $\sigma_{zz}^{swim} = 0$. Also, in the limit of $L \to \infty$ the effect of the wall becomes negligible at $z = L$ and the suspension becomes homogeneous: $\nabla\boldsymbol{m} = \mathbf{0}$, $\boldsymbol{Q} = \mathbf{0}$, and $n = n^\infty$. Consequently, we obtain $\Pi^{osmo}|_{z=0} = [\Pi^{swim} + \Pi^{osmo}]_\infty$, where $\Pi^{osmo} = nk_BT$ is the 'true' osmotic pressure of the particles. Therefore, the pressure exerted by ABPs on the wall per unit area is simply given as the sum of the bulk swim and osmotic pressures far from the wall. Furthermore, this shows that

[2] We note that when special particle-wall interactions (e.g. a wall exerting a torque on active particles [67]) are present, the polar order flux $\boldsymbol{j}_m$ may not vanish at the wall due to the interactions. In such a case, the particle pressure on the wall should include the effect of swim stress: $\Pi_{z=0}^{osmo} = [\Pi^{swim} + \Pi^{osmo}]_\infty - \sigma_{zz}^{swim}|_{z=0}$. We also note that the polar order $\boldsymbol{m}$ cannot be written as written as $\nabla \cdot \boldsymbol{j}_m$ when there is a 'bulk' torque (e.g. fluid flow [37] or external field [68]).

there exists an accumulation of ABPs at the wall which increases with the activity $Pe = U_0\ell_0/D_T = (\ell_0/\delta)^2$: $n|_{z=0} = n^\infty(1 + Pe/(d(d-1))$.

1.4 Thesis Outline

In Chapter 2 of this thesis, we answer, arguably, one of the most fundamental questions for active suspensions: the effects of an abrupt spatial variation in transport properties U_0, D_T, and D_R. We present analytical solutions of the steady state number density and polar order for various simple geometries and confirm their accuracy by performing computer simulations. From the analytical solutions and computer simulations, we find that the difference in the number densities in regions with different transport properties is governed by the swim speed difference and modulated in amplitude by the activity. We also investigate the transient effects of abrupt spatial variations in transport properties. We reveal that when ABPs are released at a position where a step change in transport properties occurs, the particles preferably partition to the region with longer reorientation time $\tau_R = 1/D_R$ and the swim speed difference does not produce nor affect the transient partitioning. We explain the connection between the seemingly contradictory results from transient and steady states. Using the results from Chapter 2, we analyze the mechanics of active suspensions with an abrupt spatial variation in transport properties in Chapter 3. By considering a mechanical force balance for the whole suspension, including the ABPs and the suspending medium, we reveal a unique feature of active matter systems with spatially varying activities: the reverse osmotic effect. We show that the swim strokes of ABPs can be utilized as a microscopic pump to spontaneously generate a reverse osmotic fluid flow from regions of high concentration to low. We also show that the reverse osmotic effect results in a counter-intuitive reverse-diffusiophoretic motion of a passive body inside an active suspension.

In Chapter 4, we further demonstrate the utility of the mechanical perspective in understanding active matter systems by considering MIPS. We first revisit the classical and statistical thermodynamic descriptions of phase equilibrium and introduce an equivalent mechanical description of phase equilibrium. Unlike the thermodynamic framework, which only applies to equilibrium systems, a mechanical theory can be readily generalized to analyze the nonequilibrium phase coexistence. Using the mechanical approach, we discover phase coexistence conditions of MIPS that allow an equal-area construction of a phase diagram on the active pressure vs. collisional pressure plane. The phase diagram obtained by the mechanical theory excellently agrees with the computer simulations of MIPS. We also explore the microscopic

structure of phase interfaces in MIPS using the mechanical theory and report a unique nonequilibrium interfacial behavior in MIPS for the first time. We find that the width of phase interface nonmonotically varies with the activity of particles and provide a mechanical explanation of this phenomena.

References

[1] R. Brown, "Xxvii. a brief account of microscopical observations made in the months of june, july and august 1827, on the particles contained in the pollen of plants; and on the general existence of active molecules in organic and inorganic bodies," *The philosophical magazine*, vol. 4, no. 21, pp. 161–173, 1828.

[2] ——, "Xxiv. additional remarks on active molecules," *The Philosophical Magazine*, vol. 6, no. 33, pp. 161–166, 1829.

[3] A. Einstein *et al.*, "On the motion of small particles suspended in liquids at rest required by the molecular-kinetic theory of heat," *Annalen der physik*, vol. 17, no. 549-560, p. 208, 1905.

[4] R. F. Ismagilov, A. Schwartz, N. Bowden, and G. M. Whitesides, "Autonomous movement and self-assembly," *Angewandte Chemie International Edition*, vol. 41, no. 4, pp. 652–654, 2002.

[5] W. F. Paxton *et al.*, "Catalytic nanomotors: Autonomous movement of striped nanorods," *Journal of the American Chemical Society*, vol. 126, no. 41, pp. 13 424–13 431, 2004.

[6] R. Dreyfus, J. Baudry, M. L. Roper, M. Fermigier, H. A. Stone, and J. Bibette, "Microscopic artificial swimmers," *Nature*, vol. 437, no. 7060, pp. 862–865, 2005.

[7] J. R. Howse, R. A. Jones, A. J. Ryan, T. Gough, R. Vafabakhsh, and R. Golestanian, "Self-motile colloidal particles: From directed propulsion to random walk," *Physical review letters*, vol. 99, no. 4, p. 048 102, 2007.

[8] B. J. Williams, S. V. Anand, J. Rajagopalan, and M. T. A. Saif, "A self-propelled biohybrid swimmer at low reynolds number," *Nature communications*, vol. 5, no. 1, pp. 1–8, 2014.

[9] H.-R. Jiang, N. Yoshinaga, and M. Sano, "Active motion of a janus particle by self-thermophoresis in a defocused laser beam," *Physical review letters*, vol. 105, no. 26, p. 268 302, 2010.

[10] S. Sanchez, A. N. Ananth, V. M. Fomin, M. Viehrig, and O. G. Schmidt, "Superfast motion of catalytic microjet engines at physiological temperature," *Journal of the American Chemical Society*, vol. 133, no. 38, pp. 14 860–14 863, 2011.

[11] G. Volpe, I. Buttinoni, D. Vogt, H.-J. Kümmerer, and C. Bechinger, "Microswimmers in patterned environments," *Soft Matter*, vol. 7, no. 19, pp. 8810–8815, 2011.

[12] J. Li *et al.*, "Water-driven micromotors for rapid photocatalytic degradation of biological and chemical warfare agents," *ACS nano*, vol. 8, no. 11, pp. 11 118–11 125, 2014.

[13] X. Ma, K. Hahn, and S. Sanchez, "Catalytic mesoporous janus nanomotors for active cargo delivery," *Journal of the American Chemical Society*, vol. 137, no. 15, pp. 4976–4979, 2015.

[14] C. Bechinger, R. Di Leonardo, H. Löwen, C. Reichhardt, G. Volpe, and G. Volpe, "Active particles in complex and crowded environments," *Reviews of Modern Physics*, vol. 88, no. 4, p. 045 006, 2016.

[15] P. J. Russell, P. E. Hertz, B. McMillan, and J. Benington, *Biology: the dynamic science*. Cengage Learning, 2020.

[16] S. T. Mortimer, "A critical review of the physiological importance and analysis of sperm movement in mammals," *Human reproduction update*, vol. 3, no. 5, pp. 403–439, 1997.

[17] A. B. Kolomeisky, "Motor proteins and molecular motors: How to operate machines at the nanoscale," *Journal of Physics: Condensed Matter*, vol. 25, no. 46, p. 463 101, 2013.

[18] T. D. Ross, H. J. Lee, Z. Qu, R. A. Banks, R. Phillips, and M. Thomson, "Controlling organization and forces in active matter through optically defined boundaries," *Nature*, vol. 572, no. 7768, pp. 224–229, 2019.

[19] A. Doostmohammadi, J. Ignés-Mullol, J. M. Yeomans, and F. Sagués, "Active nematics," *Nature communications*, vol. 9, no. 1, pp. 1–13, 2018.

[20] A.-Y. Jee, Y.-K. Cho, S. Granick, and T. Tlusty, "Catalytic enzymes are active matter," *Proceedings of the National Academy of Sciences*, vol. 115, no. 46, E10812–E10821, 2018.

[21] Y. Espmark and K. Kinderås, "Behavioural lateralisation in reindeer," *Rangifer*, vol. 22, no. 1, pp. 51–59, 2002.

[22] K. Tan *et al.*, "Bee-hawking by the wasp, vespa velutina, on the honeybees apis cerana and a. mellifera," *Naturwissenschaften*, vol. 94, no. 6, pp. 469–472, 2007.

[23] C. Blum and D. Merkle, *Swarm intelligence: introduction and applications*. Springer Science & Business Media, 2008.

[24] A. Sokolov, M. M. Apodaca, B. A. Grzybowski, and I. S. Aranson, "Swimming bacteria power microscopic gears," *Proceedings of the National Academy of Sciences*, vol. 107, no. 3, pp. 969–974, 2010.

[25] S. Mallory, C. Valeriani, and A. Cacciuto, "Curvature-induced activation of a passive tracer in an active bath," *Physical Review E*, vol. 90, no. 3, p. 032 309, 2014.

[26] R. Di Leonardo *et al.*, "Bacterial ratchet motors," *Proceedings of the National Academy of Sciences*, vol. 107, no. 21, pp. 9541–9545, 2010.

[27] A. Kaiser, A. Sokolov, I. S. Aranson, and H. Löwen, "Motion of two microwedges in a turbulent bacterial bath," *The European Physical Journal Special Topics*, vol. 224, no. 7, pp. 1275–1286, 2015.

[28] L. Angelani, R. Di Leonardo, and G. Ruocco, "Self-starting micromotors in a bacterial bath," *Physical review letters*, vol. 102, no. 4, p. 048 104, 2009.

[29] P. Galajda, J. Keymer, P. Chaikin, and R. Austin, "A wall of funnels concentrates swimming bacteria," *Journal of bacteriology*, vol. 189, no. 23, pp. 8704–8707, 2007.

[30] R. Di Giacomo *et al.*, "Deployable micro-traps to sequester motile bacteria," *Scientific reports*, vol. 7, no. 1, pp. 1–8, 2017.

[31] J. Stenhammar, R. Wittkowski, D. Marenduzzo, and M. E. Cates, "Light-induced self-assembly of active rectification devices," *Science advances*, vol. 2, no. 4, e1501850, 2016.

[32] M. Wan, C. O. Reichhardt, Z. Nussinov, and C. Reichhardt, "Rectification of swimming bacteria and self-driven particle systems by arrays of asymmetric barriers," *Physical review letters*, vol. 101, no. 1, p. 018 102, 2008.

[33] J. Tailleur and M. Cates, "Statistical mechanics of interacting run-and-tumble bacteria," *Physical review letters*, vol. 100, no. 21, p. 218 103, 2008.

[34] M. E. Cates and J. Tailleur, "Motility-induced phase separation," *Annu. Rev. Condens. Matter Phys.*, vol. 6, no. 1, pp. 219–244, 2015.

[35] Y. Fily and M. C. Marchetti, "Athermal phase separation of self-propelled particles with no alignment," *Physical review letters*, vol. 108, no. 23, p. 235 702, 2012.

[36] J. Palacci, S. Sacanna, A. P. Steinberg, D. J. Pine, and P. M. Chaikin, "Living crystals of light-activated colloidal surfers," *Science*, vol. 339, no. 6122, pp. 936–940, 2013.

[37] Z. Peng and J. F. Brady, "Upstream swimming and taylor dispersion of active brownian particles," *Physical Review Fluids*, vol. 5, no. 7, p. 073 102, 2020.

[38] J. Hill, O. Kalkanci, J. L. McMurry, and H. Koser, "Hydrodynamic surface interactions enable escherichia coli to seek efficient routes to swim upstream," *Physical review letters*, vol. 98, no. 6, p. 068 101, 2007.

[39] T. Kaya and H. Koser, "Direct upstream motility in escherichia coli," *Biophysical journal*, vol. 102, no. 7, pp. 1514–1523, 2012.

[40] E. Lushi, R. E. Goldstein, and M. J. Shelley, "Collective chemotactic dynamics in the presence of self-generated fluid flows," *Physical Review E*, vol. 86, no. 4, p. 040 902, 2012.

[41] S. Guo, D. Samanta, Y. Peng, X. Xu, and X. Cheng, "Symmetric shear banding and swarming vortices in bacterial superfluids," *Proceedings of the National Academy of Sciences*, vol. 115, no. 28, pp. 7212–7217, 2018.

[42] T. L. Hill, *Statistical mechanics: principles and selected applications*. Courier Corporation, 2013.

[43] F. Schweitzer, W. Ebeling, and B. Tilch, "Complex motion of brownian particles with energy depots," *Physical Review Letters*, vol. 80, no. 23, p. 5044, 1998.

[44] W. Ebeling, F. Schweitzer, and B. Tilch, "Active brownian particles with energy depots modeling animal mobility," *BioSystems*, vol. 49, no. 1, pp. 17–29, 1999.

[45] P. Romanczuk, M. Bär, W. Ebeling, B. Lindner, and L. Schimansky-Geier, "Active brownian particles-from individual to collective stochastic dynamics p," *The European Physical Journal Special Topics*, vol. 202, 2012.

[46] H. C. Berg and D. A. Brown, "Chemotaxis in escherichia coli analysed by three-dimensional tracking," *Nature*, vol. 239, no. 5374, pp. 500–504, 1972.

[47] M. E. Cates and J. Tailleur, "When are active brownian particles and run-and-tumble particles equivalent? consequences for motility-induced phase separation," *EPL (Europhysics Letters)*, vol. 101, no. 2, p. 20 010, 2013.

[48] A. P. Solon, M. E. Cates, and J. Tailleur, "Active brownian particles and run-and-tumble particles: A comparative study," *The European Physical Journal Special Topics*, vol. 224, no. 7, pp. 1231–1262, 2015.

[49] W. Yan and J. F. Brady, "The force on a boundary in active matter," *J. Fluid Mech.*, vol. 785, R1.1–R1.11, Dec. 2015.

[50] S. C. Takatori and J. F. Brady, "Forces, stresses and the (thermo?) dynamics of active matter," *Curr. Opin. Colloid Interface Sci.*, vol. 21, pp. 24–33, Feb. 2016.

[51] ——, "Inertial effects on the stress generation of active fluids," *Physical Review Fluids*, vol. 2, no. 9, p. 094 305, 2017.

[52] M. Sandoval, "Pressure and diffusion of active matter with inertia," *Physical Review E*, vol. 101, no. 1, p. 012 606, 2020.

[53] A. K. Omar, K. Klymko, T. GrandPre, P. L. Geissler, and J. F. Brady, "Tuning nonequilibrium phase transitions with inertia," *arXiv preprint arXiv:2108.10278*, 2021.

[54] G. P. Nguyen, R. Wittmann, and H. Löwen, "Active ornstein–uhlenbeck model for self-propelled particles with inertia," *Journal of Physics: Condensed Matter*, vol. 34, no. 3, p. 035 101, 2021.

[55] J. Su, H. Jiang, and Z. Hou, "Inertia-induced nucleation-like motility-induced phase separation," *New Journal of Physics*, vol. 23, no. 1, p. 013 005, 2021.

[56] H. Löwen, "Inertial effects of self-propelled particles: From active brownian to active langevin motion," *The Journal of chemical physics*, vol. 152, no. 4, p. 040 901, 2020.

[57] L. Caprini and U. Marini Bettolo Marconi, "Inertial self-propelled particles," *The Journal of Chemical Physics*, vol. 154, no. 2, p. 024 902, 2021.

[58] M. Sandoval, "Pressure and diffusion of active matter with inertia," *Physical Review E*, vol. 101, no. 1, p. 012 606, 2020.

[59] D. Saintillan and M. J. Shelley, "Theory of active suspensions," in *Complex Fluids in biological systems*, Springer, 2015, pp. 319–355.

[60] W. Yan and J. F. Brady, "The force on a boundary in active matter," *Journal of Fluid Mechanics*, vol. 785, 2015.

[61] H. Row and J. F. Brady, "Reverse osmotic effect in active matter," *Physical Review E*, vol. 101, no. 6, p. 062 604, 2020.

[62] A. Dulaney and J. Brady, "Waves in active matter: The transition from ballistic to diffusive behavior," *Physical Review E*, vol. 101, no. 5, p. 052 609, 2020.

[63] W. Yan and J. F. Brady, "The swim force as a body force," *Soft Matter*, vol. 11, no. 31, pp. 6235–6244, Jul. 2015.

[64] S. C. Takatori, W. Yan, and J. F. Brady, "Swim pressure: Stress generation in active matter," *Phys. Rev. Lett.*, vol. 113, no. 2, p. 028 103, 2014.

[65] S. Paliwal, J. Rodenburg, R. van Roij, and M. Dijkstra, "Chemical potential in active systems: Predicting phase equilibrium from bulk equations of state?" *New Journal of Physics*, vol. 20, no. 1, p. 015 003, 2018.

[66] H. H. Woodson and J. Melcher, *Electromechanical dynamics.(part2)*, 1968.

[67] A. P. Solon *et al.*, "Pressure is not a state function for generic active fluids," *Nature Physics*, vol. 11, no. 8, pp. 673–678, 2015.

[68] S. C. Takatori and J. F. Brady, "Swim stress, motion, and deformation of active matter: Effect of an external field," *Soft Matter*, vol. 10, no. 47, pp. 9433–9445, 2014.

Chapter 2

ACTIVE MATTER WITH SPATIALLY VARYING TRANSPORT PROPERTIES

This chapter includes content from our previously published article:

[1] H. Row and J. F. Brady, "Reverse osmotic effect in active matter," *Physical Review E*, vol. 101, no. 6, p. 062 604, 2020. DOI: 10.1103/PhysRevE.101.062604,

2.1 Introduction

Intriguing non-equilibrium behaviors exhibited by colloidal active matter systems can be tuned using external means such as light [1–3]. Spatial control of activity can direct transport [4, 5], which offers a number of intriguing applications, e.g. reproduction of images by projecting light patterns [6, 7] and rectification of microswimmers [8, 9].

The concentration variation resulting from a spatial variation in activity was first explored by Schnitzer [10] and later by Tailleur & Cates [11–13] who showed that for slow spatial variations in one dimension the number density n of active particles is inversely proportional to the speed of self-propulsion or swimming U, i.e. nU = constant in the absence of translational diffusion.

In this chapter, we generalize this finding and present results for an abrupt change of activity in any dimension and also include the effects of thermal Brownian motion, allowing us to span the complete range from thermal to active transport. We consider spatial variations in all three transport properties, U_0, D_T, and D_R. Several simple geometries that permit analytical solutions are compared with the results to Brownian dynamics (BD) simulations. We also present an interesting transient behavior of the Green's function of the Smoluchowski equation for active particles with an abrupt change in activity.

We limit our analysis to dilute isothermal suspensions of spherical ABPs in order to illustrate the basic physics. Since isothermal suspensions are considered, a variation in D_T is equivalent to a spatially varying the Stokes drag coefficient ζ which depends on the viscosity of the suspending fluid and the the hydrodynamics

of the low Reynolds number motion of the ABPs. When the temperature varies within a system, well-known thermal drifts [14] should be considered.

2.2 Infinite Active Suspensions

We revisit the simple relationship nU = constant [10–13] and examine the conditions that allow it to hold. We consider purely active particles without the translational Brownian motion. In the absence of the translational diffusion, $D_T = 0$, and the number density balance (1.4) for no flux is $\nabla\cdot(U\boldsymbol{m}) = 0$, which, for a one dimensional geometry, requires $\boldsymbol{m} = \boldsymbol{0}$. From the polar order balance (1.6) at steady state the polar order is

$$\boldsymbol{m} \approx -\frac{1}{d(d-1)D_R}\nabla\,(nU)\ , \tag{2.1}$$

which implies that $nU \approx$ constant. For (2.1) to hold in general the nematic order $\boldsymbol{Q}$ needs to be small ($\ll n\boldsymbol{I}$) even when there is an abrupt change in properties. For this reason, the condition (2.1) is exact for 1D reorientations and therefore nU = const. [10, 11] since the traceless nematic order $Q \equiv 0$ for motion that is strictly 1D.[1] In the following, we show with examples that the nematic order $\boldsymbol{Q}$ is sufficiently small in higher dimensions as well by comparison to solution of the full Smoluchowski equation. Thus, we close the hierarchy with $\boldsymbol{Q}=\boldsymbol{0}$ [15].

To explore the validity of nU = const., when thermal Brownian motion is present and there is a sharp discontinuity in activity, we first consider an infinite suspension of ABPs with a step change in transport properties at $x = 0$ as described in Fig. 2.1. Since the two regions have different transport properties, the Smoluchowski equation (1.1) is written for each region:

$$\frac{\partial P_i}{\partial t} \ + \ \nabla\cdot\boldsymbol{j}_{T,i} \ + \ \nabla_q\cdot\boldsymbol{j}_{q,i} = 0\ , \tag{2.2}$$

$$\boldsymbol{j}_{T,i} = U_i\boldsymbol{q}P_i \ - \ D_{T,i}\nabla P_i\ , \tag{2.3}$$

$$\boldsymbol{j}_{q,i} = -D_{R,i}\nabla_q P_i\ . \tag{2.4}$$

Here, the subscript i (= 1 or 2) is the index of a region and the probability density functions P_1 and P_2 are defined for $x < 0$ and $x \geq 0$ in the spatial domain. Consequently, equations for the first two orientational moments of the probability density are also obtained for each region as

$$\frac{\partial n_i}{\partial t} \ + \ \nabla\cdot\boldsymbol{j}_{n,i} = 0\ , \tag{2.5}$$

[1] For 1D processes one cannot set $d = 1$ in eq. (1.6) as the reorientation process is just changing direction ± rather than an angular displacement as modeled in the Smoluchowski equation. The conclusion is the same, however, and the equivalent of $\boldsymbol{Q} = \boldsymbol{0}$ also holds.

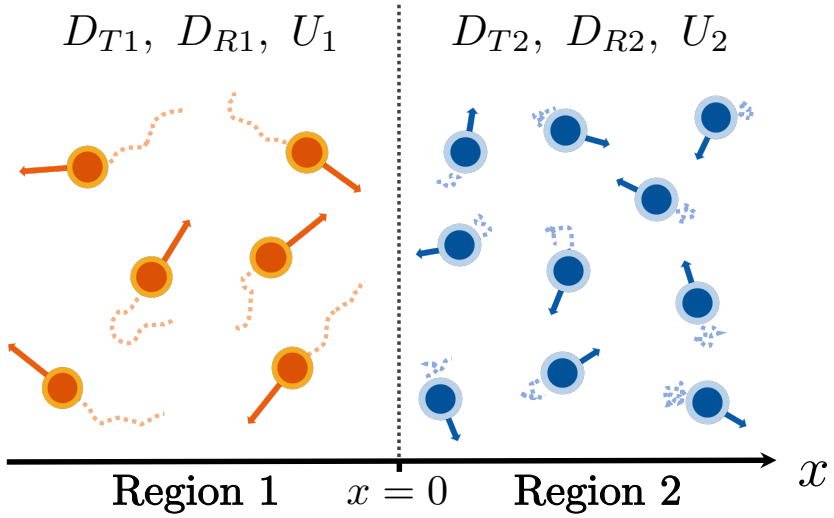

Figure 2.1: A schematic of an infinite suspension of ABPs with an abrupt change in activity. In regions 1 ($x < 0$) and 2 ($x \geq 0$) the ABPs have swim speeds U_i, translational diffusivities D_{Ti}, and rotational diffusivities D_{Ri}, where the subscript i (= 1 or 2) represents the index of a region.

$$\boldsymbol{j}_{n,i} = U_i \boldsymbol{m}_i \ - \ D_{T,i} \nabla n_i \ , \tag{2.6}$$

$$\frac{\partial \boldsymbol{m}_i}{\partial t} \ + \ \nabla \cdot \boldsymbol{j}_{m,i} \ + \ (d-1) D_{R,i} \boldsymbol{m}_i = \boldsymbol{0} \ , \tag{2.7}$$

$$\boldsymbol{j}_{m,i} = U_i \boldsymbol{Q}_i \ + \ \frac{1}{d} U_i n_i \boldsymbol{I} \ - \ D_{T,i} \nabla \boldsymbol{m}_i \ . \tag{2.8}$$

The boundary conditions are a homogeneous random suspension far from the step change: $n_1 \to n^{-\infty}$ and $m_{1,x} \to 0$ as $x \to -\infty$, and $n_2 \to n^{+\infty}$ and $m_{2,x} \to 0$ as $x \to \infty$. At the discontinuity in properties, the full Smoluchowski equation requires that the field variables, n and $\boldsymbol{m}$, etc., be continuous. Even though nU = const. would predict a discontinuity in n at $x = 0$, the problem is singular and thermal Brownian motion, no matter how small (no matter how large Pe), will result in a boundary layer of thickness $O(\ell Pe^{-1} = D_T/U)$ where Brownian motion balances advection and the probability density is continuous. Thus, n, m_x, and the fluxes $j_{n,x}$ and $j_{m,xx}$ are continuous at $x = 0$. We define $\langle n \rangle$ as the scale for the number density: $\int_{-L}^{L} n \, dx \to 2L\langle n \rangle$ as $L \to \infty$. The moment equations are easily solved at steady state with the closure $\boldsymbol{Q}_i = \boldsymbol{0}$:

$$m_{i,x} = m_{x0} e^{\pm \lambda_i x} \ , \tag{2.9}$$

$$\frac{n_i}{n^{\mp\infty}} = 1 + \frac{C_i(U_1 - U_2)}{\pm\left(\dfrac{U_1}{C_1} + \dfrac{U_2}{C_2}\right) - C_i(U_1 - U_2)} e^{\pm\lambda_i x}\,, \tag{2.10}$$

where

$$\frac{m_{x0}}{\langle n\rangle} = \frac{\dfrac{1}{\sqrt{d}}(U_1 - U_2)}{\left(\dfrac{U_1}{C_1} + \dfrac{U_2}{C_2}\right) - \dfrac{1}{2}(U_1 - U_2)(C_1 - C_2)}\,, \tag{2.11}$$

$$\frac{n^{\mp\infty}}{\langle n\rangle} = \frac{\left(\dfrac{U_1}{C_1} + \dfrac{U_2}{C_2}\right) \mp C_i(U_1 - U_2)}{\left(\dfrac{U_1}{C_1} + \dfrac{U_2}{C_2}\right) - \dfrac{1}{2}(U_1 - U_2)(C_1 - C_2)}\,, \tag{2.12}$$

$$\lambda_i = \frac{\sqrt{d-1}}{\delta_i}\sqrt{1 + \frac{Pe_i}{d(d-1)}}\,, \tag{2.13}$$

$$C_i = \frac{1}{\sqrt{1 + \dfrac{d(d-1)}{Pe_i}}}\,. \tag{2.14}$$

Here, the subscript i indicates the two regions (1 or 2), $\delta_i = \sqrt{D_{Ti}/D_{Ri}}$ is the microscopic length scale related to the translational diffusion, $Pe_i = U_i\ell_i/D_{Ti} = U_i^2/(D_{Ti}D_{Ri}) = (\ell_i/\delta_i)^2$ is the Péclet number which is a measure of the activity of the ABPs, $n^{\mp\infty}$ is the number density far from the step change in transport properties ($x \to \mp\infty$), d is the spatial dimension for reorientation, upper signs are for region 1 ($x < 0$), and lower signs are for region 2 ($x \geq 0$). Note that the inverse screening length λ_i is the characteristic length scale of the decay of step changes in the field variables. A modified Péclet number C_i ranges from 0 when $Pe_i = 0$ to 1 when $Pe_i \to \infty$. The overall number density is simply $\langle n\rangle = (n^{-\infty} + n^{+\infty})/2$ for an infinite suspension.

The analytic solution gives the distribution of number densities as

$$\frac{n^{+\infty}}{n^{-\infty}} = \frac{C_2U_1 + C_1U_2 + C_1C_2^2(U_1 - U_2)}{C_2U_1 + C_1U_2 - C_1^2C_2(U_1 - U_2)}\,, \tag{2.15}$$

and its typical functional form is presented in Fig. 2.2. The analytical solution (2.10) indicates that the number density difference is governed by the swim speed difference

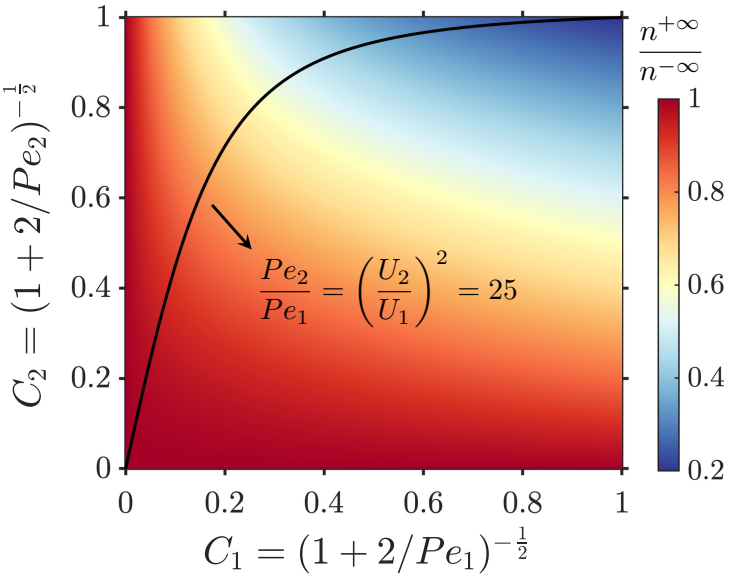

Figure 2.2: Color map of $n^{+\infty}/n^{-\infty}$ for $U_2/U_1 = 5$. The modified Péclet numbers $C_i = 0$ when $Pe_i = 0$ and $C_i \to 1$ when $Pe_i \to \infty$. The black line represents the case when diffusivities are the same in the two regions. When activities in both regions are high ($C_1,\ C_2 \approx 1$), $n^{+\infty}/n^{-\infty} \approx U_1/U_2 = 0.2$ i.e. nU = constant. If either of the two regions is diffusion-dominated ($C_i \approx 0$), the number density becomes constant throughout the whole suspension: $n^{+\infty} = n^{-\infty}$.

and modulated in amplitude by Pe. The number density is predicted to be always lower in the region with higher swim speed and the nonzero polar order points *towards* the region with slower swim speed. If there is no difference in swim speeds ($U_1 - U_2 = 0$), the suspension becomes homogeneous; the number density is uniform and the polar order is zero everywhere. Also, it is notable that eqn. (2.15) recovers the simple relation nU = const. from the previous section when activities in the two regions are large, i.e. $C_i \to 1$, or equivalently $Pe_i \to \infty$, for $i = 1$ and 2. As the activity Pe decreases the difference of the number densities in the two regions fades away.

In order to verify the analytical solution, BD simulations have been performed as described in Appendix 2.7 and the results are compared with the analytical solution in Fig. 2.3. When activity dominates translational diffusion ($Pe \gg 1$), the number density jumps sharply at the boundary of the two regions $x = 0$ and nU becomes constant. In the absence of translational Brownian motion, indicated by the black crosses in Fig. 2.3, nU is constant everywhere. Increasing the diffusivities decreases Pe and smears out the sharpness of the density jump.

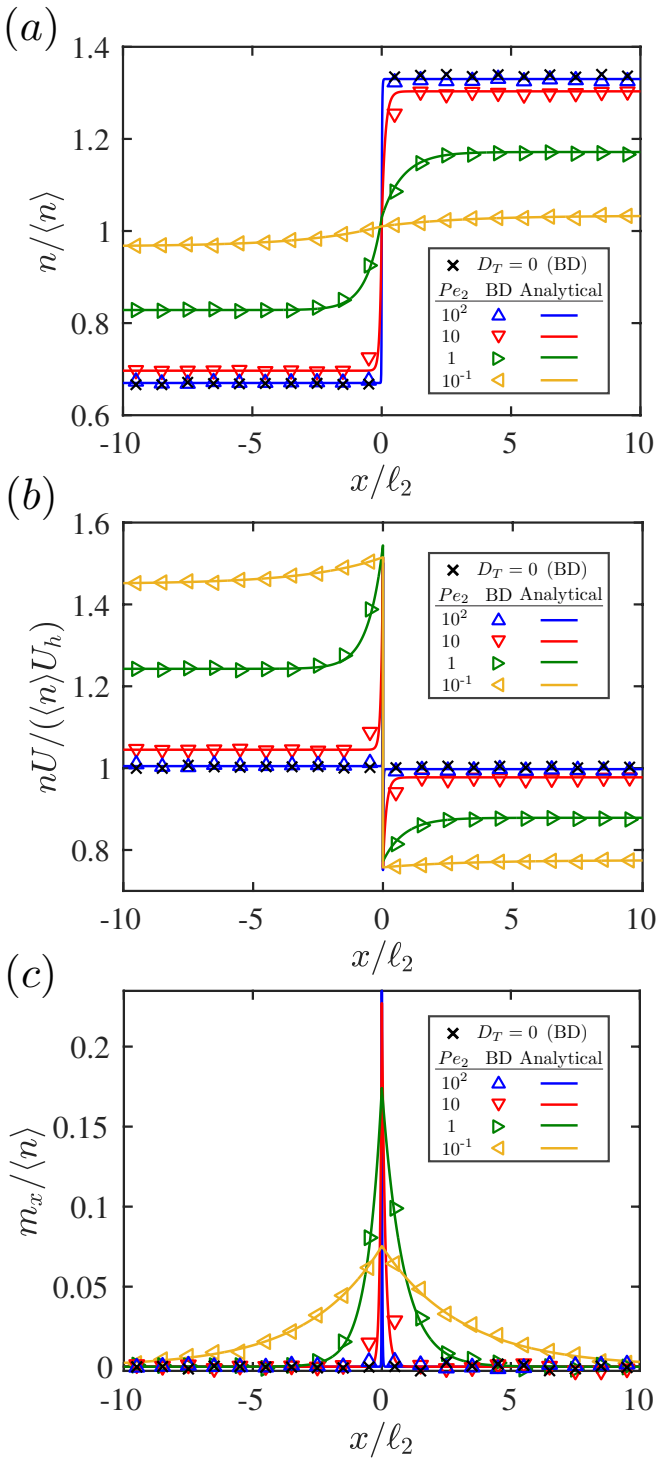

Figure 2.3: (a) Number densities scaled with the overall number density $\langle n\rangle$, (b) the product of the number density and swim speed scaled with the overall number density and the harmonic mean of the swim speeds ($U_h = 2(U_1^{-1} + U_2^{-1})^{-1}$), and (c) polar orders scaled with the overall number density versus the position x scaled with the run length in the region 2 $\ell_2 = U_2/D_{R2}$ when the swim speed abruptly changes at $x = 0$: $U_1/U_2 = 2$, $D_{T1} = D_{T2}$, and $D_{R1} = D_{R2}$. The translational diffusivity D_T is systematically changed to show the effect of the Brownian motion. Markers are BD simulations and solid lines are the analytic solutions of eqs. (2.5)-(2.8) with $\boldsymbol{Q} = \mathbf{0}$ ((2.9)-(2.14)).

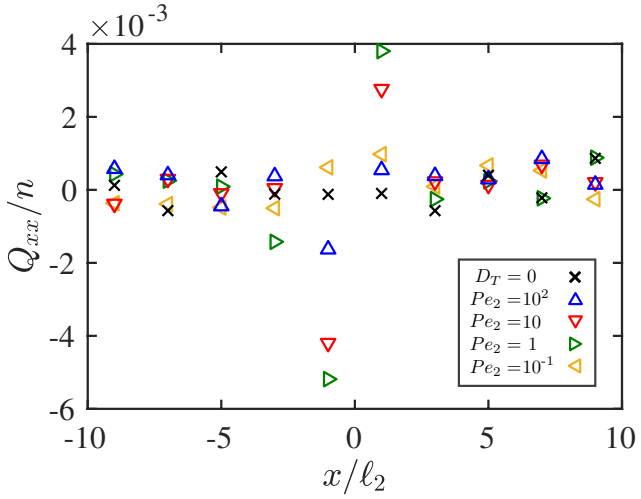

Figure 2.4: Relative magnitude of the nematic order Q_{xx} compared to the number density n as a function of the position x scaled with the run length in the region $2\,\ell_2 = U_2/D_{R2}$ obtained by BD simulations. The swim speed abruptly changes at $x = 0$ so that $U_1/U_2 = 2$, $D_{T1} = D_{T2}$, and $D_{R1} = D_{R2}$. The translational diffusivity D_T is systematically changed to show the effect of the Brownian motion. When $Pe < 100$ the nematic order is three orders of magnitude smaller than the number density allowing the simple closure $\boldsymbol{Q} = \boldsymbol{0}$ to result in the highly accurate analytical solution.

Excellent agreements of the analytical solution and BD simulations in Fig. 2.3 demonstrate the propriety of the assumption $\boldsymbol{Q} = \boldsymbol{0}$ as a closure of the orientational-moment hierarchy when active matter systems have abrupt spatial variations in transport properties. For the validity of the simple closure, $\boldsymbol{Q} \ll n\boldsymbol{I}$ is required and we confirm it by comparing the number density and nematic order from BD simulations as shown in Fig. 2.4. We find that the nematic order is three orders of magnitude smaller than the number density and consequently assuming $\boldsymbol{Q} = \boldsymbol{0}$ does not compromise the accuracy significantly when $Pe < 100$. For extremely high activities, the effect of nematic field is prominent and higher order moments should be taken into account.

We note that our results are in contrast to the study in [4] where they found via simulations that a spatial variation in number density occurred when D_T varied even *without* activity. In addition to the BD simulations, we also confirmed our findings with numerical solutions of the full Smoluchowski equation obtained by the finite element method [16] in order to verify the predictions of the analytical solution (2.9)-(2.14) obtained by the $\boldsymbol{Q} = \boldsymbol{0}$-closure.

Figure 2.5 shows that solutions of the full Smoluchowski equation agree with the

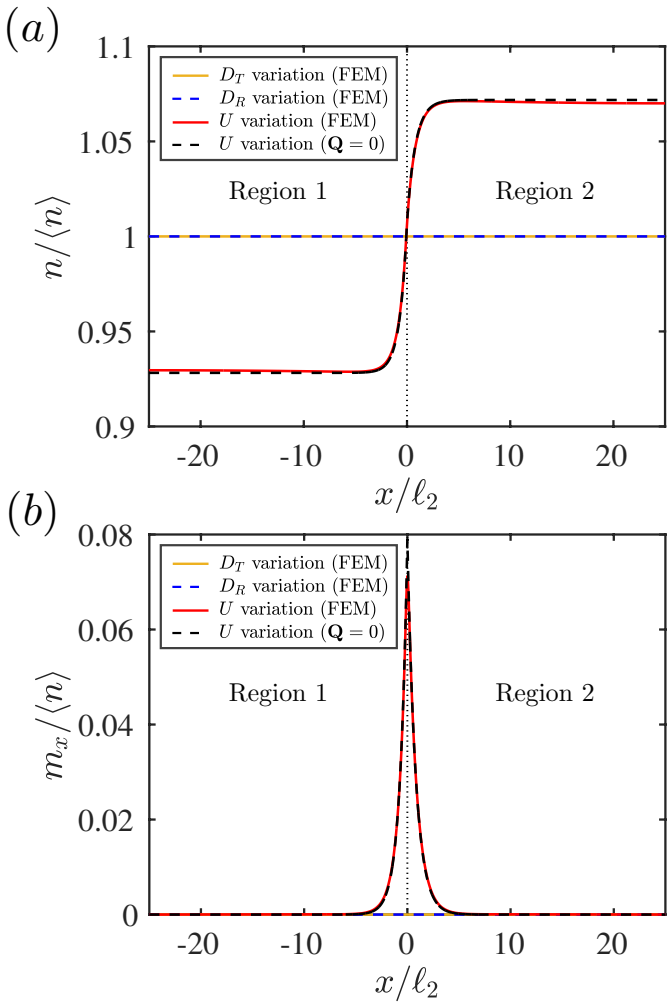

Figure 2.5: (a) Number densities and (b) polar orders scaled with $\langle n\rangle$. Black dashed line represents the analytical solution obtained by the $\boldsymbol{Q}=\mathbf{0}$-closure ((2.9)-(2.14)) and the other lines are obtained by solving the full Smoluchowski equation with the finite element method. The position x is scaled with the run length ℓ_2 in region 2. In region 1 ($x<0$), $Pe=2$ and in region 2 ($x\geq 0$), $Pe=1$. The number density changes only when there exists variation of swim speed.

$\boldsymbol{Q}=\mathbf{0}$-closure and that the variation in the number density and the peak of the polar order only occurs when the swim speed is different in the two regions. The number density changes rapidly only near $x=0$. Since $\boldsymbol{m}\sim\nabla n$, the polar order field is nearly zero everywhere except near $x=0$ where it has a peak as seen in Fig. 2.5(b). The sharpness of the peak increases as the screening length λ^{-1} decreases. In the singular athermal limit ($D_T\to 0$), the number density satisfies $nU=$ const. and the polar order becomes a δ-function if swim speeds are different in the two regions.

If suspended particles are not active in one region, say region 2 (i.e. $U_2=0$), the

analytical solution to the moment equations (2.5)-(2.8) at steady state is obtained as

$$\frac{n_1}{n^{-\infty}} = 1 + \frac{C_1 Pe_{1,2}^{\frac{1}{2}} e^{\lambda_1 x}}{\left(\frac{1}{C_1} - C_1\right) Pe_{1,2}^{\frac{1}{2}} + 1}, \tag{2.16}$$

$$n_2 = n^{+\infty}, \tag{2.17}$$

$$m_{1,x} = m_{x0} e^{\lambda_1 x}, \tag{2.18}$$

$$m_{2,x} = m_{x0} e^{\frac{x}{\delta_2}}, \tag{2.19}$$

where

$$\frac{m_{x0}}{\langle n \rangle} = \frac{\frac{1}{\sqrt{d}} Pe_{1,2}^{\frac{1}{2}}}{\left(\frac{1}{C_1} - \frac{C_1}{2}\right) Pe_{1,2}^{\frac{1}{2}} + 1}, \tag{2.20}$$

$$\frac{n^{-\infty}}{\langle n \rangle} = \frac{\left(\frac{1}{C_1} - C_1\right) Pe_{1,2}^{\frac{1}{2}} + 1}{\left(\frac{1}{C_1} - \frac{C_1}{2}\right) Pe_{1,2}^{\frac{1}{2}} + 1}, \tag{2.21}$$

$$\frac{n^{+\infty}}{\langle n \rangle} = \frac{\frac{1}{C_1} Pe_{1,2}^{\frac{1}{2}} + 1}{\left(\frac{1}{C_1} - \frac{C_1}{2}\right) Pe_{1,2}^{\frac{1}{2}} + 1}, \tag{2.22}$$

$$Pe_{1,2} = \frac{U_1^2}{d(d-1) D_{T2} D_{R2}}. \tag{2.23}$$

Here, $Pe_{1,2}$ is the global Péclet number that represents the relative significance of advective transport in region 1 compared to diffusive transport in region 2. By comparing the analytical solutions eqs. (2.9)-(2.14) and eqs. (2.16)-(2.23), we find an interesting difference between weakly active ABPs ($U_0 > 0$ and $Pe \approx 0$) and passive Brownian particles (PBPs; $U_0 = 0$ and so $Pe = 0$), which are generally perceived to be indistinguishable to each other [17, 18] since they both just diffuse with the thermal diffusivity D_T exhibiting the identical diffusion-dominated dynamics. The analytical solutions predict different steady state behaviors for passive-like ABPs and PBPs when there are spatial variations in activity. As seen in Fig. 2.2 when

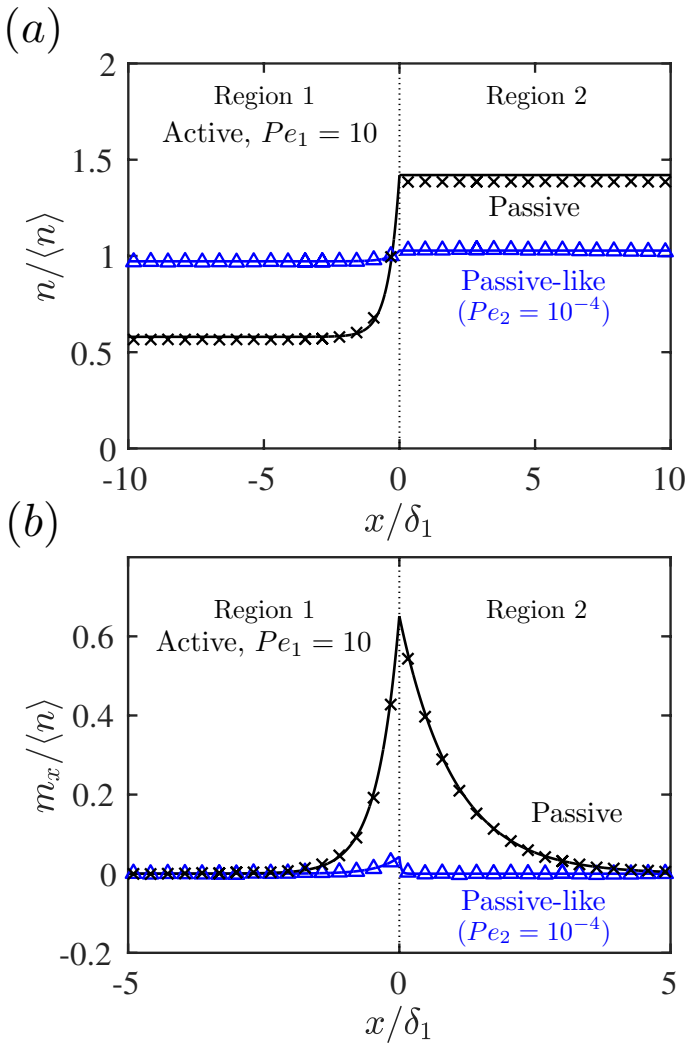

Figure 2.6: (a) Number densities and (b) polar orders scaled with the overall number density $\langle n \rangle$ versus the position x scaled with the microscopic length in region 1 $\delta_1 = \sqrt{D_{T1}/D_{R1}}$ in 2D. Particles are active ($Pe_1 = 10$) in region 1 and the transnational diffusivity is the same in the two regions. When both regions are active (blue), the number density is nearly constant even though swim speeds in the two regions differ ($U_1/U_2 = 10$) due to the passive-like ($Pe_2 = 10^{-4}$) character in region 2. When particles are not active in region 2 (black) the number density abruptly jumps at the boundary. The global Péclet number $Pe_{1,2} = U_1^2/(2D_{T2}D_{R2}) = 5$ in the passive region. Markers are BD simulations and solid lines are the analytic solutions ((2.16)-(2.23)).

particles are active throughout the whole suspension the number density becomes nearly constant everywhere provided either of the two regions is diffusion-dominated ($Pe \ll 1$). However when particles are not active in one region, the analytical solution (2.16)-(2.23) predicts that the number density can have a significant jump

at the boundary of the two regions even though $Pe = 0$ in the passive region.

We have performed BD simulations to verify this prediction and observe distinctive behaviors of the two types as seen in Fig. 2.6. The analytical solutions obtained by the $\boldsymbol{Q} = \mathbf{0}$-closure shows great accuracy. While weakly active ABPs and PBPs are usually indistinguishable by themselves, when each of them is compared with particles with a reference activity (in region 1), whether the activity Pe is nearly or exactly zero makes a singular difference. For suspensions of ABPs, the maximum jump in the number density is set by the ratio of swim speeds following $nU = \text{const.}$ and finite Pe moderates it. If the swim speed in one region is exactly zero, however, the conditions become singular; an infinitely large maximum jump in the number density and $Pe = 0$ to alleviate the singularity compete. Consequently, the number density is not simply constant even though $Pe = 0$ in the passive region. The different behaviors of ABPs and PBPs in the presence of a reference region with a different activity can be utilized as a test for the presence of extremely small activity in colloidal suspensions.

2.3 Active Suspensions Confined by Planar Walls

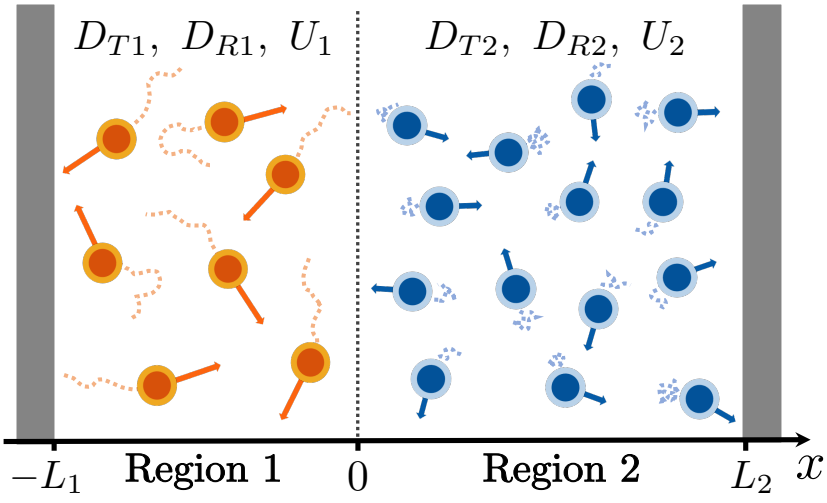

Figure 2.7: A schematic of a suspension of ABPs with an abrupt change in activity bounded between two parallel planar walls. In regions 1 ($-L_1 \le x < 0$) and 2 ($0 \le x \le L_2$) the ABPs have swim speeds U_i, translational diffusivities D_{Ti}, and rotational diffusivities D_{Ri}, where the subscript i (= 1 or 2) represents the index of a region.

Now finite suspensions of ABPs in the presence of an abrupt variation in activity are considered with two examples. We first explore a suspension confined between two

parallel walls at $x = -L_1$ and $x = L_2$ with a step change in transport properties at $x = 0$ as described in Fig. 2.7. The governing Smoluchowski equations (2.2)-(2.4) and associated moment equations (2.5)-(2.8) remain the same but the spatial domain for the two regions are now finite in x direction.

The walls are assumed to be hard and act as no-flux boundaries, i.e. $\boldsymbol{n} \cdot \boldsymbol{j}_T = 0$, at $x = -L_1$ and $x = L_2$, where $\boldsymbol{n}$ is the unit normal vector to the surface of walls. Continuity of field variables and fluxes at the boundary of the two regions ($x = 0$) still applies and the overall number density is $(L_1 + L_2)\langle n \rangle = \int_{-L_1}^{L_2} n \, dx$. The steady state analytical solution for bounded suspensions with the $\boldsymbol{Q} = \boldsymbol{0}$-closure is straightforward to obtain:

$$\frac{n_i}{n_0} = \gamma_i a_i(\cosh(\lambda_i x) - 1) \; + \; \gamma_i \frac{m_{x0}}{n_0} \sinh(\lambda_i x) \; + \; 1 \, , \tag{2.24}$$

$$\frac{m_{i,x}}{n_0} = \frac{m_{x0}}{n_0} \cosh(\lambda_i x) \; + \; a_i \sinh(\lambda_i x) \, , \tag{2.25}$$

where

$$\begin{aligned} \frac{m_{x0}}{n_0} = \frac{1}{b}\big[&\Lambda_1\Lambda_2(U_1 - U_2)(\cosh(\lambda_1 L_1) - 1)(\cosh(\lambda_2 L_2) - 1) \\ &+ \; \Lambda_1 U_1(\cosh(\lambda_1 L_1) - 1) \; - \; \Lambda_2 U_2(\cosh(\lambda_2 L_2) - 1)\big] \, , \end{aligned} \tag{2.26}$$

$$\begin{aligned} a_1 = \frac{1}{b}\Bigg[&\Lambda_1\Lambda_2(U_1 - U_2)\sinh(\lambda_1 L_1)(\cosh(\lambda_2 L_2) - 1)) \\ &+ \; \Lambda_1 U_1 \sinh(\lambda_1 L_1) \; + \; \frac{\gamma_1}{\gamma_2}\Lambda_2 U_2 \sinh(\lambda_2 L_2)\Bigg] \, , \end{aligned} \tag{2.27}$$

$$\begin{aligned} a_2 = \frac{1}{b}\Bigg[&\Lambda_1\Lambda_2(U_2 - U_1)\sinh(\lambda_2 L_2)(\cosh(\lambda_1 L_1) - 1)) \\ &+ \; \frac{\gamma_2}{\gamma_1}\Lambda_1 U_1 \sinh(\lambda_1 L_1) \; + \; \Lambda_2 U_2 \sinh(\lambda_2 L_2)\Bigg] \, , \end{aligned} \tag{2.28}$$

$$\begin{aligned} b = &\frac{d}{\gamma_1}\Lambda_1 U_1 \sinh(\lambda_1 L_1)(1 + \Lambda_2(\cosh(\lambda_2 L_2) - 1)) \\ &+ \; \frac{d}{\gamma_2}\Lambda_2 U_2 \sinh(\lambda_2 L_2)(1 + \Lambda_1(\cosh(\lambda_1 L_1) - 1)) \, , \end{aligned} \tag{2.29}$$

$$\lambda_i = \frac{\sqrt{d-1}}{\delta_i}\sqrt{1 + \frac{Pe_i}{d(d-1)}} \, , \tag{2.30}$$

$$\gamma_i = \sqrt{\frac{d}{1 + \dfrac{d(d-1)}{Pe_i}}} \, , \tag{2.31}$$

$$\Lambda_i = \frac{1}{1 + \dfrac{Pe_i}{d(d-1)}} \,. \tag{2.32}$$

Here, n_0 and m_{x0} are the number density and polar order at the step change in transport properties ($x = 0$). In order to determine the value of n_0, the particle conservation equation $\langle n \rangle = \int_{-L_1}^{L_2} n \, dx/(L_1 + L_2)$ is used for given overall number density $\langle n \rangle$.

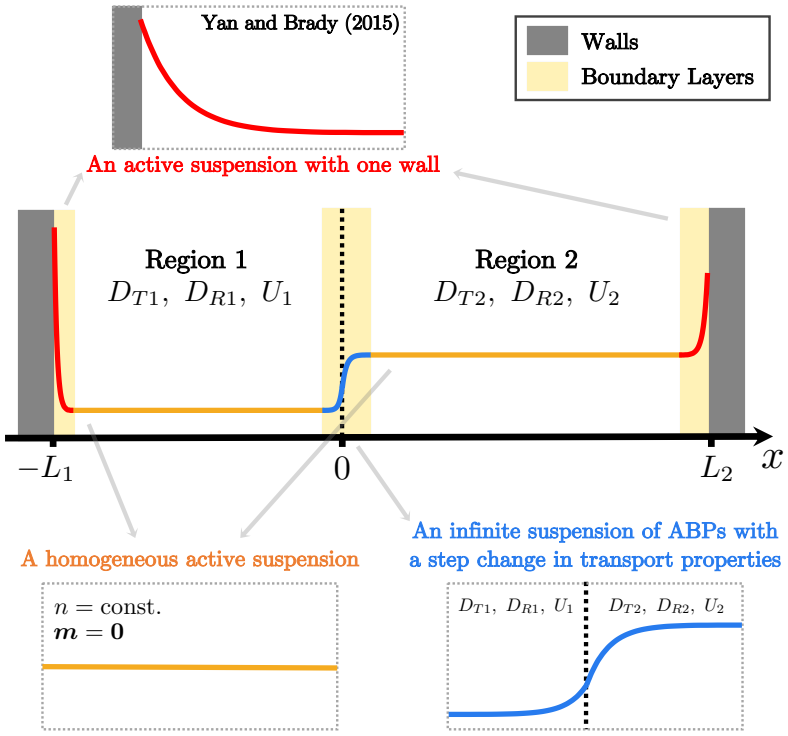

Figure 2.8: A schematic of the singular perturbation analysis with matched asymptotic expansions when the length of a region is much larger than the boundary-layer thickness $L_i \gg D_{Ti}/U_i$. Red lines represent the number density in boundary layers near the walls. The leading order solution insided the boundary layers has been obtained by Yan and Brady [15] for the number density of ABPs near a wall. The blue line represents the number density in the boundary layer where transport properties change. To leading order, the suspension can be treated as an infinite suspension with a step change in transport properties inside the boundary layer at $x = 0$. The number densities in the boundary layers are matched with number densities in the bulk, or outer regions, where the number density is constant to leading order.

The resulting formula, however, is not particularly illuminating and difficult to evaluate because of the sharp boundary layers at both walls and at the point of discontinuity in properties. Instead, a singular perturbation analysis with three

boundary layers of thickness $O(\ell Pe^{-1} = D_T/U)$ is used along with the overall conservation of number density to obtain solutions at all positions between the walls to obtain a more intuitive and simpler analytical solution as described in Fig. 2.8. In the singular perturbation, we recognize that there are boundary layers at the point of discontinuity in properties ($x = 0$) and at each wall where rapid variations in number density and polar order occur. When the length of a region L_i is large compared to the boundary-layer thickness $O(D_T/U)$, the full solution that is valid for all positions can be constructed by piecing together the boundary layers.

The leading order inner solutions within boundary layers near walls have been obtained by Yan and Brady [15] as solutions for semi-infinite suspensions with one wall. Also, the analytical solution (2.9)-(2.14) for an infinite suspension with a step change in transport properties is the leading order inner solution inside the boundary layer at $x = 0$. The outer solutions far from boundary layers are homogeneous to leading order: $n = n_i^{bulk}$(const.) and $\boldsymbol{m} = \mathbf{0}$. By matching inner and outer asymptotic solutions, we obtain a complete solution:

$$\frac{n_i}{n_i^{bulk}} = 1 + \frac{1}{d(d-1)} Pe_i e^{-\lambda_i(L_i \pm x)} + \frac{C_i(U_1 - U_2)}{\pm\left(\dfrac{U_1}{C_1} + \dfrac{U_2}{C_2}\right) - C_i(U_1 - U_2)} e^{\pm\lambda_i x} , \tag{2.33}$$

$$\frac{m_{i,x}}{n_i^{bulk}} = \frac{1}{\sqrt{d}C_i}\left[\mp \frac{1}{d(d-1)} Pe_i e^{-\lambda_i(L_i \pm x)} + \frac{C_i\,(U_1 - U_2)}{\left(\dfrac{U_1}{C_1} + \dfrac{U_2}{C_2}\right) \mp C_i(U_1 - U_2)} e^{\pm\lambda_i x} \right] , \tag{2.34}$$

$$\frac{n_1^{bulk}}{n_2^{bulk}} = \frac{\left(\dfrac{U_1}{C_1} + \dfrac{U_2}{C_2}\right) - C_1(U_1 - U_2)}{\left(\dfrac{U_1}{C_1} + \dfrac{U_2}{C_2}\right) + C_2(U_1 - U_2)} , \tag{2.35}$$

where λ_i and C_i are the same as in (2.13) and (2.14). The bulk number densities n_1^{bulk} and n_2^{bulk} are determined by the conservation of particles:

$$\int_{-L_1}^{0} n_1 \, dz + \int_{0}^{L_2} n_2 \, dz = (L_1 + L_2)\langle n \rangle . \tag{2.36}$$

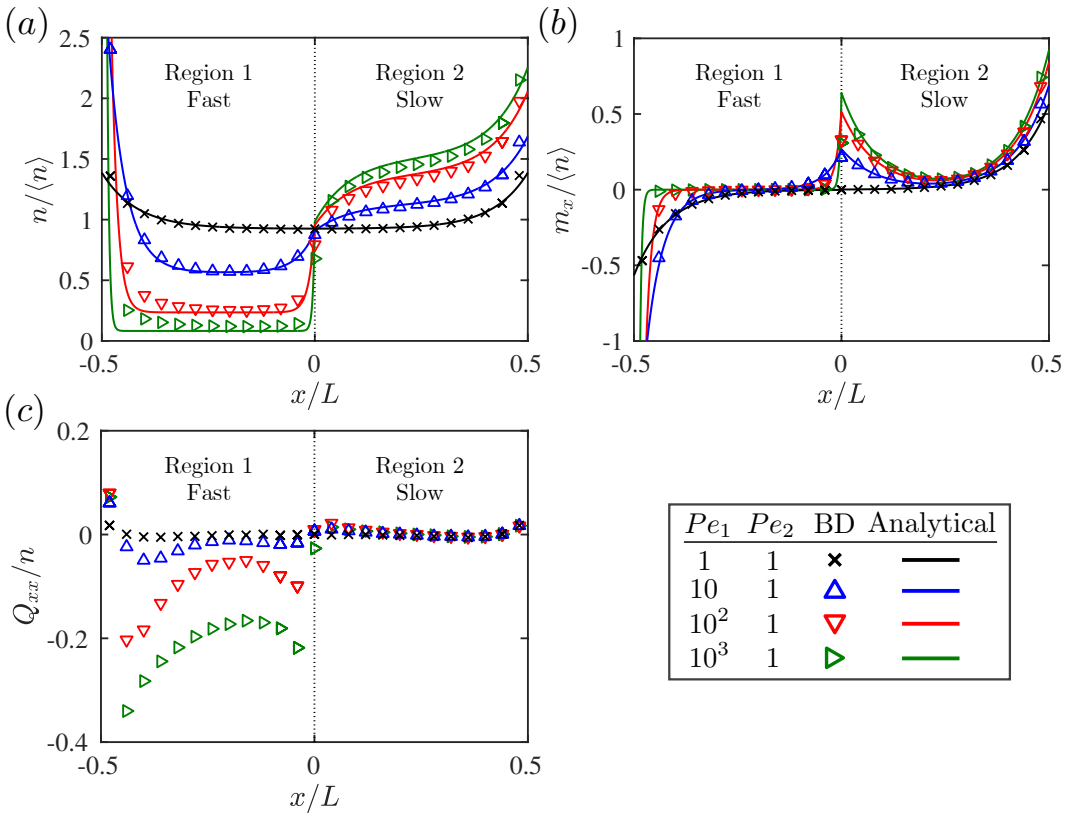

Figure 2.9: (a) Number densities, (b) polar orders, and (c) nematic orders of ABPs confined between parallel walls when transport properties abruptly changes at $x = 0$. The number densities and polar orders are scaled with the overall number density $\langle n\rangle$ and the nematic orders are scaled with the local number densities: $Q_{xx}/n = \langle q_x^2\rangle - 1/2$. Markers are BD simulations and lines are analytic solutions obtained by a singular perturbation analysis (2.33)-(2.36). In all cases, the two regions have the same translational and rotational diffusivities and length ($L/2$), but the swim speeds differ: $Pe_1/Pe_2 = (U_1/U_2)^2$. The coordinate x is scaled with L, which is 10 times longer than the microscopic length scale $\delta = \sqrt{D_T\tau_R}$.

Note that the number densities in the two regions n_1^{bulk} and n_2^{bulk} are identical when swim speeds in two regions are the same regardless of the other parameters — the number density is *governed* by swim speed difference.

A comparison of number densities obtained by the singular perturbation solution and BD simulations is shown in Fig. 2.9(a). The slight discrepancy near the walls at high Pe results from the $\boldsymbol{Q}=\boldsymbol{0}$ closure losing accuracy as shown in Fig. 2.9(c), not the invalidity of the singular analysis, which is valid as long as the two regions are larger than the boundary-layer thickness: $L_1 \gg D_{T1}/U_1$ and $L_2 \gg D_{T2}/U_2$. When the activity is high ($Pe > 100$) the nematic field associated with the steep change of

n and $\boldsymbol{m}$ needs to be included in the analysis to improve the accuracy as shown by Yan & Brady [15].

The singular perturbation solution also accurately predicts the polar order shown in Fig. 2.9(b). Since $\boldsymbol{m} \sim \nabla n$ from the number density balance (1.4) there is a peak in polar order at $x = 0$ directed towards the slower region; net advective transport of particles into the slower region is balanced by the diffusive transport due to the number density jump.

Figure 2.9(c) shows that boundary layers of the nematic order develop near the confining walls and near the step change in the swim speed of the particles. The nematic order drops sharply and becomes negative near the walls because most of the particles leave the walls orienting parallel to the walls. The sign of the nematic order also abruptly changes near the step change in swim speed. From the polar order balance (1.6), the nematic order is coupled to the gradient of the polar order by $\boldsymbol{Q} \sim U/D_T \nabla \boldsymbol{m}$ for high Pe. Since the polar order develops a sharp peak near the step change, the nematic order has a shape of the derivative of the sharp peak, which resembles a shape of the derivative of a δ-function.

2.4 Active Suspensions Confined by a Circular Wall

As another example of finite suspensions we consider a suspension confined by a circular or cylindrical container of radius R as described in Fig. 2.10. Transport properties changes abruptly at $r = \Delta R$ and we call the inner part ($r < \Delta R$) region 1 and the outer part ($\Delta R \leq r < R$) region 2. Again, the governing Smoluchowski equations (2.2)-(2.4), associated moment equations (2.5)-(2.8), and continuity of field variables and fluxes at the boundary of the two regions ($r = \Delta R$) still apply. The hard circular wall does not allow particles to pass through and the no-flux boundary condition $\boldsymbol{n} \cdot \boldsymbol{j}_T = 0$ is applied at $r = R$.

As in the previous example with planar walls the steady state analytical solution with the $\boldsymbol{Q} = \boldsymbol{0}$-closure can be easily obtained but it is not very elucidating and difficult to compute numerically. Again it is more instructive to perform a singular perturbation analysis with two boundary layers with the overall conservation of number density. The two boundary layers develop at the step change in the transport properties ($r = \Delta R$) and at the wall ($r = R$). The matched asymptotic expansion obtained by piecing together the two boundary layers is valid for the whole domain as long as the size of the suspension R is large compared to the boundary-layer thickness $O(D_T/U)$.

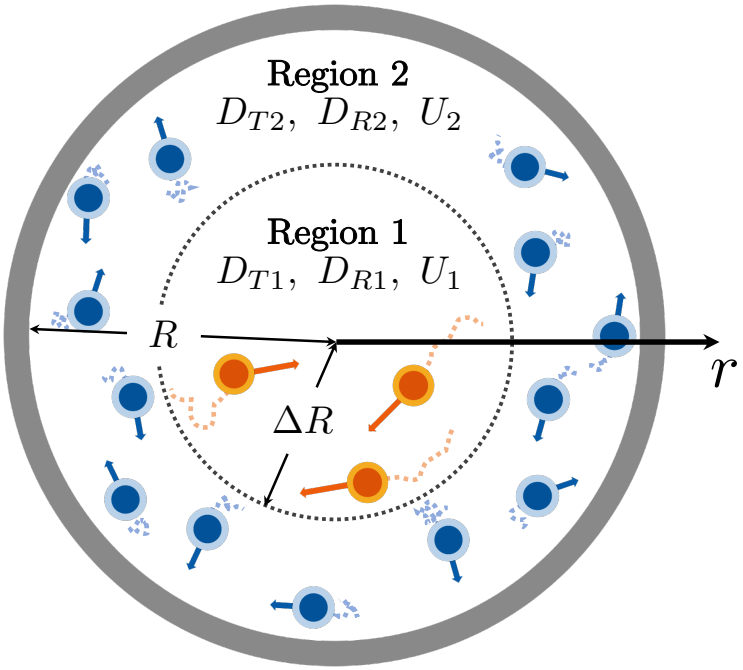

Figure 2.10: A schematic of a suspension of ABPs with an abrupt change in activity bounded by a circular wall of radius R. In regions 1 ($r < \Delta R$; $0 < \Delta < 1$) and 2 ($\Delta R \leq r < R$) the ABPs have swim speeds U_i, translational diffusivities D_{Ti}, and rotational diffusivities D_{Ri}, where the subscript i (= 1 or 2) represents the index of a region.

In order to describe the boundary layer at $r = \Delta R$ generated by the jump in transport properties, an infinite suspension with the same jump is considered — imagine the circular wall is removed from Fig. 2.10 and region 2 is everywhere outside the region 1 ($\Delta R \leq r$). For this infinite domain problem, all the equations and conditions remain the same except for the no-flux boundary condition at the wall. Instead of the no-flux condition the suspension is now homogeneous and random far from the abrupt change at $r = \Delta R$ i.e. $n_2 \to n_2^\infty$ and $\boldsymbol{m}_2 \to \mathbf{0}$ as $r \to \infty$. The overall number density $\langle n \rangle$ is defined by $\int_0^L \langle n \rangle\, r dr = \int_0^{\Delta R} n_1\, r dr + \int_{\Delta R}^L n_2\, r dr$ as $L \to \infty$ and therefore $\langle n \rangle = n_2^\infty$. The steady state analytical solution is easily obtained with the $\boldsymbol{Q} = \mathbf{0}$-closure:

$$\frac{n_1}{n_2^\infty} = 1 + \frac{(U_1 - U_2)}{c_{\Delta R}}\Big[\gamma_1[I_0(\lambda_1 r) - I_0(D_1)]K_1(D_2) - \gamma_2 I_1(D_1)K_0(\lambda_2 \Delta R)\Big]\,, \tag{2.37}$$

$$\frac{n_2}{n_2^\infty} = 1 - \frac{(U_1 - U_2)}{c_{\Delta R}}\gamma_2 I_1(D_1)K_0(\lambda_2 r)\,, \tag{2.38}$$

$$\frac{m_{1,r}}{n_2^\infty} = \frac{(U_1 - U_2)}{c_{\Delta R}} K_1(D_2) I_1(\lambda_1 r) \,, \tag{2.39}$$

$$\frac{m_{2,r}}{n_2^\infty} = \frac{(U_1 - U_2)}{c_{\Delta R}} I_1(D_1) K_1(\lambda_2 r) \,, \tag{2.40}$$

where

$$\begin{aligned} c_{\Delta R} = \frac{d}{2}\frac{U_1}{\gamma_1} K_1(D_2)(I_0(D_1) + I_2(D_1)) \; + \; \frac{d}{2}\frac{U_2}{\gamma_2} I_1(D_1)(K_0(D_2) + K_2(D_2)) \\ + \; (U_1 - U_2)\gamma_2 I_1(D_1) K_0(D_2) \,, \end{aligned} \tag{2.41}$$

$$D_i = \lambda_i \Delta R \,. \tag{2.42}$$

Here, $I_{0,1,2}$ and $K_{0,1,2}$ are modified Bessel functions of the first and second kinds and λ_i and γ_i are defined by eqs. (2.30) and (2.31). We note that even with the circular geometry the analytical solution (2.37)-(2.42) again predicts that the number density is governed by the swim speed difference $U_1 - U_2$ regardless other parameters — the suspension is homogeneous if the swim speed does not vary. It is also notable that the simple result nU = constant is recovered for the circular geometry when activity is high ($Pe \gg 1$) and region 1 is sufficiently large ($\Delta R \gg \lambda \sim O(D_T/U)$) by using the leading order asymptotic expansions of the modified Bessel functions, $I(x) \sim e^x/\sqrt{2\pi x}$ and $K(x) \sim e^{-x}/4$ as $x \to \infty$:

$$\frac{n_1(0)}{n_2^\infty} = 1 \; + \; \frac{(U_1 - U_2)}{c_{\Delta R}} \Big[\gamma_1 [1 - I_0(D_1)] K_1(D_2) \; - \; \gamma_2 I_1(D_1) K_0(\lambda_2 \Delta R) \Big] \approx \frac{U_2}{U_1} \,. \tag{2.43}$$

Another boundary layer at the circular wall has been described by Yan and Brady [15] to leading order. Piecing the two boundary layers together, the matched asymptotic expansion gives an analytic solution that is valid for all positions in the circular domain:

$$\frac{n_1}{n_2^{bulk}} = 1 \; + \; \frac{(U_1 - U_2)}{c_{\Delta R}} \Big[\gamma_1 [I_0(\lambda_1 r) - I_0(D_1)] K_1(D_2) \; - \; \gamma_2 I_1(D_1) K_0(\lambda_2 \Delta R) \Big] \,, \tag{2.44}$$

$$\frac{n_2}{n_2^{bulk}} = 1 \; - \; \frac{(U_1 - U_2)}{c_{\Delta R}} \gamma_2 I_1(D_1) K_0(\lambda_2 r) \; + \; \frac{1}{d_{\Delta R,2}} (I_0(\lambda_2 r) - 1) \,, \tag{2.45}$$

$$\frac{m_{1,r}}{n_2^{bulk}} = \frac{(U_1 - U_2)}{c_{\Delta R}} K_1(D_2) I_1(\lambda_1 r) \,, \tag{2.46}$$

$$\frac{m_{2,r}}{n_2^{bulk}} = \frac{(U_1 - U_2)}{c_{\Delta R}} I_1(D_1) K_1(\lambda_2 r) \; + \; \frac{1}{\gamma_2 d_{\Delta R,2}} I_1(\lambda_2 r) \,, \tag{2.47}$$

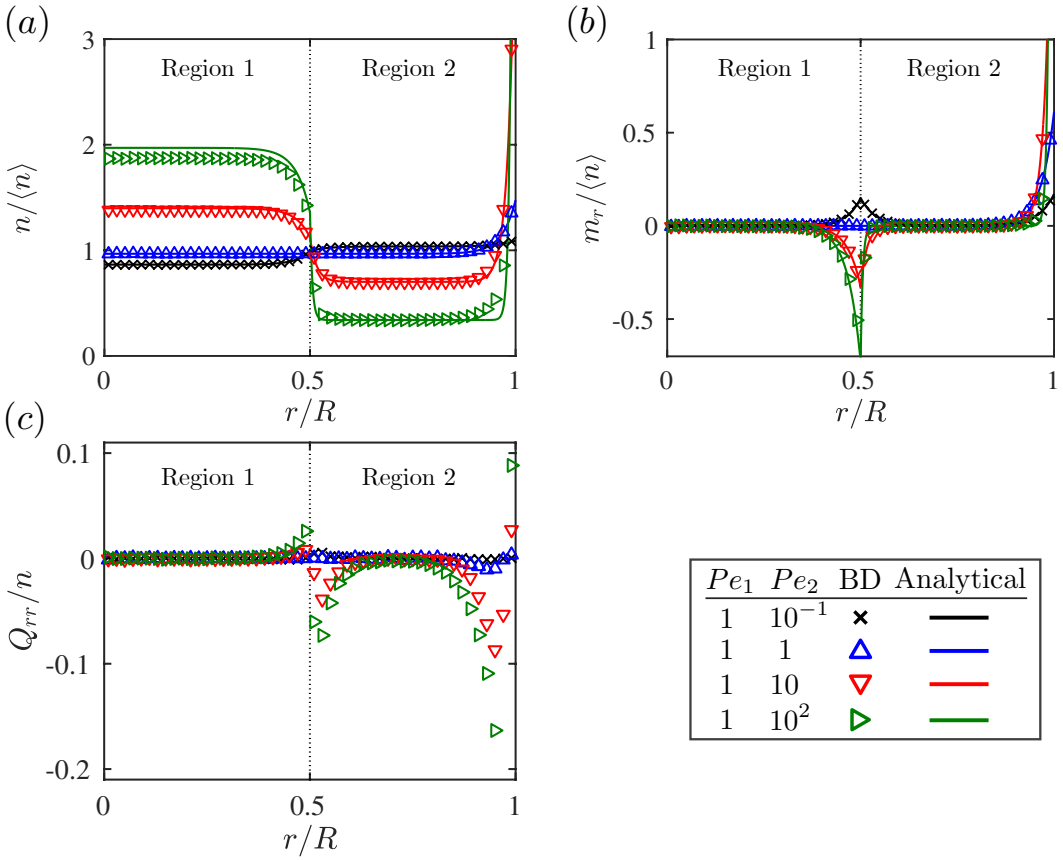

Figure 2.11: (a) Number densities, (b) polar orders, and (c) nematic orders of ABPs confined by a circular wall when transport properties abruptly changes at $r = R/2$. The number densities and polar orders are scaled with the overall number density $\langle n\rangle$ and the nematic orders are scaled with the local number densities: $Q_{rr}/n = \langle q_r^2\rangle - 1/2$. Markers are BD simulations and lines are analytic solutions obtained by a singular perturbation analysis ((2.44)-(2.48)). In all cases, the two regions have the same translational and rotational diffusivities, but the swim speeds differ: $Pe_1/Pe_2 = (U_1/U_2)^2$. The coordinate r is scaled with the radius of the container R, which is 25 times longer than the microscopic length scale $\delta = \sqrt{D_T\tau_R}$.

where

$$d_{\Delta R,2} = 1 + \frac{1}{2}\left(\frac{d(d-1)}{Pe_2} - 1\right) I_0(D_2) + \frac{1}{2}\left(\frac{d(d-1)}{Pe_2} + 1\right) I_2(D_2)\,. \qquad (2.48)$$

The bulk number density in region 2 n_2^{bulk} is determined by the overall conservation of the number density $\langle n\rangle\, R^2/2 = \int_0^{\Delta R} n_1\, r dr + \int_{\Delta R}^{R} n_2\, r dr$.

A comparison of the singular perturbation solution and BD simulations is shown in Fig. 2.11. The number density is always lower in the region with the faster swim speed and the polar order develops toward the region with the slower swim

speed. We once again note that the slight discrepancy in the number density at high $Pe = 10^2$ results from the $\boldsymbol{Q} = \mathbf{0}$-closure used to describe the boundary layers not from the singular perturbation analysis. The singular perturbation solution is valid as long as the sizes of the two regions are larger than the boundary-layer thickness: $\Delta R \gg D_{T1}/U_1$ and $(1-\Delta)R \gg D_{T2}/U_2$. When the activity is high ($Pe > 10^2$) the accuracy can be improved by accounting for the nematic field associated with rapid changes of the number density and polar order inside the boundary layers [15].

2.5 Transient Behavior of Microswimmers with Abrupt Variation in Activity

In the previous sections we demonstrated that the steady-state number density of colloidal active matter is governed by the swim speed difference. We also have shown that the amplitude of the difference in the number densities is bounded above by the relation $nU = \text{const.}$, which holds when particles are purely active, and is modulated by Pe. In this section we explore the transient dynamics of microswimmers released from the position where an abrupt change in transport properties occurs.

The evolution of microswimmers released from a point source is described by the Green's function solution of the Smoluchowski equation (2.2). The Green's function of the Smoluchowski equation when the transport properties of ABPs are uniform throughout a suspension has been studied in several previous works both experimentally [19] and theoretically [20–22] due to its relevance to the growth of bacterial films. One of the most interesting aspects of the dynamics of ABPs is the transition from ballistic wave-like motion in a short ($\ll \tau_R$) time to diffusive motion in a long ($\gg \tau_R$) time.

The transition of the dynamics of ABPs is most clearly seen by considering the first two moments of the probability density function as shown by Dulaney and Brady [20]. By combining the number density and polar order balance equations (1.4)-(1.7) with the $\boldsymbol{Q} = \mathbf{0}$-closure, the number density of purely active particles ($D_T = 0$) satisfies

$$\frac{\partial^2 n}{\partial t^2} + (d-1) D_R \frac{\partial n}{\partial t} = \frac{U_0^2}{d} \nabla^2 n \,, \tag{2.49}$$

which is known as the telegraph equation [23, 24]. A scaling analysis reveals that in a short ($\ll \tau_R$) time scale the second order time derivative dominates the first order time derivative and eq. (2.49) can be approximated as a wave equation. On the other hand in a long ($\gg \tau_R$) time scale the first order time derivative is dominant and the equation becomes a diffusion equation.

Now we consider the geometry used for infinite suspensions with a step change

in the properties in section 2.2 (see Fig. 2.1) in order to study the effect of an abrupt change in transport properties. Since the translational diffusivity just smears out spatial gradients, purely active particles ($D_T = 0$) are considered in order to understand the essential physics. The moment equations closed by $\boldsymbol{Q} = \boldsymbol{0}$ are

$$\frac{\partial n_i}{\partial t} + \nabla \cdot \boldsymbol{j}_{n,i} = 0 \,, \quad \boldsymbol{j}_{n,i} = U_i \boldsymbol{m}_i \tag{2.50}$$

$$\frac{\partial \boldsymbol{m}_i}{\partial t} + \nabla \cdot \boldsymbol{j}_{m,i} + (d-1) D_{R,i} \boldsymbol{m}_i = \boldsymbol{0} \,, \quad \boldsymbol{j}_{m,i} = \frac{1}{d} U_i n_i \boldsymbol{I} \,, \tag{2.51}$$

where subscripts i (= 1 or 2) represents the index of regions. We discuss the validity of the assumption $\boldsymbol{Q} = \boldsymbol{0}$ later in this section. For mathematical simplicity we consider an instantaneous infinite line source of particles with random orientations. The particles are initially located at at the interface of the two regions ($x = 0$) and released at $t = 0$. The corresponding initial conditions are $n_1 = n_2 = \delta(x)$ and $\boldsymbol{m}_1 = \boldsymbol{m}_2 = \boldsymbol{0}$ at $t = 0$. Also at the interface the fluxes are continuous: $n_1 U_1 = n_2 U_2$ and $\boldsymbol{m}_1 U_1 = \boldsymbol{m}_2 U_2$ at $x = 0$. Finally particles swim into an infinite free space so $n_i \to 0$ and $\boldsymbol{m}_i \to \boldsymbol{0}$ as $|x| \to \infty$. The associated telegraph equation for each region is

$$\frac{\partial^2 n_i}{\partial t^2} + (d-1) D_{R,i} \frac{\partial n_i}{\partial t} = \frac{U_i^2}{d} \nabla^2 n_i \,. \tag{2.52}$$

For the telegraph equation (2.52) the initial and boundary conditions for the polar order should be rewritten in terms of the number density. From eq. (2.50) the initial condition for the polar order can be expressed as an initial condition for the number density $\partial n_i / \partial t = 0$ at $t = 0$. Also by integrating eq. (2.50) over each region and using the boundary condition for the polar order, we obtain an integral condition for the particle conservation $N_1 + N_2 = 1$, where $N_1 = \int_{-\infty}^{0} n_1 \, dx$ and $N_2 = \int_{0}^{\infty} n_2 \, dx$ are the fractions of particles in regions 1 ($x < 0$) and 2 ($x \geq 0$).

Laplace transforming the telegraph equation (2.52) in time we obtain

$$s^2 \hat{n}_i + (d-1) D_{R,i} s \hat{n}_i = \frac{U_i^2}{d} \frac{\partial^2 \hat{n}_i}{\partial x^2} \,, \tag{2.53}$$

where $\hat{n}_i(x, s)$ is the transformed number density. The equation is easily solved to give

$$\hat{n}_i(x, s) = \hat{n}_i(0, s) \exp\left(\frac{1}{U_i} \sqrt{d(s^2 + (d-1) D_{R,i} s)} \right) \,. \tag{2.54}$$

In order to check the partitioning of particles we integrate the number density in each region and use the convolution theorem to obtain

$$N_i(t) = \frac{1}{\sqrt{d}} \int_0^t U_i n_i(0, t') \exp\left(-\frac{d-1}{2} D_{R,i} (t - t') \right) I_0\left(\frac{d-1}{2} D_{R,i} (t - t') \right) dt' . \tag{2.55}$$

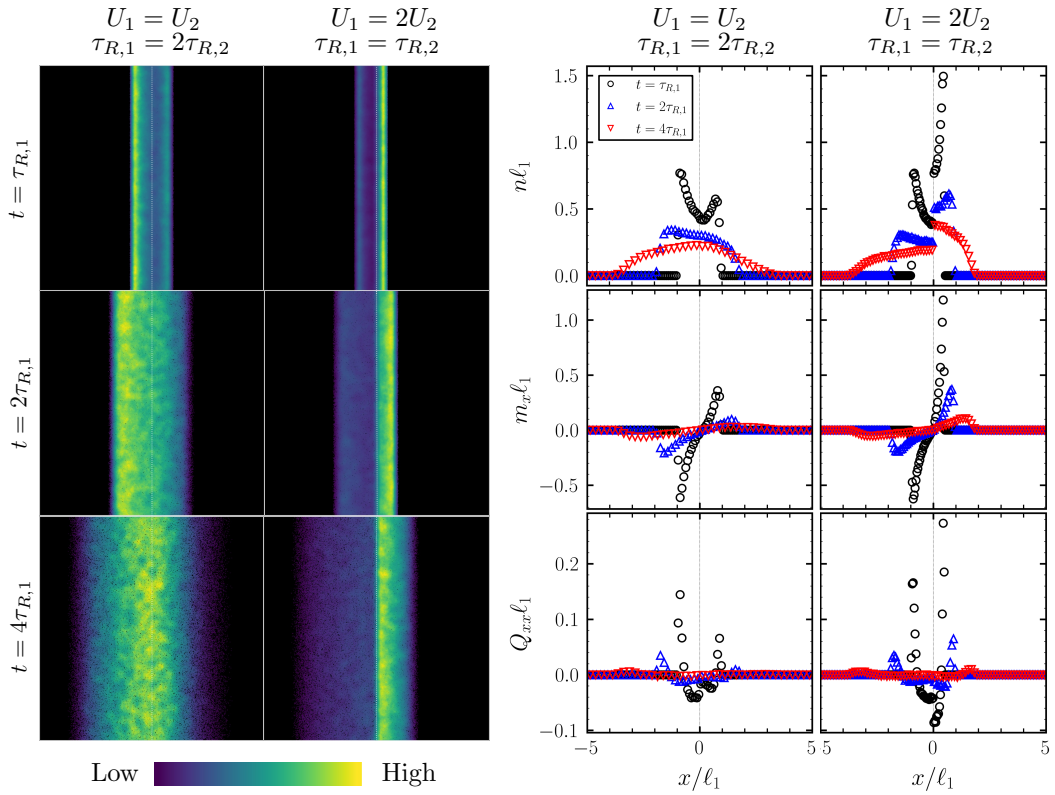

Figure 2.12: (Left) Snapshots from BD simulations of purely active particles released at $t = 0$ from the center (white dashed line) where the reorientation time or swim speed abruptly changes. The colormap shows the local number density of particles. The length of the simulation box is 5 times longer than the run length in region 1 ($x < 0$). (Right) Transient number densities, polar orders, and nematic orders multiplied by the run length in region 1 ℓ_1 obtained by BD simulations when purely active particles released at $t = 0$ from $x = 0$ where the reorientation time or swim speed abruptly changes. The probability density is normalized so that $\int_{-\infty}^{\infty} n\, dx = 1$ and the position is scaled with ℓ_1 as well. The shape of number densities shows transition from wave-like ($t \leq \tau_R$) to diffusion-like ($t > \tau_R$) dynamics. When a step change in the swim speed occurs the even-ordered orientational moments (e.g. n, $\boldsymbol{Q}$, etc.) are discontinuous at the jump for the continuity of the translational flux $\boldsymbol{j}_T = UP\boldsymbol{q}$.

Here, I_0 is a modified Bessel function of the first kind. Since $U_1 n_1 = U_2 n_2$ at the interface ($x = 0$) for the continuity of the polar order flux, eq. (2.55) implies that the particles are partitioned evenly in each region ($N_1 = N_2$) at all time regardless of the swim speeds when the rotational diffusivities in the two regions are the same. The fraction of particles in each region at ($\gg \tau_R$) times is approximated as

$$N_i(t) \approx \frac{1}{\sqrt{d(d-1)\pi D_{R,i}}} \int_0^t \frac{U_i n_i(0,t')}{\sqrt{t-t'}}\, dt', \tag{2.56}$$

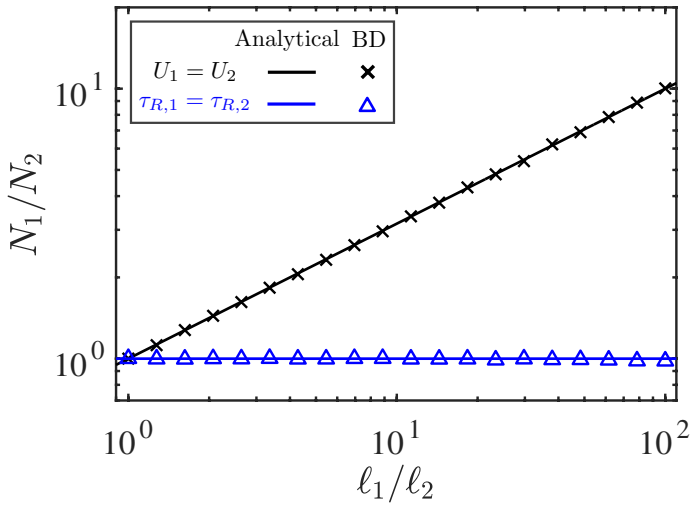

Figure 2.13: The ratio of numbers of purely active particles in the two regions after randomly oriented particles are released at the interface of the two regions with different transport properties. Black and blue represent a step change in the reorientation time ($\ell_1/\ell_2 = \tau_{R,1}/\tau_{R,2}$) and the swim speed ($\ell_1/\ell_2 = U_1/U_2$), respectively. Markers are from BD simulations and lines are the analytical prediction $N_1/N_2 = \sqrt{\tau_{R,1}/\tau_{R,2}}$. In the BD simulations the numbers of particles are measured $\sim 3\tau_{R,1}$ after the release of particles to ensure the values have reached constant.

where we used $I_0(x) \sim e^x/\sqrt{2\pi x}$ as $x \to \infty$. Thus, at long times the ratio of the fractions (or total numbers) of particles in each region is $N_1/N_2 = \sqrt{\tau_{R,1}/\tau_{R,2}}$ — the partitioning of particles is governed by the reorientation time.

This also can be explained by the long-time diffusive behavior of ABPs and the steady state solutions from previous sections. When $t \gg \tau_R$ ABPs effectively diffuse with the swim diffusivity $D^{swim} \sim U^2\tau_R$ and the average (root-mean-square) distance reached by the released particles scales as $\sqrt{D^{swim}t}$. Since the number density of particles approaches the steady state value specified by $nU = $constant, the ratio of the number of particles in each region $N_1/N_2 \sim \sqrt{D_1^{swim}t}U_2/\sqrt{D_2^{swim}t}U_1 = \sqrt{\tau_{R,1}/\tau_{R,2}}$.

We perform BD simulations to verify this prediction. Figure 2.12 shows general shapes of the Green's function when the swim speed or reorientation time abruptly changes at the position where particles are released. Even in transient cases, the number density is an order of magnitude larger than the nematic order allwoing the $\boldsymbol{Q} = \mathbf{0}$-closure for simple predictions at a long ($> \tau_R$) time scale. At a short ($< \tau_R$) time scale different closure methods including the effect of the nematic order are known to give better accuracy [20]. The ratio of number of particles obtained by BD simulations is shown Fig. 2.13 and excellently agrees with the prediction that

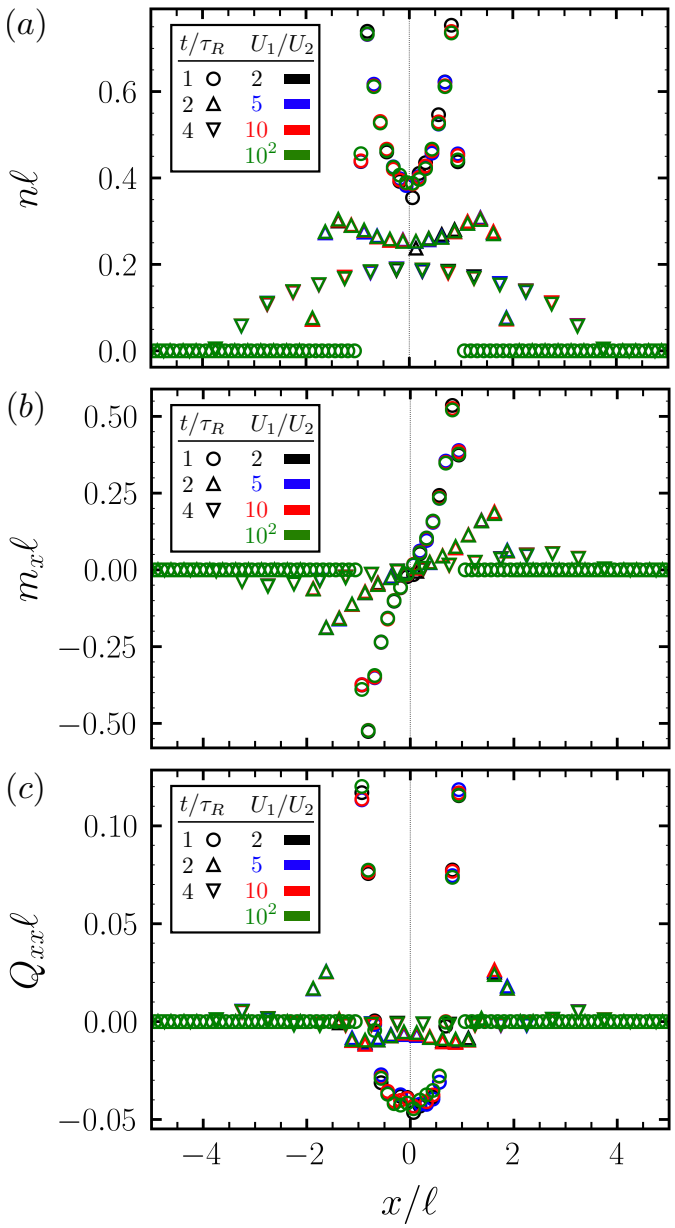

Figure 2.14: BD simulation results of transient (a) number densities, (b) polar orders, and (c) nematic orders multiplied by the local run length versus the position x scaled with the local run length when randomly oriented purely active particles are released from $x = 0$ at $t = 0$. The probability density is normalized so that $\int_{-\infty}^{\infty} n\, dx = 1$ and the reorientation time is the same in the two regions. Even though the swim speeds differ in the two regions, orientational moments of the rescaled density $A = PU$ are symmetric on the domain x/ℓ resulting in the even partitioning of particles. Furthermore, the rescaled solutions are independent of the swim speeds and fall on a single curve as predicted by eqs. (2.57)-(2.59). The style and color of markers represent the time and ratio of swim speeds U_1/U_2, respectively.

$N_1/N_2 = \sqrt{\tau_{R,1}/\tau_{R,2}}$.

We also note that when $\tau_{R,1} = \tau_{R,2}$ the two regions have the same number of particles $N_1 = N_2 = 1/2$ *at all time* regardless of the swim speeds from eq. (2.55). From the number density balance (2.50) $\partial N_i/\partial t = 0$ indicates zero polar order at the interface. The absence of net polar order at $x = 0$ for all time suggests that particles in each region behave as if there were no step change in the swim speed; when there is no variation in the transport properties the symmetry makes the polar order vanish at the position where particles are released. This independent behavior inside each region when the reorientation times are the same can be understood by rewriting the original Smoluchowski equation (2.2)-(2.4) for purely active particles as

$$\frac{\partial A_i}{\partial \bar{t}_i} + \overline{\nabla}_i \cdot \overline{\boldsymbol{j}}_{T,i} + \nabla_q \cdot \overline{\boldsymbol{j}}_{q,i} = 0 \,, \tag{2.57}$$

$$\overline{\boldsymbol{j}}_{T,i} = \boldsymbol{q} A_i \,, \tag{2.58}$$

$$\overline{\boldsymbol{j}}_{q,i} = -\nabla_q A_i \,, \tag{2.59}$$

where $A_i = P_i U_i$, $\overline{\boldsymbol{x}}_i = \boldsymbol{x}/\ell_i$, $\overline{\nabla}_i = \partial/\partial\overline{\boldsymbol{x}}_i$, and $\bar{t}_i = t/\tau_{R,i}$. The initial and boundary conditions are $A_i(x, t = 0) = \delta(x)/\Omega_d$, $\overline{\boldsymbol{j}}_{T,1}(x = 0, t) = \overline{\boldsymbol{j}}_{T,2}(x = 0, t)$, and $A_i \to 0$ as $|x| \to \infty$, where Ω_d is the surface area of the unit d-sphere (e.g. $\Omega_2 = 2\pi$). When $\tau_{R,1} = \tau_{R,2}$ the rescaled governing equations (2.57) in the two regions are identical and the associated initial and boundary conditions result in continuous and symmetric solutions. More importantly, the equation, conditions, and solutions are independent of the swim speeds U_i with the rescaling. Since the problem for homogeneous transport properties i.e. $U_1 = U_2$ is a special case, the Green's function for the homogeneous case [20] can be used as the master curve of the solutions — all the solutions collapse to one curve regardless of the swim speeds in the two regions. BD simulations are performed to confirm the collapse of the solutions and the results are shown in Fig. 2.14. When $\tau_{R,1} = \tau_{R,2}$ regardless of swim speeds in the two regions orientational moments of the rescaled probability density $A = PU$ are symmetric and also fall on a single curve on the rescaled domain $\overline{\boldsymbol{x}} = \boldsymbol{x}/\ell$.

2.6 Conclusions

In this chapter we systematically investigated the effects of an abrupt spatial variation in transport properties in dilute active matter systems. We showed that the steady state distribution of active matter is governed by the swim speed difference and modulated in amplitude by the activity Pe. The number density is always lower in the region with the faster swim speed and the polar order develops toward the

region with the slower swim speed. When particles are highly active ($Pe \gg 1$) the difference in number densities approaches its maximum set by the purely active limit nU = constant. We also showed that the weakly active ABPs ($U_0 > 0$ and $Pe \approx 0$) and passive Brownian particles (PBPs; $U_0 = 0$), which generally show indistinguishable behaviors, can be differentiated by introducing a region with a reference activity to compare.

By performing BD simulations we confirmed that the nematic order is orders of magnitude smaller than the number density for moderate ($Pe < 100$) activities buttressing the utility of the simple $\boldsymbol{Q} = \mathbf{0}$-closure in situations with a step change in transport properties. When the activity is higher, the number density and polar order develop steep gradients and the effects of the associated nematic field need to be included for better accuracy.

We also explored the transient behavior of active matter released at a step change in transport properties to show that the number of purely active particles in the two regions is governed only by the reorientation time. Active particles tend to move more to the region with the longer reorientation time and the number of particles in each region is proportional to $\sqrt{\tau_R}$. When the reorientation time is uniform throughout a suspension the Smoluchowski equation can be rescaled to be swim-speed-free and the transient distributions fall on a single symmetric master curve regardless of the swim speeds in the two regions.

In the following chapter, we consider the mechanics of the problems we discussed in the current chapter and reveal more important consequences of spatially varying transport properties in active matter systems.

2.7 Appendix: Brownian Dynamics Simulations of Active Brownian Particles

The Brownian Dynamics (BD) simulation is a numerical solution of the overdamped Langevin equations. For active Brownian particles the equations are given by

$$\mathbf{0} = -\zeta \boldsymbol{U}_\alpha + \boldsymbol{F}_\alpha^{swim} + \boldsymbol{F}_\alpha^{c} + \boldsymbol{F}_\alpha^{B}, \tag{2.60}$$

$$\mathbf{0} = -\zeta_R \boldsymbol{\Omega}_\alpha + \boldsymbol{L}_\alpha^{B}, \tag{2.61}$$

$$\frac{\partial \boldsymbol{q}_\alpha}{\partial t} = \boldsymbol{\Omega}_\alpha \times \boldsymbol{q}_\alpha, \tag{2.62}$$

where $\boldsymbol{U}_\alpha$ and $\boldsymbol{\Omega}_\alpha$ are the translational and angular velocities of particle α. The resistive medium in which the particles move (e.g. a fluid) exert translational and rotational drag forces and torques: $-\zeta \boldsymbol{U}_\alpha$ and $-\zeta_R \boldsymbol{\Omega}_\alpha$, respectively. Each individual

particle α has its self-propulsive swim force $\boldsymbol{F}_\alpha^{swim} = \zeta U_0 \boldsymbol{q}_\alpha$, where U_0 is the free-space swim velocity and $\boldsymbol{q}_\alpha$ is the direction of swimming. The interparticle collisional force on particle α is $\boldsymbol{F}_\alpha^c$. In dilute suspensions of ABPs interactions between particles are rare and the interparticle forces can be neglected. The random Brownian force/torque are $\boldsymbol{F}_\alpha^B$ and $\boldsymbol{L}_\alpha^B$, with the white noise statistics:

$$\overline{\boldsymbol{F}_\alpha^B(t)} = \boldsymbol{0},\ \overline{\boldsymbol{F}_\alpha^B(t)\boldsymbol{F}_\beta^B(t')} = 2\zeta^2 D_T \boldsymbol{I}\delta_{\alpha\beta}\delta(t-t'), \tag{2.63}$$

$$\overline{\boldsymbol{L}_\alpha^B(t)} = \boldsymbol{0},\ \overline{\boldsymbol{L}_\alpha^B(t)\boldsymbol{L}_\beta^B(t')} = 2\zeta_R^2/\tau_R \boldsymbol{I}\delta_{\alpha\beta}\delta(t-t'). \tag{2.64}$$

Here, $\overline{\cdot}$ represents the ensemble average, D_T is the translational diffusivity, $\delta_{\alpha\beta}$ is the Kronecker delta, and $\tau_R = 1/D_R$ is the reorientation time scale.

The BD simulation is performed by integrating the Langevin equations numerically in time. In chapters 2 and 3 we have used the explicit Euler method with intrinsic error from the numerical method of $O((\Delta t)^2)$. However, errors of $O(\Delta t)$ occur in positions of particles whenever they pass the interface of the two regions with different activities. Therefore, the overall magnitude of error of simulations is $O(\Delta t)$. Our choice of Δt ensures that errors in positions of particles from each step is at most an order of 0.1% of the shortest length scale in the system. For suspensions in bounded domains, we use the potential-free algorithm [25] to compute forces exerted by hard walls. The pressure exerted by particles on a wall is obtained by dividing the total force exerted by particles on the wall with the area (or length in 2D) of the wall.

References

[1] I. Buttinoni, G. Volpe, F. Kümmel, G. Volpe, and C. Bechinger, "Active Brownian motion tunable by light," *J. Phys. Condens. Matter*, vol. 24, no. 28, p. 284 129, Jul. 2012.

[2] J. M. Walter, D. Greenfield, C. Bustamante, and J. Liphardt, "Light-powering Escherichia coli with proteorhodopsin," *Proc. Natl. Acad. Sci.*, vol. 104, no. 7, pp. 2408–2412, Feb. 2007.

[3] N. A. Söker, S. Auschra, V. Holubec, K. Kroy, and F. Cichos, "How activity landscapes polarize microswimmers without alignment forces," *Physical Review Letters*, vol. 126, no. 22, p. 228 001, 2021.

[4] J. Hasnain, G. Menzl, S. Jungblut, and C. Dellago, "Crystallization and flow in active patch systems," *Soft Matter*, vol. 13, no. 5, pp. 930–936, Feb. 2017.

[5] J. Stenhammar, R. Wittkowski, D. Marenduzzo, and M. E. Cates, "Light-induced self-assembly of active rectification devices," *Sci. Adv.*, vol. 2, no. 4, e1501850, Apr. 2016.

[6] G. Frangipane *et al.*, "Dynamic density shaping of photokinetic E. Coli," *Elife*, vol. 7, pp. 1–14, Aug. 2018.

[7] J. Arlt, V. A. Martinez, A. Dawson, T. Pilizota, and W. C. Poon, "Painting with light-powered bacteria," *Nat. Commun.*, vol. 9, no. 1, p. 768, Dec. 2018.

[8] N. Koumakis, A. T. Brown, J. Arlt, S. E. Griffiths, V. A. Martinez, and W. C. Poon, "Dynamic optical rectification and delivery of active particles," *Soft Matter*, vol. 15, no. 35, pp. 7026–7032, 2019.

[9] T. D. Ross, H. J. Lee, Z. Qu, R. A. Banks, R. Phillips, and M. Thomson, "Controlling organization and forces in active matter through optically defined boundaries," *Nature*, vol. 572, no. 7768, pp. 224–229, 2019.

[10] M. J. Schnitzer, "Theory of continuum random walks and application to chemotaxis," *Phys. Rev. E*, vol. 48, no. 4, pp. 2553–2568, 1993.

[11] J. Tailleur and M. E. Cates, "Statistical mechanics of interacting run-and-tumble bacteria," *Phys. Rev. Lett.*, vol. 100, no. 21, p. 218 103, 2008.

[12] M. E. Cates and J. Tailleur, "When are active Brownian particles and run-and-tumble particles equivalent? Consequences for motility-induced phase separation," *Europhys. Lett.*, vol. 101, no. 2, p. 20 010, Jan. 2013.

[13] M. E. Cates and J. Tailleur, "Motility-Induced Phase Separation," *Annu. Rev. Condens. Matter Phys.*, vol. 6, no. 1, pp. 219–244, Mar. 2015.

[14] N. G. van Kampen, "Diffusion in inhomogeneous media," *Zeitschrift für Phys. B Condens. Matter*, vol. 68, no. 2-3, pp. 135–138, Jun. 1987.

[15] W. Yan and J. F. Brady, "The force on a boundary in active matter," *J. Fluid Mech.*, vol. 785, R1.1–R1.11, Dec. 2015.

[16] F. Hecht, "New development in freefem++," *Journal of numerical mathematics*, vol. 20, no. 3-4, pp. 251–266, 2012.

[17] S. C. Takatori and J. F. Brady, "Forces, stresses and the (thermo?) dynamics of active matter," *Curr. Opin. Colloid Interface Sci.*, vol. 21, pp. 24–33, Feb. 2016.

[18] A. K. Omar, Y. Wu, Z.-G. Wang, and J. F. Brady, "Swimming to Stability: Structural and Dynamical Control via Active Doping," *ACS Nano*, vol. 13, no. 1, pp. 560–572, Jan. 2019.

[19] S. C. Takatori, R. De Dier, J. Vermant, and J. F. Brady, "Acoustic trapping of active matter," *Nature communications*, vol. 7, no. 1, pp. 1–7, 2016.

[20] A. Dulaney and J. Brady, "Waves in active matter: The transition from ballistic to diffusive behavior," *Physical Review E*, vol. 101, no. 5, p. 052 609, 2020.

[21] F. J. Sevilla and L. A. G. Nava, "Theory of diffusion of active particles that move at constant speed in two dimensions," *Physical Review E*, vol. 90, no. 2, p. 022 130, 2014.

[22] F. J. Sevilla and M. Sandoval, "Smoluchowski diffusion equation for active brownian swimmers," *Physical Review E*, vol. 91, no. 5, p. 052 150, 2015.

[23] S. Goldstein, "On diffusion by discontinuous movements, and on the telegraph equation," *The Quarterly Journal of Mechanics and Applied Mathematics*, vol. 4, no. 2, pp. 129–156, 1951.

[24] J. Masoliver and G. H. Weiss, "Finite-velocity diffusion," *European Journal of Physics*, vol. 17, no. 4, p. 190, 1996.

[25] D. R. Foss and J. F. Brady, "Brownian Dynamics simulation of hard-sphere colloidal dispersions," *J. Rheol.*, vol. 44, no. 3, pp. 629–651, May 2000.

Chapter 3

REVERSE OSMOTIC EFFECTS IN ACTIVE MATTER

This Chapter includes content from our previously published article:

[1] H. Row and J. F. Brady, "Reverse osmotic effect in active matter," *Physical Review E*, vol. 101, no. 6, p. 062 604, 2020. DOI: 10.1103/PhysRevE.101.062604,

In the preceding Chapter we obtained analytical and numerical solutions to describe distributions of active matter when its transport properties abruptly vary in space. Now we consider the mechanics of the systems and reveal more important consequences of the variation in transport properties. Applying a macroscopic mechanical force balance to active suspensions we find a spatial variation in activity can result a spontaneous reverse osmotic effect in active matter. We show that the reverse osmotic effect can be utilized as a novel way to pump fluid from regions of high concentration to low. We also show that an object in a bath of active particles with spatially varying activity can exhibit a reverse diffusiophoretic motion.

3.1 Particle Phase Pressure on Walls

In order to describe the mechanics of active suspensions, we start by considering the pressure exerted by active particles, or the particle phase pressure. When active matter systems are confined, particles accumulate at the no-flux walls in sharp boundary layers [1] as shown in the preceding Chapter. The number density at a wall n^w can be much higher than in the bulk n^{bulk} depending on the activity $Pe = U^2/(D_T D_R)$. Since particles exert a local osmotic pressure $\Pi^{osmo} = n\zeta D_T = nk_BT$ at each point in space [2], the pressure exerted by active particles is higher on the wall ($\Pi^w = n^w k_B T$) than far from it ($\Pi^{bulk} = n^{bulk} k_B T$). The extra pressure on no-flux boundaries due to the activity is called the swim pressure $\Pi^{swim} = \Pi^w - \Pi^{bulk}$ [1, 3]. (See section 1.3 for more detailed discussions on the swim pressure.)

At high ($Pe \gg 1$) activities, the swim pressure is the dominant contribution to the particle phase pressure at a wall. Since $n^{bulk}U$ is nearly constant for highly active particles as shown in the previous Chapter (see Fig. 2.3), the pressure exerted by particles on the walls $\Pi^w \approx \Pi^{swim} \sim n^{bulk}\zeta D^{swim} \sim \zeta(n^{bulk}U)\ell$ will be different in the two regions if the run lengths are different $\ell_1 \neq \ell_2$.

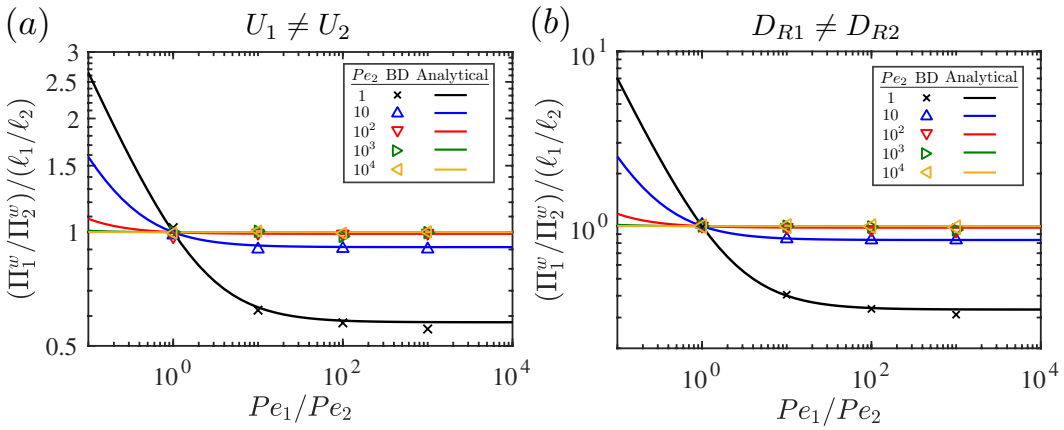

Figure 3.1: The ratio of the pressures exerted by ABPs on wall 1 ($z = -L_1$) and wall 2 ($z = L_2$) scaled with the ratio of corresponding run lengths when an active suspension is bounded by the two parallel walls as described in Fig. 2.7. The transport properties in the two regions are the same except for (a) the swim speed ($Pe_1/Pe_2 = U_1^2/U_2^2$) or (b) the rotational diffusivity ($Pe_1/Pe_2 = D_{R2}/D_{R1}$). The two regions have the same length ($L_1 = L_2$) and the distance between the walls $L = L_1 + L_2$ is 100 times longer than the microscopic length scale $\delta_2 = \sqrt{D_{T2}/D_{R2}}$ in region 2. Markers are from pressures directly measured from BD simulations and lines are from the analytical solution (2.33)-(2.36). In the both cases the ratio of pressures exerted by particles on the walls is ℓ_1/ℓ_2 when activity is high ($Pe \gg 1$)..

To test this prediction, we consider an active suspension bounded by parallel planar walls in section 2.3 (see Fig. 2.7 for a schematic description) and directly measure the pressure exerted by particles on the walls Π^w. In BD simulations we monitor the force transmitted when each APB collides with a wall to compute the pressure. We compare pressures obtained by BD simulations with the pressures computed by $\Pi^w = n^w k_B T$ using the analytical solution (2.33)-(2.36). As shown in Fig. 3.1, the ratio of pressures exerted by ABPs on the two walls is predicted very accurately. At large Pe the pressure is predicted to be linear in the run length, which is borne out precisely as shown in Fig. 3.1.

3.2 Mechanical Description of Active Matter with Spatially Varying Activity

Now we take the whole suspension as a control volume as shown in Fig. 3.2 and consider a macroscopic mechanical force balance on the control volume. If the run length of ABPs differs in the two regions, the pressure exerted the ABPs on the walls is also different. The difference in the particle phase pressures at the walls, however, must be balanced by a difference in pressure in the suspending fluid for otherwise there would be a net force exerted on the container. Active motion is a force-free

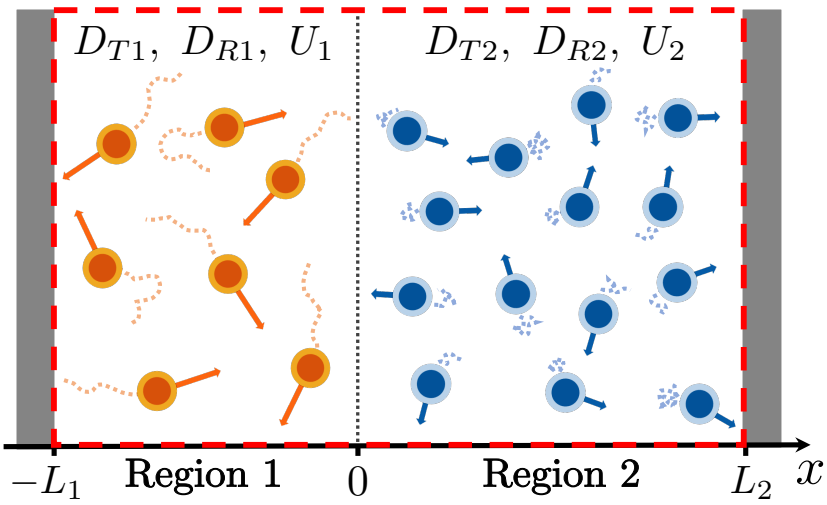

Figure 3.2: A schematic of a suspension of ABPs with an abrupt change in activity confined between two parallel planar walls (see Fig. 2.7 for detailed description of the system). The whole active suspension enclosed by the red dashed box is taken as a control volume. Since ABPs undergo a force-free motion, the net pressure on the left and right (or top and bottom) sides of the control volume must be identical to satisfy a macroscopic mechanical force balance.

motion: particles push off the suspending fluid and their motion is balanced by the fluid drag. A container of active matter cannot exert any net force on its boundary. This is clear for so-called 'wet' active matter — particles immersed in a fluid — but it also applies to 'dry' active matter such as crawling particles who push off a substrate; the combination of particles and substrate is force-free.

The force-free condition requires the total pressure in the suspension to be constant (when there is no flow). The total pressure P is the sum of the local osmotic pressure $\Pi^{osmo} = nk_BT$ exerted by particles and the fluid pressure p_f. Since $P = p_f + nk_BT = \text{const.}$, the fluid pressure distribution is the opposite that of the number density. From the number density balance (1.4), the gradient of the fluid pressure is directly related to the polar order and the flux of the active particles:

$$\nabla p_f = -\zeta U \boldsymbol{m} + \zeta \boldsymbol{j}_n \,. \tag{3.1}$$

Equation (3.1) is a momentum balance on the fluid. The right-hand side is the net hydrodynamic force exerted by active particles on the fluid [4]. The total hydrodynamic force on an individual swimmer $\boldsymbol{F}_\alpha^{hydro} = -\zeta(\boldsymbol{U}_\alpha - \boldsymbol{u}_f) + \zeta U \boldsymbol{q}_\alpha$ consists of the propulsive swim force $\boldsymbol{F}_\alpha^{swim} = \zeta U \boldsymbol{q}_\alpha$ and the fluid drag $\boldsymbol{F}_\alpha^{drag} = -\zeta(\boldsymbol{U}_\alpha - \boldsymbol{u}_f)$. Here, α is the index of each swimmer. Averaging over a continuum

volume element with number density n then gives $n\langle \boldsymbol{F}^{hydro}\rangle = -\zeta \boldsymbol{j}_n + \zeta U \boldsymbol{m}$. The particle flux is $\boldsymbol{j}_n = n(\boldsymbol{u}_p - \boldsymbol{u}_f)$, where $\boldsymbol{u}_p = \frac{1}{N}\sum_\alpha \boldsymbol{U}_\alpha$ is the average particle velocity. The drag force is proportional to the velocity of a particle *relative* to the fluid, $\boldsymbol{U}_\alpha - \boldsymbol{u}_f$, where $\boldsymbol{u}_f$ is the fluid velocity. Only relative motion produces a drag force, a requirement of Galilean invariance.

The fluid momentum balance (3.1) shows that if there is net polar order — a net swim force — in any region this can be balanced by a net particle flux, $\boldsymbol{j}_n = U\boldsymbol{m}$, with $\nabla p_f = 0$, or if there is no particle flux $\boldsymbol{j}_n = 0$, then there must be a fluid pressure gradient, $\nabla p_f \neq 0$.

How can we understand the origin of this fluid pressure gradient? When an active particle moves an equal volume of fluid is displaced in the opposite direction — there is no net mass (or volume) flux for force-free motion. (For 'dry' active matter, when one takes a step an equivalent amount of ground 'moves' in the opposite direction.) Out in the bulk where particles are swimming randomly and there is no polar order, there is no net flux of material across any plane. At a no-flux boundary the active particle's velocity normal to the boundary is zero; the force from the boundary balances the swim force. However, the particle has not stopped its 'swim strokes' and thus is still displacing fluid away from the boundary. Since the fluid does not exit (or enter) the boundary there must be a fluid pressure difference between the wall and the bulk to shut off the flow generated by the active swimming.

This is easily seen from the solution for the concentration and polar order adjacent to a plane wall. From [1] $m_z = -\frac{1}{6}n^{bulk}\ell\lambda e^{-\lambda z}$, where the accumulation boundary layer thickness $\lambda^{-1} = \delta/\sqrt{2(1+D^{swim}/D_T)}$. From (3.1) $\partial p_f/\partial z = -\zeta U m_z = n^{bulk}\zeta U\ell\lambda e^{-\lambda z}/6$ and thus $p_f^w - p_f^{bulk} = -n^{bulk}\zeta D^{swim}$. The drop in fluid pressure at the wall is precisely equal to the swim pressure exerted by the active particles on the boundary. The total pressure $P = p_f^w + n^w k_B T = p_f^{bulk} + n^{bulk} k_B T$ is constant at each location and there is no net flux of particles or fluid in the system.

A fluid pressure jump occurs not just adjacent to no-flux walls, but also at a point of discontinuity in the swim speed. As seen in Fig. 2.9(b), there is net polar order across the interface pointing into the slower region and a jump in concentration and thus a jump in the osmotic pressure. Since the overall pressure is constant, the jump in fluid pressure $\Delta p_f = p_{f1}^{bulk} - p_{f2}^{bulk} = (n_2^{bulk} - n_1^{bulk})k_B T = (n_1^{bulk} + n_2^{bulk})k_B T(U_1 - U_2)/(U_1 + U_2)$, where we have made use of nU = constant. A fluid pressure difference arises from a difference in swim speeds.

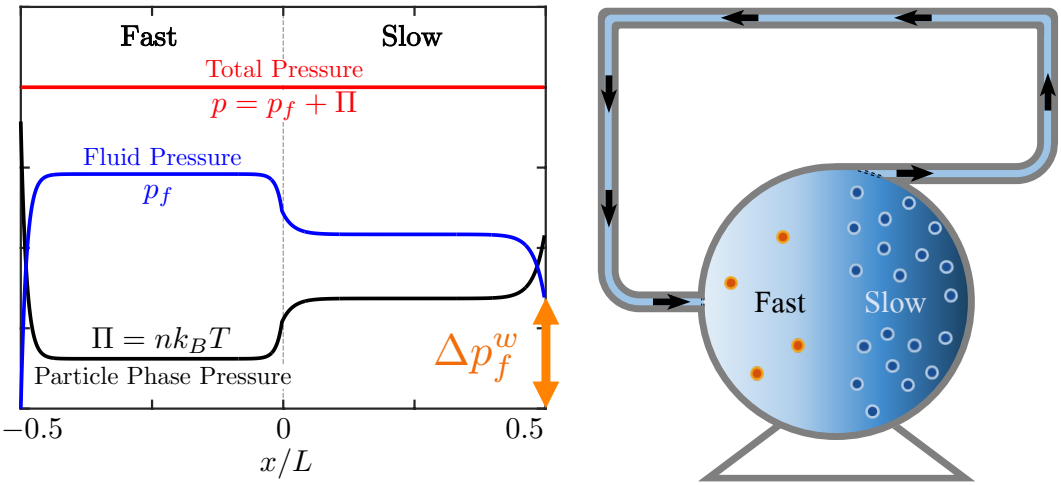

Figure 3.3: (Left) A schematic of the pressure distributions. The pressure exerted by active particles $\Pi = nk_BT$ on a wall is larger in the region with the faster swim speed. Since the total pressure p in a force-free active suspension is constant for a mechanical force balance, the fluid pressure p_f is lower at the wall in the region with the faster swim speed generating a fluid pressure difference at the two walls Δp_f^w. (Right) A schematic of a novel pumping device powered by the activity of suspended particles. When two regions with different swim speeds are connected by a tube and the walls are semi-permeable membranes, the fluid pressure difference Δp_f^w will generate a flow of fluid from the slower to the faster region — from regions of high concentration to low!

3.3 Reverse Osmotic Effect in Active Matter

Now suppose that instead of an impermeable wall, the no-flux boundaries are semi-permeable membranes allowing passage of fluid but not particles. Active particles accumulated at the membranes can act, via their swim strokes, as a pump for the fluid. This pumping action is illustrated in Fig. 3.3. Because the run length in the fast region is larger than in the slow region, the concentration at the fast boundary exceeds that at the slow boundary, $n_1^w > n_2^w$, even though the *bulk* concentration is lower, $n_1^{bulk} < n_2^{bulk}$. Thus, the fluid pressure at the fast wall is less than at the slow wall, $p_{f1}^w < p_{f2}^w$, and fluid will be sucked into the container at the fast wall and ejected at the slow wall. From the perspective of the bulk concentration this appears to be a *reverse osmotic* effect — fluid is sucked into the region with the *lower* concentration!

The speed of the pumped fluid can be estimated as follows. Since the difference in fluid pressure balances the difference in swim pressure, $|\Delta p_f^w| = |\Delta \Pi^w| \approx \zeta \langle n \rangle U_h |\Delta \ell| / (d(d-1))$ for highly active ($Pe \gg 1$) particles, where $U_h = 2(U_1^{-1} + U_2^{-1})^{-1}$ is the harmonic mean of the swim speeds in the two regions and $\Delta \ell$ is the

difference in run lengths. For spherical active particles of radii a and Stokes drag coefficient $\zeta = 6\pi\eta a$, $|\Delta p_f| = (3/4)\eta\phi U_h|\Delta\ell|/a^2$, where ϕ is the averaged volume fraction of suspended particles and η is the fluid viscosity. The pressure drop $|\Delta p_m|$ across a semi-permeable membrane is estimated by Darcy's law: $|\Delta p_m| = \eta Q R_m$, where Q is volume flow-rate and $R_m = L_m/(\kappa A_m)$ is the resistance of the membrane, κ is the permeability of the membrane, A_m is the area, and L_m is the membrane thickness. Assuming a cylindrical-shaped connecting tube and laminar flow, the pressure drop across the tube is $|\Delta p_t| = \eta Q R_t$, where $R_t = 8L_t/(\pi r_t^4)$ is the resistance of the tube and L_t and r_t are the length and radius of the tube. Finally, we obtain the average flow speed in the tube u_t from $Q = \pi r_t^2 u_t = 3\phi U_h|\Delta\ell|/(8R_m + 4R_t)$. If the tube is not too narrow ($\ll 1cm$) nor long ($\gg 1m$), the resistance of membranes — $L_m/\kappa \sim 10^9 m^{-1}$ for Nuclepore membranes with pore diameter of $1\mu m$ and even larger for smaller pores [5] — usually dominates, so we can approximate $u_t \approx 3\phi U_h|\Delta\ell|/(8\pi R_m r_t^2)$. For a suspension with volume fraction $\phi = 0.2$ for $a = 1\mu m$ and reorientation time $10s$ with two regions with swim speeds $5\mu m/s$ and $10\mu m/s$ with $100cm^2$-wide membranes with $L_m/\kappa \sim 10^9 m^{-1}$, the fluid speed in the tube of radius $1cm$ is $0.1\mu m/s$.

In the above calculation, we assumed that the flow of fluid does not significantly disturb the concentration or pressure distributions within the bulk regions, which is true when $Pe_U = u_c L/D^{swim} \ll 1$, where u_c is the flow speed in the suspension container (not the tube) and L is the size of the container. If Pe_U is not small, the advective flux $\boldsymbol{u}_c P$ needs to be included in the translational flux $\boldsymbol{j}_T$ of the Smoluchowski equation while the imposed advection speed u_s satisfies a self-consistence condition with the resulting fluid pressure difference from the disturbed distribution. The reverse osmotic flow can persist even though the fluid flow alters the distribution of active particles, and thus pressures [6].

In the following section we use diffusiophoresis as an example to demonstrate that the reverse osmotic effect can result in unexpected consequences that are opposed to our intuition and knowledge.

3.4 Reverse Diffusiophoresis in Active Bath

Diffusiophoresis is a directed motion of a colloidal particle in a solution generated by a concentration gradient of bath or solute particles suspended in the solution. In the classical analysis of diffusiophoresis, a boundary layer analysis is performed near the surface of a phoretic particle using a large separation between the characteristic

length scale of the interactive force b and the size of a phoretic particle $R(\gg b)$. As a leading order result in this 'thin interfacial limit', local interactions between the bath particles and the phoretic particle are encapsulated as the 'slip velocity' of the suspension at the phoretic particle surface. Then a phoretic motion is generated by the slip velocity to maintain the phoretic particle force- and torque-free. When the interactive force is repulsive, e.g. hard-sphere interactions, the resulted phoretic motion is well-known to be down the concentration gradient — from high concentration to low.

Recently Brady [7] has proposed a new continuum formulation of phoretic motion that is broadly applicable both to a passive and active bath. The aim of the current section is to verify an interesting prediction of a reverse diffusiophoresis in [7] — phoretic motion against the concentration gradient even though the interaction is purely repulsive — which is directly related to the reverse osmotic effect in active matter discussed in the preceding section. Here, we briefly highlight the essence of the new approach.

Instead of performing the boundary layer analysis, Brady utilizes the reciprocal theorem for Stokes flow to obtain a general formula for the phoretic velocity $\boldsymbol{U}$ that is applicable to phoretic particles of arbitrary shape and interactive forces of any range and type. This formulation offers a new alternative perspective, in a nutshell, that the phoretic motion is fundamentally powered by interactive or osmotic force exerted by bath particles but in a reduced amount due to suspending fluid — the osmotic force is not entirely transmitted to the phoretic particle because it is also used to move fluid.

The new perspective is most clearly seen by an expression for the phoretic velocity in a bath of hard-spheres of radius b,

$$\boldsymbol{U} = -\boldsymbol{R}_{FU}^{-1} \cdot \int_{S_c} (\boldsymbol{I} - \mathcal{U}_U) \cdot \boldsymbol{n}\Pi \, dS + \boldsymbol{R}_{FU}^{-1} \cdot \boldsymbol{F}^{ext} \,, \tag{3.2}$$

where $\boldsymbol{R}_{FU}$ is the hydrodynamic resistance tensor coupling the force and the velocity of the phoretic particle, S_c is contact surface between the phoretic and bath particles, $\mathcal{U}_U$ is a second-order tensor that gives the fluid velocity $\mathcal{U}_U \cdot \boldsymbol{U}$ when the phoretic particle translates at a uniform velocity $\boldsymbol{U}$ in a quiescent fluid, $\boldsymbol{n}$ is a outward unit normal to the phoretic particle surface, $\Pi = nk_BT$ is the osmotic pressure of bath particles, and $\boldsymbol{F}^{ext}$ is the external force on the phoretic particle. Equation (3.2) plainly shows that the amount of force expended by the phoretic motion is reduced from the total osmotic force $\boldsymbol{F}^{osmo} = -\int_{S_c} \boldsymbol{n}\Pi \, dS$ because the osmotic force is also

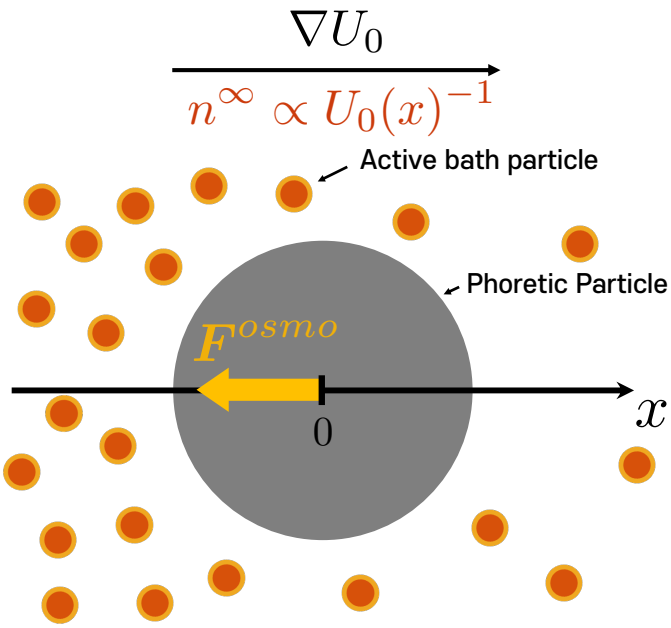

Figure 3.4: A schematic of reverse diffusiophoresis in a bath of active hard-spheres. When the swim speed U_0 of highly active ($Pe \gg 1$) bath particles varies spatially, the number density is lower in the faster than in the slower region satisfying $nU_0 \approx$ constant. Due to the reverse osmotic behavior of active particles, the osmotic pressure at the contact surface $\Pi|_{S_c} \propto \ell_0$ is higher on the lower concentration side. The resulted phoretic motion is from regions of low concentration to high even though interparticle interactions are repulsive: the reverse diffusiophoresis.

consumed to generate a fluid flow especially near the no-slip surface of the phoretic body. It is important to note that eq. (3.2) is generally applicable both to passive and active bath particles.

For a spherical phoretic particle of radius R, eq. (3.2) becomes

$$\boldsymbol{U} = -\frac{L(R_c)}{\zeta_R} \oint_{r=R_c} \Pi \boldsymbol{n}\, dS + \frac{1}{\zeta_R} \boldsymbol{F}^{ext}\,, \tag{3.3}$$

where $R_c = R + b$ is the contact radius, $L(R_c) = 3\Delta^2(1 + 2\Delta/3)/(2(1 + \Delta)^3)$ is the hydrodynamic mobility function introduced by Brady in [8], $\Delta = b/R$, and $\zeta_R = 6\pi\eta R$ is the Stokes drag coefficient of the phoretic particle. Equation (3.3) recovers the classical thin interfacial limit when $\Delta \ll 1$ and the freely draining model, in which hydrodynamic interactions are neglected and hence the entire osmotic force is transmitted to the phoretic particle, when $\Delta \gg 1$. In the both cases, the direction of the phoretic motion aligns with the total osmotic force $\boldsymbol{F}^{osmo} = -\oint_{r=R_c} \Pi \boldsymbol{n}\, dS$ on the phoretic body.

In a classical diffusiophoresis problem a concentration gradient of passive Brownian bath particles is externally imposed to break the symmetry of the osmotic force density at the contact surface. It can be easily shown that the osmotic pressure of passive bath particles at the contact surface is larger on the high-concentration side. Consequently, the direction of the total osmotic force, and hence the phoretic motion induced by repulsive hard-sphere interactions, is down the concentration gradient.

When bath particles are active, however, a concentration gradient need not be maintained by external measures. As shown in Chapter 2, the number density at steady state can be inhomogeneous by itself when the swim speed spatially varies in the suspension. Moreover, in this case, the osmotic pressure exerted by the active bath particles is smaller on the high-concentration side — the reverse osmotic effect — as shown in the preceding section (see Fig. 3.1(a)). The resulted phoretic motion is then against the number density gradient even though interactions are purely repulsive: *the reverse diffusiophoresis*. Brady [7] predicts that the total osmotic force, and hence the reverse diffusiophoretic speed, is linearly proportional to the gradient of swim speed evaluated at the center of the phoretic particle ($\boldsymbol{x} = \boldsymbol{0}$) when the bath particles are highly active ($Pe = U_0^2/(D_R D_R) \gg 1$) and the spatial variation occurs slowly ($\nabla \ell_0 \ll 1$):

$$\boldsymbol{F}^{osmo} = -\oint_{r=R_c} \Pi_\infty^{swim} \boldsymbol{n}\, dS \approx -\frac{\zeta \Omega_d R_c^d}{d^2(d-1)} n^\infty(0) U_0(0) \nabla \ell_0(0)\,, \tag{3.4}$$

where Ω_d is the surface area of the unit d-sphere (e.g. $\Omega_2 = 2\pi$) and super- and sub-scripted ∞ indicates background values in the absence of a phoretic particle.

To test this prediction we performed BD simulations and computed the total osmotic force on the phoretic body inside a bath of purely active particles with linear gradient of swim speed. In the simulations we measure the force on a fixed particle in the active bath instead of letting it move freely. From eq. (3.3) this is equivalent to applying the external force F_{ext} (e.g. optical tweezer) to make the phoretic velocity $\boldsymbol{U} = \boldsymbol{0}$. Here, we assume that the number density distribution of active bath particles is not significantly altered by fixing the phoretic particle. We also assume that a fluid flow generated by the local osmotic force can be neglected. These are standard assumptions in the analysis of phoresis, which are valid when the phoretic speed $U/U_0 \ll 1$.

Figure 3.5 shows that the BD simulation results agree with Brady's prediction. The total osmotic force has a sign opposite to the swim speed gradient, which indicates that the force is directed towards regions of slower swim speed where the number

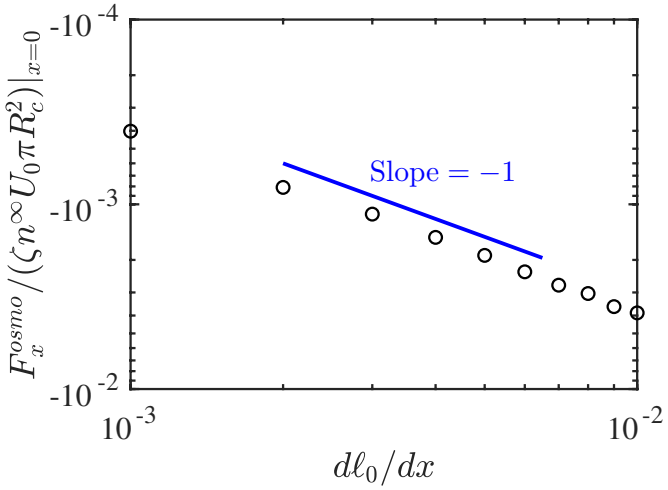

Figure 3.5: The total osmotic force $\boldsymbol{F}^{osmo} = -\oint_{r=R_c} \Pi \boldsymbol{n}\, dS$ on a circular phoretic body fixed at $x = 0$ in a bath of purely active particles versus the linear swim speed gradient dU_0/dx of active bath particles. The osmotic force is scaled with the product of the swim force $\zeta U_0(0)$, background number density $n^\infty(0)$ at the center of the phoretic particle, and area pervaded by the phoretic particle and the swim speed gradient is scaled with the rotational diffusivity. The contact radius R_c is 10 times longer than the run length at the center $\ell_0(0)$. The results obtained by the BD simulations confirm Brady's prediction [7] of the reverse diffusiophoresis that the total osmotic force and hence the phoretic speed is linearly proportional to the swim speed gradient.

density is higher. Consequently the resulting phoretic motion is towards regions of higher bulk bath particle concentration even though the active bulk particles repel the phoretic particles — reverse diffusiophoresis! We also confirm that the magnitude of the total osmotic force is linearly proportional to the swim speed gradient. The phoretic speed then is also linearly proportional to the swim speed gradient from eq. (3.3).

We note that in an active bath a phoretic motion can be achieved even without a concentration gradient. For example, suppose that the reorientation time τ_R spatially varies while the swim speed U_0 and the translational diffusivity D_T are uniform throughout a suspension. Then the background number density of active bath particles is constant since U_0 does not change but the osmotic pressure at the no-flux contact surface $\Pi|_{S_c}$ is proportional to the run length $\ell = U_0\tau_R$ (see Fig. 3.1(b)) and therefore varies. Thus, a phoretic motion in this case is down the gradient of the reorientation time τ_R. More generally, a spherical phoretic particle in a bath of active hard-spheres moves down a run length gradient regardless of the

concentration gradient as pointed out by Brady [7].

Indeed active bath particles do not even require any spatial variations in transport properties to generate a directed motion of an immersed body. All that matters is a broken symmetry of the osmotic pressure at the contact surface, which can be also achieved by an asymmetric body shape of the immersed object (e.g. chevron, chiral gear, etc.) in active matter systems. From discussions in this section it is clear that the (classical) diffusiophoresis is just a special case of 'osmophoresis' [9], in which a concentration gradient is a source of the broken symmetry to generate nonzero total osmotic force on a phoretic body, from Brady's new perspective. Thus, the reverse diffusiophoresis in an active bath can be considered as an immediate consequence of the reverse osmotic effect in active matter systems.

3.5 Conclusions

In this Chapter we showed that a mechanical approach to the problems discussed in the preceding Chapter reveals more important consequences of spatial variation in transport properties in active matter systems. To describe the mechanics of the systems we investigated the pressure exerted by active particles and showed that the particle phase pressure at a no-flux wall is linearly proportional to the run length $U_0\tau_R$. Consequently, when swim speed varies spatially, the particle pressure at a wall is higher in the region with the smaller bulk number density $n \propto U_0^{-1}$ — the reverse osmotic effect. From a global mechanical force balance, a difference in the particle phase pressures on the walls should be balanced by the fluid pressure at the walls so that the whole suspension remains force-free. Thus, the fluid pressure at a wall is smaller in the region with the smaller bulk number density. The fluid pressure gradient between the walls can be utilized as a pump to generate a fluid flow from regions of high concentration to low — the reverse osmotic flow — by connecting the two confining walls with a tube and letting only the fluid to pass through the walls.

We note that the reverse osmotic behavior is unique to active systems and may be important in biological processes. The interior of a cell is a highly active system driven by ATP, motor proteins, enzymes [10], etc. Local variations in activity may result in solvent pressure gradients that could drive fluid motion, affect transport processes within a cell, and even transport a whole cell [6]. Variations in activity can also maintain concentration differences or gradients without the need for an external potential or a semipermeable membrane. This suggests some of our knowledge

in biological systems (e.g. how the cell maintains its osmotic balance with its surroundings) may need to be reexamined.

It is important to be mindful that our intuition and knowledge obtained from passive or equilibrium systems can lead to wrong conclusions when dealing with active systems that are naturally driven away from the equilibrium. We considered diffusiophoresis in an active bath as an example of counterintuitive phenomena in active systems. A phoretic body in an active bath can move from regions of low concentration to high even though the phoretic and bath particles undergo purely repulsive interactions, which directly contradicts well-known results for diffusiophoresis in a passive bath. A phoretic motion is fundamentally powered by the total osmotic force on an immersed object [7] and therefore the unique reverse osmotic behavior of an active suspension generates the reverse diffusiophoresis when the swim speed of active bath particles spatially varies. From BD simulations the reverse diffusiophoretic speed is shown to be linearly proportional to the gradient of run length of active bath particles as predicted by Brady [7].

In the following Chapter we discuss another example that is seemingly confounding from the equilibrium viewpoint: motility-induced phase separation. Instead of using equilibrium theories that are not guaranteed to be fruitful when describing active matter systems, we return to first principles — simple mechanics — and solve the problem that has intrigued and puzzled the active matter community since its beginning.

References

[1] W. Yan and J. F. Brady, "The force on a boundary in active matter," *J. Fluid Mech.*, vol. 785, R1.1–R1.11, Dec. 2015.

[2] A. K. Omar, Z.-G. Wang, and J. F. Brady, "Microscopic origins of the swim pressure and the anomalous surface tension of active matter," *Phys. Rev. E*, vol. 101, no. 1, p. 012 604, 2020.

[3] S. C. Takatori and J. F. Brady, "Towards a thermodynamics of active matter," *Phys. Rev. E - Stat. Nonlinear, Soft Matter Phys.*, vol. 91, no. 3, p. 32 117, 2015.

[4] W. Yan and J. F. Brady, "The swim force as a body force," *Soft Matter*, vol. 11, no. 31, pp. 6235–6244, Jul. 2015.

[5] M. Cheryan, *Ultrafiltration and Microfiltration Handbook*. CRC press, 1998.

[6] Z. Peng, T. Zhou, and J. F. Brady, "Activity-induced propulsion of a vesicle," *arXiv preprint arXiv:2112.05904*, 2021.

[7] J. F. Brady, "Phoretic motion in active matter," *Journal of Fluid Mechanics*, vol. 922, 2021.

[8] ——, "Particle motion driven by solute gradients with application to autonomous motion: Continuum and colloidal perspectives," *Journal of Fluid Mechanics*, vol. 667, pp. 216–259, 2011.

[9] U. M. Córdova-Figueroa and J. F. Brady, "Osmotic propulsion: The osmotic motor," *Physical review letters*, vol. 100, no. 15, p. 158 303, 2008.

[10] A.-Y. Jee, Y.-K. Cho, S. Granick, and T. Tlusty, "Catalytic enzymes are active matter," *Proceedings of the National Academy of Sciences*, vol. 115, no. 46, E10812–E10821, 2018.

Chapter 4

MECHANICAL THEORY OF PHASE COEXISTENCE

Liquid-gas phase separation is a well-understood topic in thermodynamics [1, 2]. From statistical thermodynamics, it can be shown that a liquid-gas phase separation requires attractive interactions as an essential ingredient [3], which is usually accepted as common knowledge. However, this is not true in active matter systems, which are inherently out of equilibrium due to the self-propelling motion of active constituents; purely repulsive active colloids can undergo a liquid-gas phase separation: the motility-induced phase separation (MIPS) [4–7]. While it seems confounding, the phenomenological description [5] is surprisingly simple: a positive feedback between the repulsive collisions that reduces the local swim speed [8, 9] and slow swim speed that increases the number density [10–13].

Due to the nonequilibrium nature, the classical and statistical thermodynamic framework cannot be directly applied to analyze MIPS, and there have been a number of attempts to generalize thermodynamic frameworks to active systems for the description of MIPS [14–25]. However, debate continues about the correct definition of the (nonequilibrium) chemical potential and free energy of active matter systems, which are core thermodynamic properties required for a description of phase behaviors. In this Chapter, we propose an alternative perspective to approach MIPS: instead of generalizing the thermodynamic framework, we develop a mechanical theory of phase coexistence that can be generally applicable to equilibrium and nonequilibrium systems. In the following sections, we first revisit the thermodynamic descriptions of phase equilibrium and introduce an equivalent mechanical description of phase equilibrium. Unlike the thermodynamic framework, which only applies to equilibrium systems, a mechanical theory can be readily applied to the nonequilibrium phase coexistence. Using the mechanical approach, we reveal phase coexistence conditions and interface structure of MIPS.

4.1 Phase Equilibrium Conditions

Thermodynamics provides a powerful framework to study systems at equilibrium. At the heart of thermodynamics is the thermodynamic extremum principles which is rooted in the second law of thermodynamics. The extremum principles state that the system possesses a minimum free energy at equilibrium. In some cases, the

minimum free energy state is achieved by having multiple phases in a system: phase equilibrium.

At phase equilibrium, the temperature T, pressure p, and chemical potential μ of each species are uniform in all phases — the thermal, mechanical, and chemical equilibria. To see this, let us consider an isolated C-component system with N_i particles of species i ($\in \{1, 2, \ldots, C\}$), volume V, and energy of the system E and suppose the system has two phases α and β at contact. We denote variables for each phase with superscripts e.g. V^α is the volume occupied by α phase. Since the interface of the two phases is diathermal, movable, and permeable to the chemical species, the energy, volume, and number of particles of each phase are unconstrained. Using the additivity of the entropy $S = S^\alpha + S^\beta$ and the fundamental thermodynamic relation, the variation in the system entropy to the first orders is given by

$$\delta S = \left(\frac{1}{T^\alpha} - \frac{1}{T^\beta}\right)\delta E^\alpha + \left(\frac{p^\alpha}{T^\alpha} - \frac{p^\beta}{T^\beta}\right)\delta V^\alpha - \sum_{i=1}^{C}\left(\frac{\mu_i^\alpha}{T^\alpha} - \frac{\mu_i^\beta}{T^\beta}\right)\delta N_i^\alpha \ . \tag{4.1}$$

From the second law of thermodynamics, the entropy of an isolated system reaches a maximum at equilibrium and thus the first differential of the system entropy S with respect to any macrostate variable X vanishes at an equilibrium state: $\delta S/\delta X = 0$. Consequently $\delta S = 0$ for any small variations in unconstrained variables at equilibrium and therefore from eq. (4.1)

$$T^\alpha = T^\beta, \quad p^\alpha = p^\beta, \quad \mu_i^\alpha = \mu_i^\beta \quad \forall i \in \{1, 2, \ldots, C\} \ . \tag{4.2}$$

When more than two phases are present, the phase equilibrium condition (4.4) is satisfied by every pair of phases by the zeroth law of thermodynamics. Hence, T, p, and μ are the same in all coexisting phases at equilibrium. We note that the Gibbs phase rule is an immediate consequence of a degree of freedom analysis on the phase equilibrium condition.

One can also find thermodynamic stability conditions by considering the second order variation of the entropy. For example, we consider variations in the energy:

$$\delta^2 S = \frac{1}{2}\left[\left(\frac{\partial}{\partial E^\alpha}\left(\frac{1}{T^\alpha}\right)\right)_{V^\alpha, N^\alpha} + \left(\frac{\partial}{\partial E^\beta}\left(\frac{1}{T^\beta}\right)\right)_{V^\beta, N^\beta}\right](\delta E^\alpha)^2 \ . \tag{4.3}$$

Now we let the two phases to be identical — the system is homogeneous — and treat the interface as an imaginary surface dividing the system into two regions α

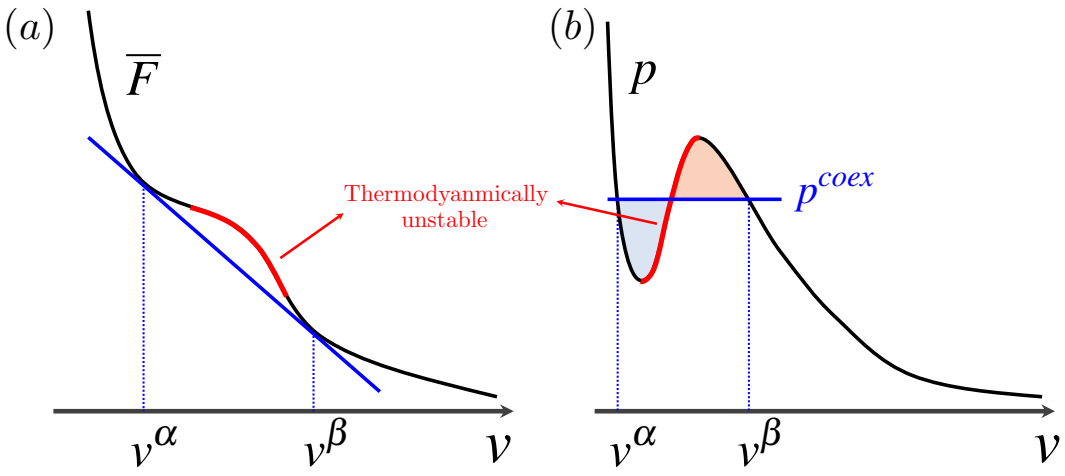

Figure 4.1: (a) A schematic description of the double-tangent construction on an isotherm in the diagram of the molar Helmholtz free energy $\overline{F}$ versus the molar volume v at a fixed temperature T. The points at contact with the common tangent line (blue) correspond to the coexisting phases. The slope and y-intercept of the common tangent represents the the coexistence pressure $(\partial\overline{F}/\partial v)_T = -p$ and the coexistence chemical potential $\overline{F} - v(\partial\overline{F}/\partial v)_T = \mu$. The red region of the curve indicates unstable region from the stability condition (4.5). (b) A schematic description of the Maxwell construction on an isotherm in the $p - v$ diagram. A horizontal line that cuts equal areas from the isotherm above (shaded blue) and below (shaded red) gives the coexistence pressure. The intersections of the horizontal line and isotherm correspond to the coexisting phases. The red region of the curve indicates unstable region from the stability condition (4.5).

and β. By the second law, the entropy of the system holds its maximum value at equilibrium. Thus, $\delta^2 S \leq 0$ and from eq. (4.3) we should have

$$c_V = \frac{1}{N}\left(\frac{\partial E}{\partial T}\right)_{V,N} \geq 0\,, \tag{4.4}$$

where c_V^α is the molar heat capacity at constant volume and $T = T_\alpha = T_\beta$ from the equilibrium condition (4.4). Using the thermodynamic extremum principles, similar variational analyses can be performed on systems with different conditions. One of the most useful stability conditions is obtained by the Helmholtz energy minimization principle for the system at fixed N, V, and T:

$$\kappa_T = -\frac{1}{V}\left(\frac{\partial V}{\partial p}\right)_{T,N} \geq 0\,, \tag{4.5}$$

where κ_T is the isothermal impressibility and $p = p_\alpha = p_\beta$ from the equilibrium condition (4.4).

A phase diagram can be constructed by directly finding states that satisfy the phase equilibrium condition. When a pressure-explicit equation of state that is valid for multiple phases (e.g. van der Waals equations state for liquid and gas) is known for a single component system, alternative graphical representations of the equilibrium condition provide more convenient and instructive methods to obtain a phase diagram: the double-tangent and Maxwell (equal-area) constructions.

In the double-tangent construction, the molar Helmholtz free energy $\overline{F}$ curve is drawn as a function of the molar volume v at a constant temperature T as shown in Fig. 4.1(a). A tangent line of the free energy curve has the slope $(\partial\overline{F}/\partial v)_T = -p$ and y-intercept $\overline{F} - v(\partial\overline{F}/\partial v)_T = \mu$. Therefore if multiple points, say $(v^\alpha, \overline{F}(v^\alpha, T))$ and $(v^\beta, \overline{F}(v^\beta, T))$, on the curve share a common tangent, the corresponding states (v^α, T) and (v^β, T) satisfy the phase equilibrium condition and are called the binodal.

When the overall molar volume of the system $v \in (v^\alpha, v^\beta)$, the total Helmholtz free energy is minimized by having the two separated phases with (v^α, T) and (v^β, T): the Helmholtz free energy minimization principle for fixed N, V, and T. The phase separation always occurs when the free energy curve is convex upward, i.e. $(\partial^2\overline{F}/\partial v^2)_T = -(\partial p/\partial v)_T < 0$ — the red segment in Fig. 4.1(a) — to meet the mechanical stability condition (4.5). The points at the onset the instability, i.e. $(\partial^2\overline{F}/\partial v^2)_T = 0$ are called the spinodal. The states between the binodal and spinodal is called metastable. In the metastable region, the system is allowed to exist as a homogeneous state without a phase separation since the stability condition (4.5) is satisfied. However, a phase separation would occur whenever possible in order to minimize the total Helmholtz free energy of the system.

The Maxwell construction is obtained by considering the first derivatives with respect to the molar volume v in the double-tangent construction. We now consider the pressure $p = -(\partial\overline{F}/\partial v)_T$ instead of $\overline{F}$ and draw a $p-v$ isotherm as shown in Fig. 4.1(b). Then one seeks the coexistence pressure $p = p^{coex}(T)$ such that

$$p(v^\alpha, T) = p(v^\beta, T) = p^{coex}(T)\ , \quad \int_{v^\alpha}^{v^\beta} \left[p(v, T) - p^{coex}(T)\right]\ dv = 0\ , \tag{4.6}$$

then the intersections of the horizontal line and the isotherm gives the coexisting states. The first condition in (4.6) is trivially required to have the same pressure in the two states (v^α, T) and (v^β, T). The integral in (4.6) is required for the same chemical potential in the coexsiting phases. To see this, we integrate by parts to

obtain

$$[v(p - p^{coex})]_{v^\alpha}^{v^\beta} - \int_{v^\alpha}^{v^\beta} v \left(\frac{\partial p}{\partial v}\right)_T dv = 0 \,. \tag{4.7}$$

Due to the first condition in (4.6), the bracketed term in (4.7) vanishes. The integral in (4.7) represents the difference in the chemical potentials at v^α and v^β since $d\mu = vdp = v(\partial p/\partial v)_T \, dv$ at constant temperature. Thus, the second integral condition enforces chemical potentials of the two coexisting states to be identical.

From the Maxwell construction, it is clearly seen that the coexistence pressure p^{coex} depends on the temperature since the isotherms depends on the temperature of the system. The relationship between p^{coex} and T — the Clausius equation — can be directly derived from the equilibrium condition (4.1). Suppose that a single-component system at the temperature T has two phases α and β at equilibrium: $T = T_\alpha = T_\beta$, $p^{coex}(T) = p^\alpha = p^\beta$, and $\mu^\alpha(T, p^{coex}(T)) = \mu^\beta(T, p^{coex}(T))$. Then we imagine that the temperature varies slightly by δT and a new phase equilibrium is achieved. At the new temperature $T+\delta T$, the equilibrium condition (4.1) is satisfied again: $T+\delta T = T_\alpha = T_\beta$, $p^{coex}(T+\delta T) = p^\alpha = p^\beta$, and $\mu^\alpha(T+\delta T, p^{coex}(T+\delta T)) = \mu^\beta(T+\delta T, p^{coex}(T+\delta T))$. Taylor expanding the new chemical equilibrium condition about the original temperature, we obtain

$$\delta T \left[-\Delta s + \frac{dp}{dT}^{coex} \Delta v \right] + O(\delta T^2) = 0 \,, \tag{4.8}$$

where s is the molar entropy and Δ represents the difference between the two phases e.g. $\Delta v = v^\alpha - v^\beta$. Now by taking a limit $\delta T \to 0$ the temperature dependence of the coexistence pressure is obtained as

$$\frac{dp}{dT}^{coex} = \frac{\Delta s}{\Delta v} \,. \tag{4.9}$$

The entropy change due to the phase transition at constant temperature and pressure can be written as $\Delta s = \Delta h^L/T$, where Δh^L is the molar latent heat involved in transition from phase β to α. Replacing the Δs in eq. (4.9), we obtain the Clausius equation:

$$\frac{dp}{dT}^{coex} = \frac{\Delta h^L}{T\Delta v} \,. \tag{4.10}$$

4.2 Microscopic Structure of Phase Interfaces

In the classical thermodynamic picture, spotlight is on macroscopic properties and the phase interface is treated as a surface where a sharp discontinuity occurs in bulk properties [26]. The discontinuity at the interface is justified by the negligibly small

range of interactions between the constituting particles compared to the macroscopic length scale of bulk phases. To study the microscopic structure of phase interfaces, statistical thermodynamic approaches should be taken. The first of such attempts was made by van der Walls [27], who founded the so-called gradient theory to obtain continuous density profiles at the liquid-gas interface. Static equilibrium properties of inhomogeneous systems now can be more effectively investigated in the framework of the classical density functional theory (cDFT) (see appendix 4.6 for a brief discussion on the structure of the cDFT framework). In this section, we reformulate the gradient theory [27] in the language of the cDFT to seek ingredients required to describe microscopic structure of interfaces.

Let consider an isothermal system of volume V with the external potential ϕ^{ext} in a chemical reservoir with the chemical potential μ. The equilibrium condition for the system is given by the minimization of the grand potential $W = \int_V f[\rho] + (\phi^{ext} - \mu)\rho \; d\boldsymbol{x}$:

$$\frac{\delta}{\delta\rho(\boldsymbol{x})} \int_V f[\rho(\boldsymbol{x}')] \; d\boldsymbol{x}' + \phi^{ext}(\boldsymbol{x}) - \mu = 0 \,, \tag{4.11}$$

where $f[\rho]$ is the intrinsic Helmholtz free energy density. Here, brackets are used to denote the functional dependence. Equation (4.11) is the main equation of the cDFT. While eq. (4.11) is exact (see appendix 4.6), it is usually difficult to find an exact functional expression for the free energy density functional. Consequently, it is customary to use an approximate form of $f[\rho]$ and the approximation determines the level and accuracy of description.

We first assume that the intrinsic Helmholtz free energy density f at a position $\boldsymbol{x}$ depends on the local density $\rho(\boldsymbol{x})$ only and examine the consequences: the local density approximation, i.e. $f[\rho] = f_0(\rho)$, where f_0 is the Helmholtz free energy density of a homogeneous system. The fundamental thermodynamic relation for the Helmholtz free energy density is given by

$$df_0 = \mu_0 d\rho - \rho s_0 dT \,, \tag{4.12}$$

where μ_0 and s_0 are the (intrinsic) chemical potential and molar entropy in a homogeneous system. Since $f = f_0(\rho)$ is simply a function — not a functional — of the density, the functional derivative in eq. (4.11) is replaced by a partial derivative $\partial f_0/\partial\rho$ and eq. (4.11) becomes

$$\mu_0(\rho(\boldsymbol{x})) = \mu - \phi^{ext}(\boldsymbol{x}) \,. \tag{4.13}$$

Equation (4.13) indicates that at equilibrium the sum of the intrinsic chemical potential and the external potential is constant throughout the system with the value

set by the chemical reservoir. In other words, the gradient of the intrinsic chemical potential acts as a thermodynamic driving force which is balanced by the external force: $\nabla\mu_0 = -\nabla\phi^{ext}$. Using $\nabla\mu_0 = (\partial\mu_0/\partial\rho)_T\nabla\rho = (\partial p_0/\partial\rho)_T\nabla\ln\rho$ we obtain the (macroscopic) mechanical equilibrium condition:

$$-\rho(\boldsymbol{x})\nabla\phi^{ext}(\boldsymbol{x}) - \nabla p_0(\rho(\boldsymbol{x}))\ , \tag{4.14}$$

where $p_0 = \rho\mu_0 - f_0$ is the (intrinsic) pressure in the homogeneous state.

When there is no external potential, eq. (4.13) gives $\mu_0(\rho(\boldsymbol{x})) = \mu$ (const.) and eq. (4.14) gives $p_0(\rho(\boldsymbol{x}))$ = constant. Thus, the simple model of free energy density functional $f = f_0(\rho)$ just retrieves the macroscopic equilibrium condition (4.1) of the classical thermodynamics — the microscopic structure of interfaces cannot be described. This is because the free energy functional with the local density approximation does not sufficiently include effects of particle interactions that are equally absent in the classical thermodynamic perspective. We also note that in this macroscopic description, we required thermodynamic knowledge $(\partial\mu_0/\partial\rho)_T = (\partial p_0/\partial\rho)_T$ in order to obtain the mechanical equilibrium condition (4.14). If one does not know such a thermodynamic relation between the chemical potential and pressure, the chemical equilibrium condition. (4.13) alone cannot uniquely determine a phase equilibrium state.

When there exists a gradient in density, the state at a given position is not completely determined by the local density at the same position. It depends on the density in the vicinity as well due to the interactions between the particles. In other words, to describe the interfaces where the density spatially varies, the free energy density f should be modeled as a functional of the density that depends not only on the local value of the density but also on the shape or gradient of the density profile.

Now we treat the free energy density f as a functional of the density. When spatial variations in density are slow (e.g. phase interface near the critical point), the free energy density functional can be expanded in gradients of density [28]:

$$f = f_0(\rho) + \boldsymbol{f}_{21}(\rho) : \nabla\nabla\rho + \boldsymbol{f}_{22}(\rho) : \nabla\rho\nabla\rho + O(\nabla^4\rho)\ , \tag{4.15}$$

where $\boldsymbol{f}_{21}$ and $\boldsymbol{f}_{22}$ are second-order-tensorial material properties of a homogeneous system with the density ρ. In the density gradient expansion all the odd-order gradient terms vanish due to the reflection symmetry. When interactions between the constituting particles are isotropic, so should the material properties: $\boldsymbol{f}_{21} = f_{21}\boldsymbol{I}$

and $\boldsymbol{f}_{22} = f_{22}\boldsymbol{I}$. Now eq. (4.15) becomes

$$f = f_0(\rho) + f_{21}\nabla^2\rho + f_{22}(\nabla\rho)^2 \ . \tag{4.16}$$

Using the divergence theorem, the intrinsic Helmholtz free energy can be written as

$$\mathcal{F} = \int_V f \ d\boldsymbol{x} = \int_V \left[f_0 + \frac{1}{2} f_2(\rho)(\nabla\rho)^2 \right] \ d\boldsymbol{x} \ , \tag{4.17}$$

where $f_2 = 2(f_{22} - \partial f_{21}/\partial\rho)$. The last term in the second integral is called the *square-gradient* term. The square-gradient term represents free energetic penalty due to variations in density and gives rise to the interfacial tension as we will see later. From eq. (4.17) the chemical equilibrium condition (4.11) now becomes

$$\mu_0(\rho(\boldsymbol{x})) - \frac{1}{2}\frac{\partial f_2}{\partial\rho}(\nabla\rho)^2 - f_2\nabla^2\rho + \phi^{ext} - \mu = 0 \ , \tag{4.18}$$

which is a partial differential equation that gives a microscopic density profile of interfaces as a solution. Unlike the previous case of the local density approximation, which required thermodynamic information to determine a unique equilibrium state, the density profile from eq. (4.18) alone describes the structure of the interface and the coexisting densities as well. In order to solve eq. (4.18) f_2 is required. Here, we simply note that f_2 can be computed with the direct correlation functions as shown by Yang, Fleming, and Gibbs [29] and proceed without specifying f_2 in order to focus on the general structure of the chemical equilibrium condition.

Equation (4.18) is consistent with the macroscopic chemical equilibrium condition. This can be shown even without solving the equation. Suppose that two phases α and β coexist at equilibrium in the absence of the external potential. Deep inside the phases, it is spatially uniform and all the gradient terms vanish. Thus, eq. (4.18) recovers the classical chemical equilibrium condition $\mu_0(\rho^\alpha) = \mu_0(\rho^\beta) = \mu$ (const.) for the bulk phases.

For a mechanical equilibrium condition we first multiply eq. (4.18) with $\nabla\rho$ and obtain

$$(\mu_0 - \mu)\nabla\rho - \frac{1}{2}\nabla f_2(\nabla\rho)^2 - f_2\nabla\rho\nabla^2\rho + \phi^{ext}\nabla\rho = \boldsymbol{0} \ . \tag{4.19}$$

The square-gradient term in eq. (4.19) can be expressed in two ways:

$$\nabla f_2(\nabla\rho)^2 = \nabla\left[f_2(\nabla\rho)^2\right] - 2f_2\nabla\rho\cdot\nabla\nabla\rho \tag{4.20}$$

$$= \nabla\cdot[f_2\nabla\rho\nabla\rho] - f_2\nabla^2\rho\nabla\rho - f_2\nabla\rho\cdot\nabla\nabla\rho \ . \tag{4.21}$$

Consequently, it can be expressed as a linear combination of the two expressions (4.20) and (4.21):

$$\begin{aligned}\nabla f_2(\nabla\rho)^2 =& c\left[\nabla\left[f_2(\nabla\rho)^2\right] - 2f_2\nabla\rho\cdot\nabla\nabla\rho\right] \\ &+ (1-c)\left[\nabla\cdot[f_2\nabla\rho\nabla\rho] - f_2\nabla^2\rho\nabla\rho - f_2\nabla\rho\cdot\nabla\nabla\rho\right] , \end{aligned} \tag{4.22}$$

where c is an arbitrary number. From eq. (4.22) with $c = 2$, eq. (4.19) becomes,

$$(\mu_0 - \mu)\nabla\rho - \nabla\cdot[f_2\nabla\rho\nabla\rho] + \frac{1}{2}\nabla\left[f_2(\nabla\rho)^2\right] + \phi^{ext}\nabla\rho = \mathbf{0} . \tag{4.23}$$

For simplicity we consider a planar interface between the two phases α ($z < 0$) and β ($z > 0$) and let the z axis parallel with the normal to the interface. When there is no external potential, integration of eq. (4.23) from deep inside the phase α ($z \to -\infty$) to an arbitrary position z gives

$$f_0(\rho) - \mu\rho + p_0(\rho^\alpha) - \frac{1}{2}f_2\left(\frac{d\rho}{dz}\right)^2 = 0 . \tag{4.24}$$

Taking the limit $z \to \infty$ (the bulk phase β), the square-gradient term in (4.24) vanishes due to the homogeneity in the bulk phase and we retrieve the macroscopic mechanical equilibrium condition $p_0(\rho^\alpha) = p_0(\rho^\beta) \equiv p^{coex}$.

The interfacial tension is defined as the excess grand free energy due to the interface per unit area. Noting that the grand potential density of a homogeneous system is given by $w_0 = f_0 - \mu_0\rho = -p_0$ and the two bulk phases have the same bulk pressure p^{coex}, the interfacial tension is

$$\begin{aligned}\gamma &= \int_{-\infty}^{\infty} (f[\rho] - \mu\rho) - (-p^{coex})\, dz \\ &= \int_{-\infty}^{\infty} f_0(\rho) + \frac{1}{2}f_2\left(\frac{d\rho}{dz}\right)^2 - \mu\rho + p^{coex}\, dz \\ &= \int_{-\infty}^{\infty} f_2\left(\frac{d\rho}{dz}\right)^2 dz , \end{aligned} \tag{4.25}$$

where the last equation obtained by eq. (4.24). Equation (4.25) clearly shows that the interfacial tension is the result of the square-gradient term which penalizes nonhomogeneity in the density due to interparticle interactions.

4.3 Mechanical Description of Phase Interfaces

While the cDFT framework is useful to describe phase equilibrium and interfaces, it is not applicable to nonequilibrium cases. This is because the cDFT is written

in the language of (statistical) thermodynamics. The chemical equilibrium condition (4.11) is rooted in the free energy minimization at equilibrium, which is not guaranteed to be achieved in nonequilibrium systems even at steady state. Furthermore the description of chemical equilibrium naturally involves the chemical potential which may not be well-defined for systems away from equilibrium. Clearly, a theory of phase coexistence that works for both in and out of equilibrium requires a more general perspective that does not rely upon thermodynamic concepts. In this section we translate the thermodynamic chemical equilibrium condition (4.23) obtained in the preceding section into the language of mechanics. We show that the mechanical description of phase equilibrium offers a new perspective on the phase coexistence which can be applied to systems both in and out of equilibrium.

The thermal, mechanical, and chemical equilibria required for the phase equilibrium represent that there are no net fluxes of heat, momentum, nor mass in the system. To describe the phase equilibrium or coexistence, the most important condition is the one for the mass transport; for phases to remain in a state of coexistence, there should be no net mass transfer whether the system is in or out of equilibrium. Thus, to develop a general theory of phase coexistence, the main task is in obtaining a condition of no net mass transport in a thermodynamics-free form.

To obtain a thermodynamics-free mass transport condition we remove thermodynamic quantities from the chemical equilibrium condition (4.23). Using eq. (4.18) we can eliminate chemical potentials in eq. (4.23) to obtain

$$-\rho\nabla\phi^{ext} + \nabla\cdot\left[-p_0\boldsymbol{I} + \left(\frac{1}{2}\frac{\partial(f_2\rho)}{\partial\rho}(\nabla\rho)^2 + f_2\rho\nabla^2\rho\right)\boldsymbol{I} - f_2\nabla\rho\nabla\rho\right] = \boldsymbol{0}\,. \quad (4.26)$$

Equation (4.26) is a mechanical force balance on the fluid; the bracketed term is the stress of the fluid and its divergence is balanced by the external force. The stress deviates from $-p_0\boldsymbol{I}$ — the stress when the fluid is homogeneous — due to the inhomogeneity in the density. The excess stress is known as the Korteweg stress [30]. The Korteweg stress acts as a stabilizer that allows the interfacial region to possess densities in the spinodal region [31]. Also, its nonisotropic part $-f_2\nabla\rho\nabla\rho$ represents the effective stress from the interfacial tension (4.25). Integration of eq. (4.26) over the interfacial region recovers the Young-Laplace equation. We note that f_2 was introduced by the density-gradient expansion of the free energy functional (eqs. (4.15) and (4.16)) in the statistical thermodynamic context but it is not a thermodynamic quantity but rather a material property related to the microscopic structure at a homogeneous density [29, 32].

The equivalence of the thermodynamic chemical equilibrium condition (4.23) and mechanical force balance (4.26) is not obtained by serendipity. Thermodynamics is a phenomenological theory — an individual particle does not know thermodynamics. Each particle only follows Newton's laws of motion in response to the forces acting on it, which is essentially how the molecular dynamics simulations are performed. Therefore, one can directly *average* or coarse-grain the mechanical equations of motion to describe the transport processes with continuum-balance laws [33] including microscopic details and study phase behaviors without using any knowledge of thermodynamics. Thermodynamics is simply a systematic language that is optimized for a description of the statistical rules followed by *average* equilibrium properties of a macroscopic system. In this sense, the mechanical force balance (4.26) is more fundamental than eq. (4.23). Furthermore, the mechanical perspective can be applied to nonequilibrium systems as well.

Indeed eq. (4.23) for a simple fluid in an isothermal system can be derived without using any thermodynamic concepts. By coarse-graining the microscopic dynamics [33], a particle balance equation to describe the mass transport is obtained:

$$\frac{\partial \rho}{\partial t} + \nabla \cdot \boldsymbol{j} = 0 \,, \tag{4.27}$$

where $\boldsymbol{j} = \rho \boldsymbol{v}$ is the particle flux and $\boldsymbol{v}$ is the mass- or number-averaged velocity. The required velocity field $\boldsymbol{v}$ can be obtained by a continuum mechanical momentum balance, which also can be obtained from the the microscopic dynamics:

$$\frac{\partial (\rho \boldsymbol{v})}{\partial t} + \nabla \cdot (\rho \boldsymbol{v}\boldsymbol{v}) = -\rho \nabla \phi^{ext} + \nabla \cdot \boldsymbol{\sigma} \,, \tag{4.28}$$

where $\boldsymbol{\sigma}$ is the stress of the fluid. Since $\partial / \partial t = 0$ and $\boldsymbol{j} = \boldsymbol{0}$ at equilibrium and it is required that $-\rho \nabla \phi^{ext} + \nabla \cdot \boldsymbol{\sigma} = \boldsymbol{0}$. In order to obtain the same level of description with the square-gradient free energy (4.17), we perform a density-gradient expansion for the stress [31, 34] to the second order and obtain

$$-\rho \nabla \phi^{ext} + \nabla \cdot \left[-p_0 \boldsymbol{I} + \left(p_{21} \nabla^2 \rho + p_{22} (\nabla \rho)^2 \right) \boldsymbol{I} + p_{23} \nabla \nabla \rho + p_{24} \nabla \rho \nabla \rho \right] = \boldsymbol{0} \,, \tag{4.29}$$

which has the same form with eq. (4.26). Here, $p_{21,22,23,24}$ are material properties of the fluid at a homogeneous state and depend on the local density, and when the particle interactions are spherically symmetric, and $p_{23} = 2p_{21}$ and $p_{24} = 2p_{22}$ for the isotropicity.

Now let us again consider the planar interface between two phases α and β with the mechanical perspective. By integrating the mechanical force balance (4.29), we

obtain

$$-p_0(\rho) + a(\rho)\frac{d^2\rho}{dz^2} + b(\rho)\left(\frac{d\rho}{dz}\right)^2 = \text{const.}\,, \tag{4.30}$$

where $a = p_{21} + p_{23}$ and $b = p_{22} + p_{24}$. From eq. (4.30) the pressure is the same deep inside the coexisting phases due to the lack of density gradients in the bulk: the mechanical equilibrium condition. Thus, the integration constant on the right-hand side is the negative coexistence pressure $-p^{coex}$.

The interfacial tension can be also computed from a mechanical perspective [31, 35, 36]:

$$\gamma = \int_{-\infty}^{\infty}\left[\frac{1}{2}\left(\sigma_{xx} + \sigma_{yy}\right) - \sigma_{zz}\right]\,dz\,. \tag{4.31}$$

The normal and tangential components of the stress for the planar phase interface are

$$\sigma_{zz} = -p_0 + a\frac{d^2\rho}{dz^2} + b\left(\frac{d\rho}{dz}\right)^2\,, \tag{4.32}$$

$$\sigma_{xx} = \sigma_{yy} = -p_0 + p_{21}\frac{d^2\rho}{dz^2} + p_{22}\left(\frac{d\rho}{dz}\right)^2\,. \tag{4.33}$$

From the mechanical definition (4.31) the surface tension becomes

$$\gamma = \int_{-\infty}^{\infty}\left[p_{23}\frac{d^2\rho}{dz^2} + p_{24}\left(\frac{d\rho}{dz}\right)^2\right]\,dz = \int_{-\infty}^{\infty}\left[\left(\frac{\partial p_{23}}{\partial\rho}\right)_T - p_{24}\right]\left(\frac{d\rho}{dz}\right)^2\,dz, \tag{4.34}$$

where the second equation is obtained by the divergence theorem.

Aifantis and Serrin [31] have shown that in an appropriate model of the stress the material properties a and b (and therefore p_{23} and p_{24} when particle interactions are isotropic) of a simple fluid are not independent. This is essentially because the mechanical force balance obtained from thermodynamic framework (4.26) has one parameter f_2 while the equivalent description (4.29) from the mechanical perspective has two. They find an integrating factor

$$E(\rho) = \frac{1}{a}\exp\left(2\int\frac{b}{a}\,d\rho\right)\,, \tag{4.35}$$

which allows the second order gradient terms in eq. (4.30) to vanish upon integration from one phase to the other:

$$\int_{\rho^\alpha}^{\rho^\beta}(p_0(\rho) - p^{coex})E(\rho)\,d\rho = 0\,, \tag{4.36}$$

which is an integral condition for no net mass transport between the bulk phases. By comparing eq.(4.36) and the Maxwell construction (4.7), the integrating factor $E(\rho) = a/\rho^2$ up to a nonzero multiplicative constant, which results $b = \rho d(a/\rho)/d\rho$.

As a final note, we emphasize that effects of *at least* the second order density gradients need to be considered to properly describe microscopic details of even-order tensorial quantities (e.g. free energy, pressure, stress, etc.). Odd-order density gradients do not affect the even-order tensors due to the reflection symmetry. For example, even if first order gradient terms are present, they do not impart information about microscopic details to even-order tensorial quantities. Thus, for both thermodynamic and mechanical descriptions of phase interfaces, of which the central physical quantities are free energy and stress, the mass transport condition should include effects of at least the second order gradients in density. Otherwise, we simply obtain macroscopic description of the system as seen in the local density approximation from the preceding section.

4.4 Motility-Induced Phase Separation

In this section, we apply the mechanical perspective on phases coexistence developed in the preceding section to a nonequilibrium case with the motility-induced phase separation (MIPS) of active Brownian particles (ABPs) as an example. From the mechanical perspective we obtain the conditions required by MIPS which is analogous to the phase equilibrium conditions (4.1). With the phase coexistence conditions we construct a phase diagram for MIPS which agrees with the Brownian Dynamics (BD) simulations. Further, by investigating the microscopic structure of the interfaces in MIPS we discover a unique nonequilibrium interfacial behavior.

To apply the mechanical perspective to MIPS, we obtain continuum-balance equations starting from the mechanical (Newton's) equations of motion for ABPs. The microscopic dynamics of ABPs is described by the overdamped Langevin equations:

$$\mathbf{0} = -\zeta \boldsymbol{U}_\alpha + \boldsymbol{F}_\alpha^{swim} + \boldsymbol{F}_\alpha^{c} + \boldsymbol{F}_\alpha^{B} \,, \tag{4.37}$$

$$\mathbf{0} = -\zeta_R \boldsymbol{\Omega}_\alpha + \boldsymbol{L}_\alpha^{B} \,, \tag{4.38}$$

$$\frac{\partial \boldsymbol{q}_\alpha}{\partial t} = \boldsymbol{\Omega}_\alpha \times \boldsymbol{q}_\alpha \,, \tag{4.39}$$

where $\boldsymbol{U}_\alpha$ and $\boldsymbol{\Omega}_\alpha$ are the translational and angular velocities of particle α. We denote the index of a particle with Greek subscripts. The resistive medium in which particles move (e.g. a suspending fluid) exerts translational and rotational

drag forces and torques: $-\zeta \boldsymbol{U}_\alpha$ and $-\zeta_R \boldsymbol{\Omega}_\alpha$, where ζ and ζ_R are translation and rotational drag coefficients. The self-propulsive swim force is $\boldsymbol{F}_\alpha^{swim} = \zeta U_0 \boldsymbol{q}_\alpha$, where U_0 is the free-space swim velocity and $\boldsymbol{q}_\alpha$ is the direction of swimming. The interparticle collisional force on particle α is $\boldsymbol{F}_\alpha^c$. Our theory applies to any types of interaction potentials but the results presented in this section are obtained with the Weeks-Chandler-Andersen (WCA) potential to highlight a unique property of MIPS — a liquid-gas phase separation with purely repulsive interactions. The random Brownian force and reorientation torque are $\boldsymbol{F}_\alpha^B$ and $\boldsymbol{L}_\alpha^B$ and follow the white noise statistics:

$$\overline{\boldsymbol{F}_\alpha^B(t)} = \boldsymbol{0} \,, \quad \overline{\boldsymbol{F}_\alpha^B(t)\boldsymbol{F}_\beta^B(t')} = 2\zeta^2 D_T \boldsymbol{I} \delta_{\alpha\beta} \delta(t-t') \,, \tag{4.40}$$

$$\overline{\boldsymbol{L}_\alpha^B(t)} = \boldsymbol{0} \,, \quad \overline{\boldsymbol{L}_\alpha^B(t)\boldsymbol{L}_\beta^B(t')} = 2\zeta_R^2/\tau_R \boldsymbol{I} \delta_{\alpha\beta} \delta(t-t') \,, \tag{4.41}$$

where D_T is the translational diffusivity, $\delta_{\alpha\beta}$ is the Kronecker delta, and τ_R is the time scale of random reorientations.

A dimensional analysis shows that there are four governing dimensionless parameters in the problem: ϕ, $U_0\tau_R/D$, $U_0^2\tau_R/D_T$, and $\epsilon/(D\zeta U_0)$, where ϕ is the volume (or area in 2D) fraction and D and ϵ are the length and energy parameter of the interaction potential. Here we consider the hard-sphere limit in which the repulsive interactive force is much larger than the Brownian and swim forces: $\epsilon/(D\zeta U_0) \gg 1$ and $\epsilon/(\zeta D_T) \gg 1$. Consequently, the problem is essentially governed by three dimensionless parameters: ϕ, $U_0\tau_R/D$, and $U_0^2\tau_R/D_T$.

Now we coarse-grain the microscopic dynamics of ABPs using the standard Irving-Kirkwood-Noll procedure [33, 37, 38] (see appendix 4.7 for the derivations of equations in the current section) and obtain a particle balance equation to describe the mass transport in the active suspension:

$$\frac{\partial n}{\partial t} + \nabla \cdot \boldsymbol{j}_n = 0 \,, \tag{4.42}$$

$$\boldsymbol{j}_n = U_0 \boldsymbol{m} + \frac{1}{\zeta}\left(\boldsymbol{F}^{ext} n + \nabla \cdot \boldsymbol{\sigma}^c\right) - D_T \nabla n \,, \tag{4.43}$$

where $n = \langle \sum_\alpha \delta(\boldsymbol{x} - \boldsymbol{x}_\alpha) \rangle$ is the average number density field, $\boldsymbol{j}_n$ is the particle flux, and $\boldsymbol{\sigma}^c$ is the collisional stress of the ABPs. The swimming motion of ABPs brings about a unique advective transport of particles $U_0\boldsymbol{m}$, where $\boldsymbol{m} = \langle \sum_\alpha \delta(\boldsymbol{x} - \boldsymbol{x}_\alpha)\boldsymbol{q}_\alpha \rangle$ is the polar order or net-orientation vector field. We note that the particle balance (4.42)-(4.43) is exact.

Equation (4.43) is indeed a mechanical force balance on the ABPs. By multiplying the drag coefficient ζ to eq. (4.43) and using the Stokes-Einstein-Sutherland relation $\zeta D_T = k_B T$, we obtain

$$\mathbf{0} = -\zeta \boldsymbol{j}_n + \zeta U_0 \boldsymbol{m} + \boldsymbol{F}^{ext} n + \nabla \cdot (\boldsymbol{\sigma}^c + \boldsymbol{\sigma}^{osmo}) \,, \tag{4.44}$$

where $\boldsymbol{\sigma}^{osmo} = -nk_BT\boldsymbol{I}$ is the osmotic stress. The suspending medium exerts the drag force $-\zeta \boldsymbol{j}_n$ on particles for their relative motion to the medium. The average of the individual swim forces acts as a self-generated 'body' force, $\zeta U_0 \boldsymbol{m}$, on the particle phase [39] and the divergence of particle stresses balances the forces.

In order to understand how the self-generated body force develops, we obtain an evolution equation for the polar order from the microscopic dynamics:

$$\frac{\partial \boldsymbol{m}}{\partial t} + \nabla \cdot \boldsymbol{j}_m + \frac{d-1}{\tau_R} \boldsymbol{m} = \mathbf{0} \,, \tag{4.45}$$

$$\boldsymbol{j}_m = U_0 \overline{U} \left(\boldsymbol{Q} + \frac{1}{d} n \boldsymbol{I} \right) + \frac{1}{\zeta} \boldsymbol{F}^{ext} \boldsymbol{m} + \frac{1}{\zeta} \nabla \cdot \left(\frac{\boldsymbol{\sigma}\, \boldsymbol{m}}{n} \right) - D_T \nabla \boldsymbol{m} \,, \tag{4.46}$$

where $\overline{U}(n)$ is the reduction in the swim velocity from its free- space value U_0 due to collisions with other particles, d is the spatial dimension for reorientation, and $\boldsymbol{Q} = \langle \sum_\alpha \delta(\boldsymbol{x} - \boldsymbol{x}_\alpha)(\boldsymbol{q}_\alpha \boldsymbol{q}_\alpha - \boldsymbol{I}/d) \rangle$ is the nematic order tensor field. The nematic order satisfies an equation analogous to the polar order equation:

$$\frac{\partial \boldsymbol{Q}}{\partial t} + \nabla \cdot \boldsymbol{j}_Q + \frac{2d}{\tau_R} \boldsymbol{Q} = \mathbf{0} \,, \tag{4.47}$$

$$\boldsymbol{j}_Q = U_0 \overline{U} \boldsymbol{B} + U_0 \boldsymbol{m} \cdot \left(\frac{\overline{U}}{d+2} \boldsymbol{\alpha} - \frac{1}{d} \boldsymbol{I}\boldsymbol{I} \right) + \frac{1}{\zeta} \boldsymbol{F}^{ext} \boldsymbol{Q} - \frac{1}{d\zeta} \nabla \cdot \boldsymbol{\sigma}^c \boldsymbol{I} - D_T \nabla \boldsymbol{Q} \,, \tag{4.48}$$

where $\boldsymbol{B} = \langle \sum_\alpha \delta(\boldsymbol{x} - \boldsymbol{x}_\alpha)(\boldsymbol{q}_\alpha \boldsymbol{q}_\alpha \boldsymbol{q}_\alpha - \boldsymbol{\alpha} \cdot \boldsymbol{q}_\alpha/(d+2) \rangle$ is the traceless third order orientational moment tensor field and $\boldsymbol{\alpha}$ is the fourth order isotropic tensor.

The equations for the polar order (4.45)-(4.46) and nematic order (4.47)-(4.48) show the well-known hierarchical structure of orientational moments due to the coupling between the moments of neighboring orders [39, 40]. Due to the sink terms in the equations, a higher order moment has an order of the gradient of a lower order moment (e.g. $\boldsymbol{m} \sim \nabla n$, $\boldsymbol{Q} \sim \nabla \boldsymbol{m} \sim \nabla\nabla n$, etc.) for high activities ($\ell_0^2/(D_T \tau_R) \gg 1$) that are required to achieve MIPS. Thus, for active suspensions the hierarchy of orientational moments naturally introduces microscopic nonlocal effects via orientational moments even without a density-gradient expansion. As discussed at the end of the preceding section, a mechanical description of interfaces

requires effects of at least the second order density gradients. We close the hierarchy by keeping all terms up to the order $O(k^2)$ in Fourier space assuming reasonably slow variations in the number density and investigate results of the minimal closed set of equations.[1]

It is notable that at steady state the polar order equation (4.45) allows the self-generated 'body' force to be written in a form of divergence: $\zeta U_0 \boldsymbol{m} = \nabla \cdot \boldsymbol{\sigma}^{swim}$, where $\boldsymbol{\sigma}^{swim} \equiv \zeta \ell_0 \boldsymbol{j}_m/(d-1)$ is the swim stress [41] and $\ell_0 = U_0 \tau_R$ is the run length in a free space. The swim stress is an effective stress arising from the self-propulsive forces. While the swim stress is not a true stress [36, 42] but a 'body' force recast as a form of a stress — analogous to the equivalent (or dynamic) pressure in fluid mechanics [17] or Maxwell stress in electrostatics [43] —[2] it is useful to determine the force exerted by ABPs on no-flux boundaries at steady state [39]. We show below that this steady-state property of active matter systems is indeed important in determining the phase coexistence criteria of MIPS.

Now let us consider a planar MIPS interface with the normal in z direction at steady state when there is no net mass transport $j_{n,z} = 0$. We label the coexisting phases α ($z \to -\infty$) and β ($z \to +\infty$). Here, we focus on the effects of the self-propelling motion of ABPs to discover the underlying physics of MIPS by considering athermal limit ($D_T = 0$), but it is straightforward to include the thermal Brownian motion. Now, the problem is described by two dimensionless parameters: ϕ and ℓ_0/D. The mechanical force balance and the polar and nematic order equations become

$$0 = \zeta U_0 m_z - \frac{d\Pi^c}{dz} = 0 \,, \tag{4.49}$$

$$\frac{d}{dz}\left(U_0 \overline{U}\left(Q_{zz} + \frac{1}{d}n\right)\right) + \frac{d-1}{\tau_R} m_z = 0 \,, \tag{4.50}$$

$$\frac{d}{dz}\left(\left(\frac{3\overline{U}}{d+2} - \frac{1}{d}\right) U_0 m_z + \frac{1}{d\zeta}\frac{d\Pi^c}{dz}\right) + \frac{2d}{\tau_R} Q_{zz} = 0 \,, \tag{4.51}$$

where Π^c is the collisional pressure. Combining and integrating eqs. (4.49) and (4.50), we obtain

$$\frac{\zeta U_0 \ell_0}{d-1} \overline{U} Q_{zz} + \Pi^{swim} + \Pi^c = \text{const.} \,, \tag{4.52}$$

[1] The effects of the correlation between the collisional stress and orientation $\nabla \cdot (\boldsymbol{\sigma}\,\boldsymbol{m}/n)/\zeta$ ($\sim O(k^2)$) in the polar order flux (4.46) is investigated in appendix 4.8.

[2] Treating the swim stress as a true stress leads to extremely negative interfacial tension of MIPS which contradicts a stable interfaces between coexisting phases [36, 44, 45].

where $\Pi^{swim} = \zeta U_0 \ell_0 \overline{U} n/(d(d-1))$ is the swim pressure [8, 41]. From the nematic order equation (4.51), $Q_{zz} = 0$ deep inside phases where spatial gradients vanish due to the homogeneity. The sum of the swim and collisional pressures defines an *active* pressure which is identical in the bulk part of coexisting phases. This motivates us to name the undetermined integration constant in eq. (4.49) as the coexistence active pressure Π^{act}_{coex}:

$$\Pi^{act}_{coex} = \Pi^{act}_{\alpha} = \Pi^{act}_{\beta} \ . \tag{4.53}$$

The active pressure represents the pressure exerted by ABPs on a no-flux boundary at steady-state and acts as an observable steady-state pressure. For the mechanical stability $\partial \Pi^{act}/\partial n \geq 0$. Thus, the spinodal is determined by $\partial \Pi^{act}/\partial n = 0$ and the critical point determined by $\partial^2 \Pi^{act}/\partial n^2 = 0$.

To construct the binodal of MIPS, one more condition is required to determine the coexistence active pressure. Now we need to utilize the microscopic information in the continuum-balance equation. From eqs. (4.49), (4.51) and (4.52) we obtain

$$\Pi^{act} - \Pi^{act}_{coex} = \frac{3\ell_0^2}{2d(d-1)(d+2)} \overline{U} \frac{d}{dz} \left(\overline{U} \frac{d\Pi^c}{dz} \right) \ . \tag{4.54}$$

Using the chain rule eq. (4.54) can be expressed as

$$\Pi^{act} - \Pi^{act}_{coex} = \frac{3\ell_0^2}{2d(d-1)(d+2)} \overline{U} \left[\left(\frac{\partial}{\partial n} \left(\overline{U} \frac{\partial \Pi^c}{\partial n} \right) \right) \left(\frac{dn}{dz} \right)^2 + \overline{U} \frac{\partial \Pi^c}{\partial n} \frac{dn^2}{dz^2} \right] \ , \tag{4.55}$$

which has the the same mathematical form with eq. (4.30).[3] Thus, Eifantis and Serrin's analysis [31] applies and there exists an integrating factor (4.35) such that the integration of eq. (4.55) from phase α to β makes the second order gradient terms on the right-hand side disappear. Indeed the existence of such integrating factor is more clearly seen by using the collisional pressure gradient $d\Pi^c/dz$ for the original equation (4.54):

$$\begin{aligned} \int_{\Pi^c_\alpha}^{\Pi^c_\beta} \left[\Pi^{act} - \Pi^{act}_{coex} \right] \, d\Pi^c &= \frac{3\ell_0^2}{2d(d-1)(d+2)} \int_{-\infty}^{\infty} \overline{U} \frac{d\Pi^c}{dz} \frac{d}{dz} \left(\overline{U} \frac{d\Pi^c}{dz} \right) \, dz \\ &= \frac{3\ell_0^2}{4d(d-1)(d+2)} \left[\left(\overline{U} \frac{d\Pi^c}{dz} \right)^2 \right]_{\alpha}^{\beta} = 0 \ , \end{aligned} \tag{4.56}$$

where the last equation is obtained by the homogeneity in each bulk phase.

[3] We note that the gradient terms are all multiplied by ℓ_0^2 and thus are unique to active suspensions. Gradient terms similar to those present in equilibrium systems could be included in (4.54) but are not necessary. Furthermore, these terms are directly connected to the surface tension of an interface, and MIPS interface has been shown to have essentially zero surface tension [36].

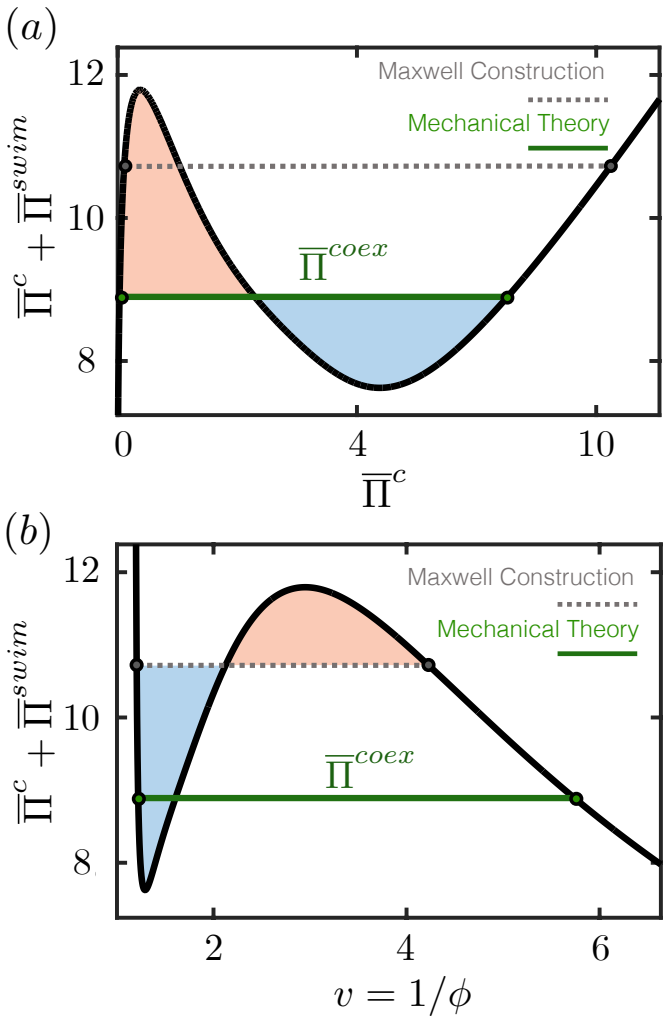

Figure 4.2: (a) Generalized equal-area construction from the mechanical theory (eqs. (4.53) and (4.56)) in the $(\Pi^{act} = [\Pi^c + \Pi^{swim}]\,, \Pi^c)$ plane and (b) Maxwell construction for $\ell_0/D = 35 \times 2^{-1/6}$ in 2D. Pressures are normalized by $\zeta U_0/(\pi D)$. The shaded areas are visual guides for equal-area constructions.

The equivalence of the active pressures (4.53) and the new integral condition (4.56) allows a new generalized equal-area construction for MIPS rather than the conventional Maxwell construction (4.6) for thermodynamic systems. In fig. 4.2(a) we show the equal-area construction of the active pressure $\Pi^{act} = \Pi^c + \Pi^{swim}$ vs. Π^c that determines phase coexistence. From the equal-area construction the collisional pressure in the two phases is determined and then the corresponding number densities are found from the equation of state (EOS) for the collisional pressure. Figure 4.2(b) shows what the corresponding Maxwell construction would predict. The predicted coexistence pressure is larger and correspondingly the dilute phase

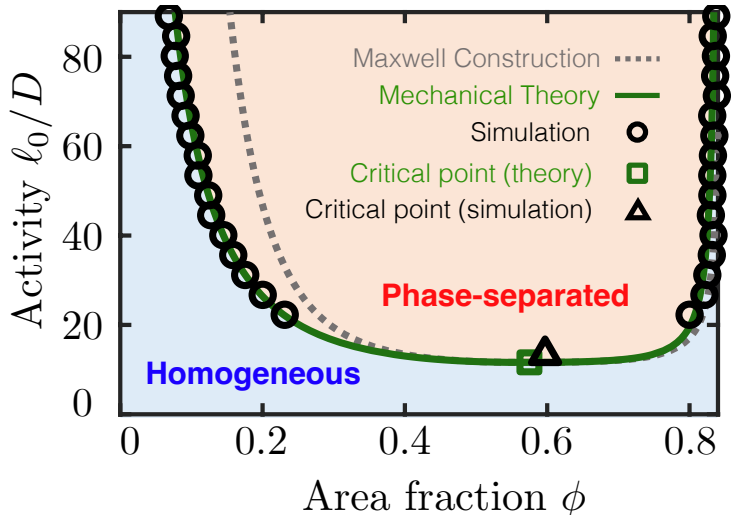

Figure 4.3: Mechanical theory prediction for the phase behavior of active suspensions (solid line) compared with simulations (open circles). Here, $\ell_0/D = U_0\tau_R/D$ and $\phi = \pi D^2 n/4$, is the area fraction of active particles of diameter D. Also shown is the phase boundary from using a Maxwell construction (dotted line).

density is higher.

In order to construct a Π^{act} vs. Π^c plot we need expressions for the collisional and swim pressures as a function of the number density n. For the equal-area construction the equaion of state (EOS) is required. In the following, we use the EOS of ABPs in 2D from the work by Mallory, Omar, and Brady [8], which includes a careful discussion of how to extrapolate homogeneous system behavior into the two-phase region. The EOS in 3D can be obtained from Brownian dynamics simulations by following the procedures in [8] as

$$\frac{\Pi^c}{\zeta U_0/(\pi D^2)} = 6\times 2^{-7/6}\frac{\phi^2}{\sqrt{1-\phi/\phi_0}}\,, \tag{4.57}$$

$$\frac{\Pi^{swim}}{\zeta U_0/(\pi D^2)} = \phi\left(\frac{\ell_0}{D}\right)\overline{U} = \phi\left(\frac{\ell_0}{D}\right)\left[1+\left(1-\exp\left(-2^{7/6}\left(\frac{\ell_0}{D}\right)\right)\frac{\phi}{1-\phi/\phi_0}\right)\right]^{-1}\,, \tag{4.58}$$

where $\phi_0 = 0.645$ is the maximum random packing density achieved in 3D from the simulations. The extrapolation can be challenging, but is made easier here because the collisional pressure is a monotonically increasing function of concentration and, while the swim pressure displays a maximum, the reduction in the swim speed $\overline{U}(n)$ is a monotonically decreasing function of concentration; their sum displays the van-der Waals-like loop shown in figs. 4.2(a) and 4.2(b).

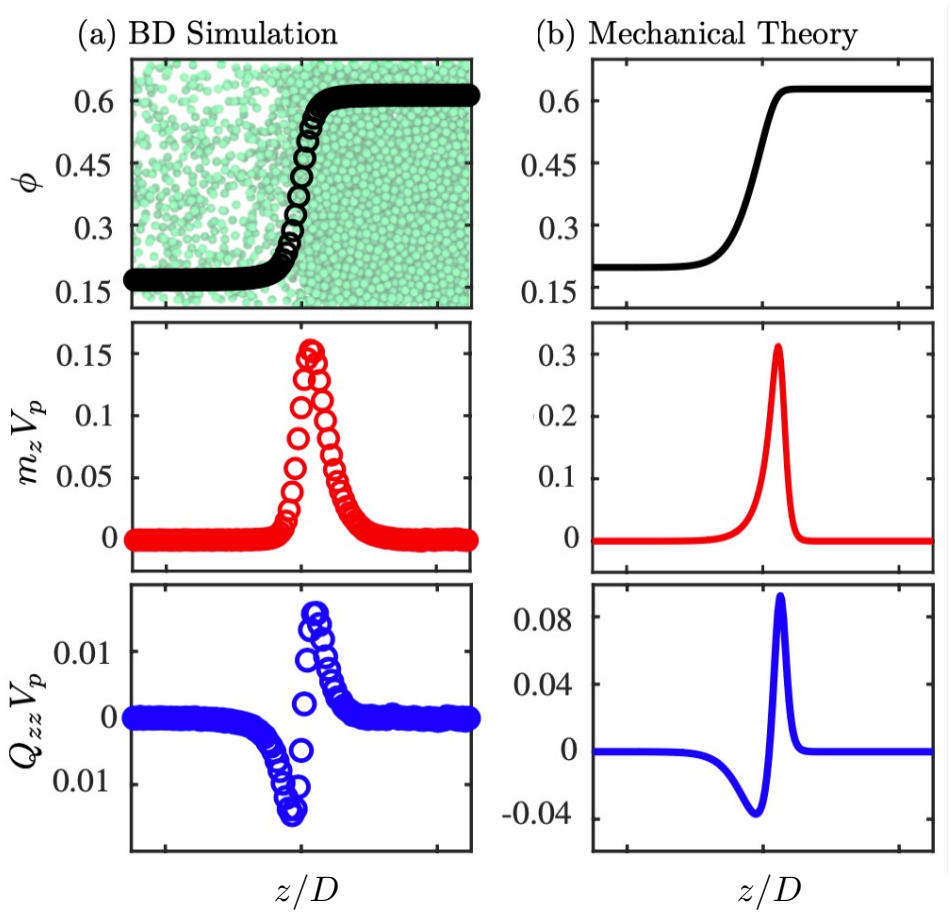

Figure 4.4: Interfacial profiles of the number density, polar order, and nematic order scaled by the volume of a particle $V_p = \pi D^3/6$ at the interface for $\ell_0/D = 50$ in 3D obtained by the a) Brownian Dynamics (BD) simulation and (b) mechanical theory.

Figure 4.3 shows a comparison of this new mechanical theory for the motility-induced phase separation (MIPS) of ABPs in 2D. Also shown for comparison is the phase coexistence predicted via the a Maxwell construction, which over predicts the concentration in the dilute phase. The same Π^c are Π^{swim} are used in both constructions. There are no adjustable parameters in the comparison.

The mechanical theory not only predicts phase coexistence, but, by its very nature, makes predictions about the structure of the interface that can be compared with simulation. A solution of eq. (4.55) is shown in fig. 4.4, where the interfacial profile, polar order, m_z and nematic order, Q_{zz}, are shown in comparison to simulation in this case for 3D in the two-phase region at an activity $\ell_0/D = 50$. From the particle force balance (4.49), the difference in the collisional pressures between the two phases is balanced by the integral of the swim force: $\Delta\Pi^c = \int \zeta U_0 m_z dz$. Particles at the

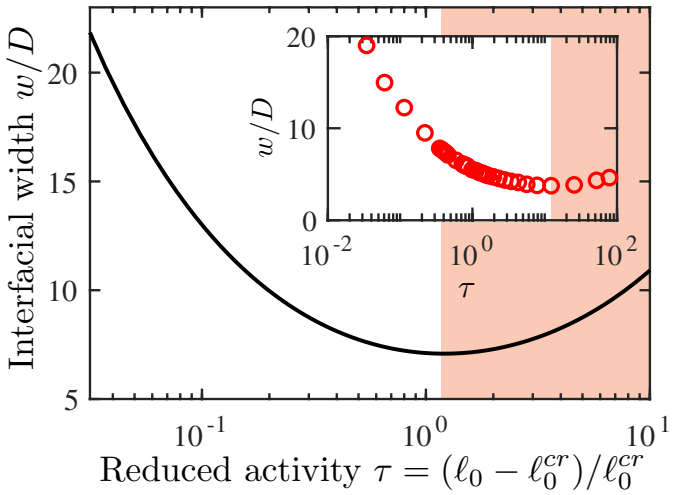

Figure 4.5: Nonmonotonic trend of interfacial width w with activity ℓ_0/D obtained by the mechanical theory and the Brownian Dynamics simulations (inset). The interfacial width is scaled with the diameter of particles D and the reduced activity indicates the departure from the critical activity ℓ_0^{cr}/D, which is the minimum activity required to observe MIPS.

interface are oriented and exert their swim forces *towards* the phase with a higher collisional pressure, or density, in order to suppress an avalanche of particles from the dense to the dilute region. Purely repulsive particles cannot sustain separated dense and gas phases. (This local interfacial swim force density is ultimately why the Maxwell construction does not work.) Figure 4.4 also shows that the polar order is proportional to dn/dz and the nematic order is proportional to dm_z/dz, as predicted by their conservation equations.

The self-compressing feature of MIPS interface engenders a unique non-monotonic trend in the interfacial width as shown in fig. 4.5. When the activity increases as one moves deeper into the two-phase region, the difference of collisional pressures (or densities) between coexisting phases increases, and so must the total swim force provided by the particles at the interface. For sufficiently low activities, the swim force required can be achieved by amplifying the swim force density, $\zeta U_0 \boldsymbol{m} = \zeta U_0 n \langle \boldsymbol{q} \rangle$, with better alignment of orientation $\langle \boldsymbol{q} \rangle$ towards the denser phase, which results in a more compact and thinner interface (see fig. 4.6(a)→(b)).

However, this mode of reinforcement is limited due to the upper bound of the swim force density imposed by close-packing and perfect alignment $|\boldsymbol{q}| = 1$. In order to supply the large required swim force needed at high activity the domain of integration with nonzero m_z, *i.e.* the width of the interface, must increase with

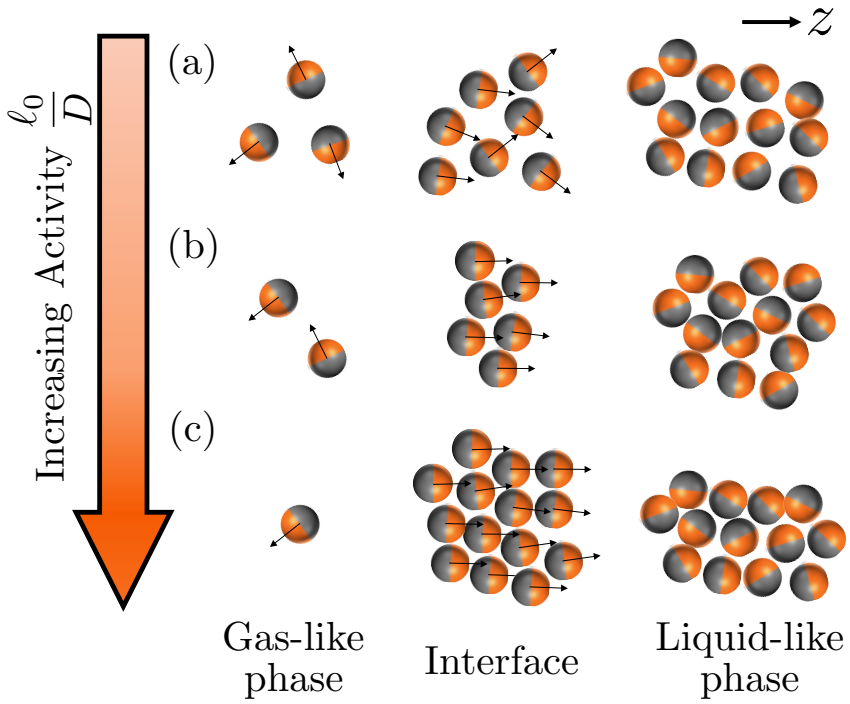

Figure 4.6: A schematic description of the nonmonotonic trend in the interfacial width in MIPS. For the mechanical force balance, the difference of the collisional pressures in two coexisting phases $\Delta\Pi^c$ is balanced by the self-generated swim force from the interface $\int \zeta U_0 m_z \, dz$. (a)→(b) For low activities, extra swim force required for increased collisional pressure difference can be obtained by aligning orientations of the particles at the interface toward the liquid-like phase. Consequently, the interface becomes more compact. (b)→(c) The swim force density per layer is bounded above by $\phi_0 \zeta U_0$, i.e. every particle perfectly aligns toward the liquid-like phase, where ϕ_0 is the maximum packing fraction. To compensate huge difference in the collisional pressures in the two phases, more layer of particles are required and the interfacial width increases.

activity; once a packed layer of particles is fully aligned, more layers are necessary to produce the required swim force (see fig. 4.6(b)→(c)). This is in stark contrast to interfaces in equilibrium thermodynamic systems where the width of the interface decreases monotonically with the distance from the critical point.

4.5 Conclusions

In this Chapter we developed a mechanical theory of phase coexistence that is applicable to both equilibrium and nonequilibrium systems. An essential ingredient for a phase coexistence is that there is no net mass transport in the system; otherwise, phases would not remain in a state of coexistence. To describe the mass transport in a system, a continuum-level mechanical force balance for constituent particles

is derived from mechanical equations of motion for the particles. By including sufficient microscopic details, the mechanical force balance can be used to study the structure of phase interfaces. We note that at least the second-order-gradient effects must be considered to include the nonlocal effects originating from particle interactions and thereby properly describe the interfacial structure. This is because of the reflection symmetry of the number density and stress, which are the central physical quantities in the mechanical description of systems. The mechanical description of phase coexistence is more general than the thermodynamic analog. We show that the thermodynamic chemical equilibrium condition can be recovered by the mechanical theory for equilibrium systems. More importantly, the mechanical perspective can be applied to systems far away from equilibrium since the mechanical force balance is valid regardless whether in or out of equilibrium.

We demonstrated the utility of the mechanical theory in describing nonequilibrium phase behavior by applying it to MIPS. We discover that the steady-state MIPS in a purely active suspension with a uniform activity is described by the equivalence of the active pressure $\Pi^{act} = \Pi^{c} + \Pi^{swim}$ and the integral condition (4.56), which is analogous to the thermodynamic equilibrium condition (4.6). The coexistence conditions allow a generalized equal-area construction on $\Pi^{act} - \Pi^{c}$ plane for a construction of a binodal, which excellently agrees with BD simulations. We also investigated the microscopic structure of phase interfaces of MIPS by directly solving the mechanical force balance equation and discovered a unique nonequilibrium interfacial behavior of MIPS: the interfacial width varies nonmonotonically with the activity of particles. The nonmonotonic trend in the interfacial width can be explained mechanically by the upper bound in the swim force density that is unique to the active matter systems. At low activities, particles at the interface can adjust their orientations toward the denser phase and control the amount of the swim force to balance the difference in the collisional pressures of the coexisting phases. However, each layer of particles at the interface can exert a maximum swim force density $\phi_0 \zeta U_0$. Consequently, a large difference in the collisional pressures at high activities can be balanced only by having more layers of particles at the interface and the interfacial width increases with activity.

We have considered MIPS of purely active hard-spheres in this section to illuminate the fundamental physics underlying MIPS, but in principle phase coexistence in any active, driven, or equilibrium systems can be studied in the framework of the mechanical theory, just by writing a continuum mechanical force balance equation

for constituent particles and computing a pressure equation of state. For example, one can adopt the mechanical perspective to understand the effects of the thermal Brownian motion, complex interaction potentials [46], a spatial variation in transport properties [47], or multiple components (mixture) on MIPS [48–50] for more realistic modeling or interesting applications of MIPS. Indeed, effects of the thermal Brownian motion can be investigated directly with eqs. (4.44)-(4.48). The mechanical force balance equation for the ABPs has the same mathematical form with eq. (4.30) and the binodal and interfacial profiles can be obtained by the same procedures in section 4.4.

4.6 Appendix: Classical Density Functional Theory

In this appendix we provide a brief outline of the classical density functional theory (cDFT) which is helpful in studying static equilibrium properties of inhomogeneous systems. We first consider a system of a simple fluid with an external potential in a grand canonical ensemble at fixed chemical potential μ, volume V, and temperature T. The Hamiltonian $\mathcal{H}$ of the system with N particles is written in a general form as the sum of the kinetic energies, interparticle interaction potential Φ, and external potential ϕ^{ext}:

$$\mathcal{H}(\boldsymbol{x}^N, \boldsymbol{p}^N) = \sum_{i=1}^{N} \frac{\boldsymbol{p}_i^2}{2m} + \Phi(\boldsymbol{x}^N) + \sum_{i=1}^{N} \phi^{ext}(\boldsymbol{x}_i) \,, \tag{4.59}$$

where $\boldsymbol{x}^N = (\boldsymbol{x}_1, \ldots, \boldsymbol{x}_N)$ and $\boldsymbol{p}^N = (\boldsymbol{p}_1, \ldots, \boldsymbol{p}_N)$ are positions and momenta of all the particles in the system. The equilibrium phase space probability density is given by

$$p_N(\boldsymbol{x}^N, \boldsymbol{p}^N) = \frac{1}{\Xi} \exp[-\beta \mathcal{H}(\boldsymbol{x}^N, \boldsymbol{p}^N) + \beta\mu N] \,, \tag{4.60}$$

where

$$\Xi = e^{-\beta W} = \sum_{N=0}^{\infty} \frac{1}{N! v_0^N} \int_V \prod_{i=1}^{N} d\boldsymbol{x}_i \exp\left[-\beta\Phi(\boldsymbol{x}^N) + \sum_{j=1}^{N} \beta\psi(\boldsymbol{x}_j)\right] \tag{4.61}$$

is the grand canonical partition function, $\beta = (k_B T)^{-1}$, W is the grand potential, $\psi(\boldsymbol{x}) = \mu - \phi^{ext}(\boldsymbol{x})$ is the *intrinsic* chemical potential, v_0 is a volume scale which is the cube of the thermal de Broglie wavelength $\lambda_T = h/\sqrt{2\pi m k_B T}$, and h is the Planck constant. Here, the probability density (4.60) is normalized

$$\sum_{N=0}^{\infty} \frac{1}{h^{3N} N!} \int_V \prod_{i=1}^{N} d\boldsymbol{x}_i d\boldsymbol{p}_i p_N(\boldsymbol{x}^N, \boldsymbol{p}^N) = 1 \,, \tag{4.62}$$

and the ensemble average is computed by

$$\langle \cdots \rangle = \sum_{N=0}^{\infty} \frac{1}{h^{3N} N!} \int_V \prod_{i=1}^{N} d\boldsymbol{x}_i d\boldsymbol{p}_i (\cdots) p_N(\boldsymbol{x}^N, \boldsymbol{p}^N) \ . \tag{4.63}$$

Noticing that the total intrinsic chemical potential in the system can be expressed with the microscopic density $\hat{\rho}(\boldsymbol{x}) = \sum_{i=1}^{N} \delta(\boldsymbol{x} - \boldsymbol{x}_i)$ as $\sum_{i=1}^{N} \beta\psi(\boldsymbol{x}_i) = \int_V \hat{\rho}(\boldsymbol{x})\psi(\boldsymbol{x}) \, d\boldsymbol{x}$, the average macroscopic density ρ of the system is obtained as a functional derivative of the grand potential:

$$\rho(\boldsymbol{x}) = \langle \hat{\rho}(\boldsymbol{x}) \rangle = -\frac{\delta W}{\delta \psi(\boldsymbol{x})}. \tag{4.64}$$

We note that eq. (4.64) implies that the microscopic density $\hat{\rho}$ and the intrinsic chemical potential ψ are thermodynamic conjugates and thus the operations for usual thermodynamic conjugate pairs can be applied in the same way with the calculus of variations. For example, the functional derivative of the average density with respect to the intrinsic chemical potential gives the *variance* or fluctuation of the microscopic density:

$$\frac{\delta \rho(\boldsymbol{x})}{\delta \psi(\boldsymbol{x}')} = -\frac{\delta^2 W}{\delta \psi(\boldsymbol{x}') \delta \psi(\boldsymbol{x})} = \beta \langle (\hat{\rho}(\boldsymbol{x}) - \rho(\boldsymbol{x}))(\hat{\rho}(\boldsymbol{x}') - \rho(\boldsymbol{x}')) \rangle \ . \tag{4.65}$$

The variance of the microscopic density $\langle (\hat{\rho}(\boldsymbol{x}) - \rho(\boldsymbol{x}))(\hat{\rho}(\boldsymbol{x}') - \rho(\boldsymbol{x}')) \rangle$ is called the density-density correlation function and its Fourier transform is directly related to the static structure factor of the system.

Equations (4.64) and (4.65) clearly show that the average density is a functional of the intrinsic chemical potential in the grand canonical formulation. For the density functional theory, however, the perspective should be reversed so that thermodynamic variables are treated as functionals of the average density — the *density functionals* as suggested by the name of the theory.

This reverse perspective is achieved by ideas from the seminal works by Hohenberg, Kohn, and Mermin [51, 52], which forms the basis of the electronic density functional theory. Applying their ideas to classical systems, Evans [53] has shown that at fixed temperature and volume there exists a one-to-one correspondence between the equilibrium average density ρ and the intrinsic potential ψ. The one-to-one correspondence allows a unique inverse mapping by which ψ now can be seen as a functional of ρ — there exists a unique intrinsic chemical potential field associated to given average density distribution, T, and V. Consequently, the grand canonical partition function and potential, which are functionals of ψ, can be treated as functionals of ρ.

Now we formulate a variational problem in terms of the average density. In the grand canonical framework, the intrinsic Helmholtz free energy excluding the external potential is written as

$$\mathcal{F} = \left\langle \left(\mathcal{H} - \sum_{i=1}^{N} \phi^{ext}(\boldsymbol{x}_i) \right) + k_B T \ln p_N \right\rangle = \left\langle \sum_{i=1}^{N} \frac{\boldsymbol{p}_i^2}{2m} + \Phi + k_B T \ln p_N \right\rangle, \quad (4.66)$$

where $\langle -k_B T \ln p_N \rangle$ is the Gibbs entropy. Here, we treat p_N and $\mathcal{F}$ as functionals of the average number density ρ *only*. In other words, eq. (4.66) computes the intrinsic Helmholtz free energy for an arbitrary number density profile automatically considering the unique associated intrinsic chemical potential that would result in the given number density profile at equilibrium. Then, we consider

$$W_\psi = \mathcal{F} - \int_V \rho(\boldsymbol{x}) \psi(\boldsymbol{x}) \; b\boldsymbol{x} \; , \quad (4.67)$$

which is also a functional of ρ. When ρ is taken as the density ρ_ψ that would be resulted by the intrinsic chemical potential ψ, W_ψ clearly becomes the grand potential of the system with the intrinsic chemical potential ψ, i.e.

$$W_\psi \big|_{\rho=\rho_\psi} = W|_\psi \; . \quad (4.68)$$

Indeed, ρ_ψ is the global minimizer of W_ψ and satisfies the Euler-Lagrange equation:

$$\left. \frac{\delta W_\psi}{\delta \rho(\boldsymbol{x})} \right|_{\rho=\rho_\psi} = \left. \frac{\delta \mathcal{F}}{\delta \rho(\boldsymbol{x})} \right|_{\rho=\rho_\psi} - \psi(\boldsymbol{x}) = 0 \quad (4.69)$$

which confirms that the grand potential is a (functional) Legendre transform of the intrinsic Helmholtz free energy. Equation (4.69) can be interpreted as the minimization of the total Helmholtz free energy of a system (including the effect of the external potential) in a canonical ensemble. In this perspective the chemical potential μ is a Lagrangian multiplier from the constraint $\int_V \rho(\boldsymbol{x}) \, d\boldsymbol{x} = N$. We note that even in the canonical-ensemble interpretation, the total Helmholtz free energy should be still the one obtained from the grand canonical ensemble as defined in eq (4.66).

Equations (4.68) and (4.69) are the main equations of the cDFT. From eqs. (4.68) and (4.69), one can compute the equilibrium density profile and grand potential from which equilibrium static properties can be obtained [32]. While the formulation of the cDFT is exact, the required intrinsic Helmholtz free energy $\mathcal{F}$ (as a functional of the density) is difficult to obtain. In most problems a free energy functional is

modeled with some approximations (e.g. using the finite measure theory [54] for hard spheres) and the accuracy of the results depends on that of the model. For this reason, one can usually adopt the canonical-ensemble perspective without concerning the subtlety in using the grand-canonical form of the free energy functional — the functional is anyhow modeled approximately.

Indeed, the ideal gas and one-dimensional hard-rods (the Tonk gas) [55] are the only systems for which the exact form of $\mathcal{F}$ is known. For ideal-gas ($\Phi = 0$), it can be easily shown that the grand potential $W^{id} = -k_B T \int_V \exp[\beta\psi]/v_0 \; d\boldsymbol{x}$ and from eq. (4.64) the average density $\rho^{id}(\boldsymbol{x}) = \exp[\beta\psi]/v_0$. Then the intrinsic Helmholtz free energy (4.66) can be parameterized by the average density as $\mathcal{F}^{id} = \int_V k_B T \rho^{id}(\boldsymbol{x})(\ln[\rho^{id}(\boldsymbol{x})v_0] - 1) \; d\boldsymbol{x}$. It is notable that the local intrinsic Helmholtz free energy density is the same with that of a homogeneous ideal gas with the local density since the local state of ideal gas is not affected by the states of neighboring regions due to the lack of interactions. It is customary to separate the ideal contribution from the the intrinsic free energy and write $\mathcal{F} = \mathcal{F}^{id} + \mathcal{F}^{ex}$, where the deviation from the ideal case $\mathcal{F}^{ex}$ is called the excess intrinsic Helmholtz free energy.

4.7 Appendix: Orientational Moment Equations of Interacting Active Brownian Particles

In this appendix we provide a systematic derivation of coarse-grained equations that govern evolution of 1-body orientational moment fields in a suspension of N interacting active Brownian particles (ABPs). We start by writing the Smoluchowski equation that is equivalent to the microscopic mechanical equations of motions for ABPs (4.37)-(4.41):

$$\frac{\partial P_N}{\partial t} + \sum_\alpha \nabla_\alpha \cdot \boldsymbol{j}_\alpha^T + \sum_\alpha \nabla_\alpha^R \cdot \boldsymbol{j}_\alpha^R = 0. \tag{4.70}$$

Here, $P_N(\boldsymbol{\zeta}_N, t)$ is the probability density function of observing a configuration $\boldsymbol{\zeta}_N \equiv (\boldsymbol{x}_1, \boldsymbol{x}_2, ..., \boldsymbol{x}_N, \boldsymbol{q}_1, \boldsymbol{q}_2, ..., \boldsymbol{q}_N)$ at a time t, $\boldsymbol{x}_\alpha$ and $\boldsymbol{q}_\alpha$ are position and orientation vectors of particle α, $\boldsymbol{j}_\alpha^T$ and $\boldsymbol{j}_\alpha^R$ are translational and rotational fluxes of particle α, $\nabla_\alpha = \partial/\partial\boldsymbol{x}_\alpha$, and $\nabla_\alpha^R = \boldsymbol{q}_\alpha \times \partial/\partial\boldsymbol{q}_\alpha$. The fluxes are given by

$$\boldsymbol{j}_\alpha^T = U_0 \boldsymbol{q}_\alpha P_N + \frac{1}{\zeta}\boldsymbol{F}_\alpha P_N - D_T \nabla_\alpha P_N, \tag{4.71}$$

$$\boldsymbol{j}_\alpha^R = -D_R \nabla_\alpha^R P_N, \tag{4.72}$$

where U_0 is the self-propelling or swim speed in free space, ζ is the translational drag coefficient of ABPs, D_T and D_R $(= 1/\tau_R)$ are translational and rotational diffusivities, and $\boldsymbol{F}_\alpha$ is the force on particle α due to the potential energy. The three terms in the translational flux (4.71) represent transports via self-propulsion (active convection), conservative forces, and translational diffusion, respectively.

We model interparticle interaction potential to be pairwise additive. Then the conservative force on particle α can be written as $\boldsymbol{F}_\alpha = \boldsymbol{F}_\alpha^{ext} + \sum_\beta \boldsymbol{F}_{\alpha\beta}$, where $\boldsymbol{F}_\alpha^{ext} = -\nabla_\alpha \phi^{ext}(\boldsymbol{x}_\alpha)$ is force on particle α resulted by the external potential energy ϕ^{ext} and $\boldsymbol{F}_{\alpha\beta} = -\nabla_\alpha U_2(\boldsymbol{x}_\alpha, \boldsymbol{x}_\beta)$ is pairwise interparticle force exerted by the particle β on particle α. Here, we define $\boldsymbol{F}_{\alpha\alpha} \equiv 0$ for all $\alpha \in \{1, 2, ..., N\}$ for convenience in notation. We consider spherical (or circular in 2D) ABPs and model pair interactions to be isotropic, i.e. $U_2(\boldsymbol{x}_\alpha,\ \boldsymbol{x}_\beta) = U_2(|\boldsymbol{x}_\alpha - \boldsymbol{x}_\beta|)$.

We first derive an evolution equation of the number density field to consider mass transport. The first step is to project the full probability distribution function P_N onto the number density field. For the projection, we introduce the microscopic number density $\hat{n}(\boldsymbol{x}; \boldsymbol{\zeta}_N) = \sum_\alpha \delta(\boldsymbol{x} - \boldsymbol{x}_\alpha)$. The number density field $n(\boldsymbol{x}, t)$ is then obtained by averaging the microscopic number density over all configurations $n(\boldsymbol{x}, t) = \langle \hat{n}(\boldsymbol{x}; \boldsymbol{\zeta}_N) \rangle$, where $\langle (\cdot) \rangle \equiv \int d\boldsymbol{\zeta}_N (\cdot) P_N(\boldsymbol{\zeta}_N, t)$. Note that integral symbol is written only once but it is indeed $(2d-1)N$-fold (dN from positions and $(d-1)N$ from orientations), where d is the spatial dimension.

Applying the divergence theorem to the Smoluchowski equation (4.70) the time rate change of the number density field is obtained as

$$\frac{\partial n}{\partial t} + \nabla \cdot \boldsymbol{j}_n = 0, \tag{4.73}$$

$$\begin{aligned} \boldsymbol{j}_n &= \sum_\alpha \int d\boldsymbol{\zeta}_N \, \boldsymbol{j}_\alpha^T \delta(\boldsymbol{x} - \boldsymbol{x}_\alpha) \\ &= \sum_\alpha \int d\boldsymbol{\zeta}_N \left(U_0 \boldsymbol{q}_\alpha P_N + \frac{1}{\zeta} \boldsymbol{F}_\alpha P_N - D_T \nabla_\alpha P_N \right) \delta(\boldsymbol{x} - \boldsymbol{x}_\alpha), \end{aligned} \tag{4.74}$$

where $\nabla = \partial / \partial \boldsymbol{x}$ and $\boldsymbol{j}_n$ is the number density flux. Now we investigate how each term in the translational flux $\boldsymbol{j}_\alpha^T$ contributes to $\boldsymbol{j}_n$. The first term corresponding to the self-propulsion invokes the definition of the microscopic polar order density $\hat{\boldsymbol{m}}(\boldsymbol{x}; \boldsymbol{\zeta}_N) = \sum_\alpha \delta(\boldsymbol{x} - \boldsymbol{x}_\alpha) \boldsymbol{q}_\alpha$. Upon averaging, it brings about the polar order field $\boldsymbol{m}(\boldsymbol{x}, t) = \langle \hat{\boldsymbol{m}}(\boldsymbol{x}; \boldsymbol{\zeta}_N) \rangle$ and $U_0 \boldsymbol{m}$ accounts for the active convective transport of the number density. Indeed it is well-known that an orientational moment of

the probability distribution function is coupled to its next order moment due to the active convection term [39, 40]. This results a hierarchical structure of orientational moment equations and hence a proper closure is required as we will discuss later in this appendix. The second term represents the effect of forces on particles. By using the sifting property of the Dirac δ function, the contribution of the external force $\boldsymbol{F}_\alpha^{ext} = -\nabla_\alpha \phi^{ext}(\boldsymbol{x}_\alpha)$ is simplified as

$$\begin{aligned}\sum_\alpha \int d\boldsymbol{\zeta}_N \, \boldsymbol{F}_\alpha^{ext} P_N(\boldsymbol{\zeta}_N, t)\delta(\boldsymbol{x}-\boldsymbol{x}_\alpha) &= \sum_\alpha \int d\boldsymbol{\zeta}_N \, (-\nabla\phi^{ext}(\boldsymbol{x}))P_N(\boldsymbol{\zeta}_N, t)\delta(\boldsymbol{x}-\boldsymbol{x}_\alpha) \\ &= -\nabla\phi^{ext}(\boldsymbol{x}) \int d\boldsymbol{\zeta}_N \, \sum_\alpha \delta(\boldsymbol{x}-\boldsymbol{x}_\alpha) P_N(\boldsymbol{\zeta}_N, t) \\ &= \boldsymbol{F}^{ext}(\boldsymbol{x})(\boldsymbol{x}) n(\boldsymbol{x}, t).\end{aligned}$$

Following the Irving-Kirkwood-Noll procedure [33, 37, 38] the contribution of interparticle forces can be expressed as the divergence of the collisional stress

$$\boldsymbol{\sigma}^c = -\frac{1}{2} \int d\boldsymbol{x}_\alpha \int d\boldsymbol{x}_\beta \, \boldsymbol{r}_{\alpha\beta} \boldsymbol{F}_{\alpha\beta} \, \rho^{(2)}(\boldsymbol{x}_\alpha, \boldsymbol{x}_\beta, t) \, b_{\alpha\beta}(\boldsymbol{x}) \, . \tag{4.75}$$

Here, $\boldsymbol{r}_{\alpha\beta} = \boldsymbol{x}_\alpha - \boldsymbol{x}_\beta$ and $b_{\alpha\beta}(\boldsymbol{x}) = \int_0^1 d\lambda \; \delta(\boldsymbol{x} - \boldsymbol{x}_\beta - \lambda \boldsymbol{r}_{\alpha\beta})$ is a bond function. Finally, the contribution of the translational diffusion is easily integrated by using the sifting property:

$$\begin{aligned}\sum_\alpha \int d\boldsymbol{\zeta}_N \, \nabla_\alpha P_N(\boldsymbol{\zeta}_N, t)\delta(\boldsymbol{x}-\boldsymbol{x}_\alpha) &= \sum_\alpha \int d\boldsymbol{\zeta}_N \, \nabla P_N(\boldsymbol{\zeta}_N, t)\delta(\boldsymbol{x}-\boldsymbol{x}_\alpha) \\ &= \nabla \int d\boldsymbol{\zeta}_N \, \sum_\alpha \delta(\boldsymbol{x}-\boldsymbol{x}_\alpha) P_N(\boldsymbol{\zeta}_N, t) = \nabla n(\boldsymbol{x}, t) \, .\end{aligned}$$

Now the number density flux (4.74) becomes

$$\boldsymbol{j}_n = U_0 \boldsymbol{m} + \frac{1}{\zeta} \left(\boldsymbol{F}^{ext} n + \nabla \cdot \boldsymbol{\sigma}^c \right) - D_T \nabla n \, . \tag{4.76}$$

It is noteworthy that eqs. (4.73) and (4.76) are exact. The number density evolution equation (4.73) implies $\nabla \cdot \boldsymbol{j}_n = 0$ at a steady state. For suspensions of ABPs with unidirectional variations $\boldsymbol{j}_n = \boldsymbol{0}$, which implies

$$\zeta U_0 \boldsymbol{m} - \nabla\phi^{ext} n + \nabla \cdot \boldsymbol{\sigma}^c - \zeta D_T \nabla n = \boldsymbol{0} \, . \tag{4.77}$$

This is indeed a microscopic mechanical force balance on the particle phase. We highlight that the first term $\zeta U_0 \boldsymbol{m}$ arising from net orientation of ABPs acts as a self-generated body force density.

Next, in order to understand how the self-generated body force density develops we investigate an evolution of the polar order field $\boldsymbol{m}$. From the definition of the polar order and the Smoluchowski equation (4.70), applications of the divergence theorem give

$$\frac{\partial \boldsymbol{m}}{\partial t} + \nabla \cdot \boldsymbol{j}_m + (d-1) D_R \boldsymbol{m} = \boldsymbol{0} \,, \tag{4.78}$$

$$\boldsymbol{j}_m = U_0 \tilde{\boldsymbol{Q}} + \sum_\alpha \int d\boldsymbol{\zeta}_N \, \frac{1}{\zeta} \sum_\beta \boldsymbol{F}_{\alpha\beta} P_N \boldsymbol{q}_\alpha \delta(\boldsymbol{x} - \boldsymbol{x}_\alpha) + \frac{1}{\zeta} \boldsymbol{F}^{ext} \boldsymbol{m} - D_T \nabla \boldsymbol{m} \,, \tag{4.79}$$

where $\boldsymbol{j}_m$ is the polar order flux and $\tilde{\boldsymbol{Q}}(\boldsymbol{x}, t) = \langle \hat{\tilde{\boldsymbol{Q}}}(\boldsymbol{x}; \boldsymbol{\zeta}_N) \rangle = \langle \sum_\alpha \delta(\boldsymbol{x} - \boldsymbol{x}_\alpha) \boldsymbol{q}_\alpha \boldsymbol{q}_\alpha \rangle$. The last two terms in eq. (4.79) are obtained by straightforward integrations using the sifting property as shown before.

For the interparticle forces we generalize the Irving-Kirkwood-Noll procedure as following. We first obtain a symmetric form by adding the same expression to itself after switching the indices of summation:

$$\begin{aligned}
(\mathrm{IP})_m \equiv & \sum_\alpha \int d\boldsymbol{\zeta}_N \, \sum_\beta \boldsymbol{F}_{\alpha\beta} \boldsymbol{q}_\alpha P_N \delta(\boldsymbol{x} - \boldsymbol{x}_\alpha) = \sum_\beta \int d\boldsymbol{\zeta}_N \, \sum_\alpha \boldsymbol{F}_{\beta\alpha} \boldsymbol{q}_\beta P_N \delta(\boldsymbol{x} - \boldsymbol{x}_\beta) \\
= & \frac{1}{2} \sum_\alpha \sum_\beta \int d\boldsymbol{\zeta}_N \, \boldsymbol{F}_{\alpha\beta} \Big(\boldsymbol{q}_\alpha \delta(\boldsymbol{x} - \boldsymbol{x}_\alpha) - \boldsymbol{q}_\beta \delta(\boldsymbol{x} - \boldsymbol{x}_\beta) \Big) P_N \\
= & \frac{1}{2} \sum_\alpha \sum_\beta \int d\boldsymbol{\zeta}_N \, \boldsymbol{F}_{\alpha\beta} \left[(\boldsymbol{q}_\beta + \lambda \boldsymbol{n}_{\alpha\beta}) \delta(\boldsymbol{x} - \boldsymbol{x}_\beta - \lambda \boldsymbol{r}_{\alpha\beta}) \right]_{\lambda=0}^{\lambda=1} P_N \,,
\end{aligned} \tag{4.80}$$

where $\boldsymbol{n}_{\alpha\beta} = \boldsymbol{q}_\alpha - \boldsymbol{q}_\beta$ is the relative orientation vector. Then we rewrite the bracketed term as

$$\begin{aligned}
\left[(\boldsymbol{q}_\beta + \lambda \boldsymbol{n}_{\alpha\beta}) \delta(\boldsymbol{x} - \boldsymbol{x}_\beta - \lambda \boldsymbol{r}_{\alpha\beta}) \right]_{\lambda=0}^{\lambda=1} &= \int_0^1 d\lambda \, \frac{\partial}{\partial \lambda} \Big((\boldsymbol{q}_\beta + \lambda \boldsymbol{n}_{\alpha\beta}) \delta(\boldsymbol{x} - \boldsymbol{x}_\beta - \lambda \boldsymbol{r}_{\alpha\beta}) \Big) \\
&= \boldsymbol{n}_{\alpha\beta} b_{\alpha\beta}(\boldsymbol{x}) - \boldsymbol{r}_{\alpha\beta} \cdot \nabla \boldsymbol{c}_{\alpha\beta}(\boldsymbol{x}) \,,
\end{aligned} \tag{4.81}$$

where $\boldsymbol{c}_{\alpha\beta} = \int_0^1 d\lambda \, (\boldsymbol{q}_\beta + \lambda \boldsymbol{n}_{\alpha\beta}) \delta(\boldsymbol{x} - \boldsymbol{x}_\beta - \lambda \boldsymbol{r}_{\alpha\beta})$. Thus, eq. (4.80) is rewritten as

$$(\mathrm{IP})_m = \frac{1}{2} \sum_\alpha \sum_\beta \int d\boldsymbol{\zeta}_N \, \boldsymbol{F}_{\alpha\beta} \boldsymbol{n}_{\alpha\beta} b_{\alpha\beta} P_N + \nabla \cdot \left[-\frac{1}{2} \sum_\alpha \sum_\beta \int d\boldsymbol{\zeta}_N \, \boldsymbol{r}_{\alpha\beta} \boldsymbol{F}_{\alpha\beta} \boldsymbol{c}_{\alpha\beta} P_N \right] . \tag{4.82}$$

While the contribution of the interparticle forces to the number density flux could be related to the well-known collisional stress, the two terms on the right-hand side of eq. (4.82) uniquely arise for ABPs and their physical meanings have not been explored.

The first term can be interpreted as a measure of how much two ABPs mutually impede self-propulsion of each other. This can be understood by the following reasoning. First, due to the presence of interparticle force $\boldsymbol{F}_{\alpha\beta}$ in the integrand, it is sufficient to consider configurations with particles (nearly) at contact when particles are (sufficiently) hard. Let us consider a pair of touching APBs that are oriented towards the same orientation. Both particles swim freely since they are not *colliding* with each other. Such configurations, however, do not contribute to the integration since corresponding $\boldsymbol{n}_{\alpha\beta} = \boldsymbol{0}$. On the other hand a pair of APBs with orientations exactly opposite to each other maximizes the magnitude of $\boldsymbol{n}_{\alpha\beta}$ and can contribute the most to the integral. In this case, there are two possible scenarios which are particles (i) colliding head-to-head ($\boldsymbol{F}_{\alpha\beta} \cdot \boldsymbol{n}_{\alpha\beta} < 0$) or (ii) swimming apart ($\boldsymbol{F}_{\alpha\beta} \cdot \boldsymbol{n}_{\alpha\beta} > 0$). Among the two, only the former type of configurations needs to be considered because the latter is scarcely weighted by the probability density function P_N [56, 57]. Therefore the first term in eq. (4.82) should increase with the reduction in active convective transport of polar order due to collisions generated by the relative self-propelling motion. We write the amount of the reduction as $U_0(1-\overline{U}_m)\tilde{\boldsymbol{Q}}$, where $\overline{U}_m$ represents the effective speed of active convective transport of polar order relative to the free self-propulsive speed.

This interpretation can be more clearly seen and be even generalized to higher order orientational moments by relating an interparticle interaction term in a flux to the effective swim speed. The effective swim speed of ABPs is computed from the swim stress (and pressure) by using the impulse formula [8, 16, 58, 59]

$$\boldsymbol{\sigma}^{swim} = -\frac{1}{(d-1)VD_R}\sum_{\alpha}\langle \boldsymbol{v}_\alpha \boldsymbol{F}_\alpha^{swim}\rangle. \tag{4.83}$$

Here, V is the volume of a system, $\boldsymbol{F}_\alpha^{swim} = \zeta U_0 \boldsymbol{q}_\alpha$ is the swim force responsible for the self-propulsion, and $\boldsymbol{v}_\alpha$ is the velocity of the αth particle. From the over-damped Langevin equation, the swim stress in a homogeneous suspension of ABPs is rewritten as

$$\boldsymbol{\sigma}^{swim} \equiv -\frac{n\zeta U_0^2 \overline{U}}{d(d-1)\tau_R}\boldsymbol{I} = -\frac{n\zeta U_0^2}{d(d-1)\tau_R}\left(\boldsymbol{I} + \frac{1}{\zeta U_0}\left\langle \sum_\beta \boldsymbol{F}_{\alpha\beta}\boldsymbol{q}_\alpha \right\rangle\right). \tag{4.84}$$

Therefore, the contribution of interparticle interactions to the flux of the pth orien-

tational moment can be approximated as

$$\frac{1}{\zeta}\sum_{\alpha}\left\langle\sum_{\beta}\boldsymbol{F}_{\alpha\beta}\underbrace{\boldsymbol{q}_{\alpha}\ldots\boldsymbol{q}_{\alpha}}_{p}\delta(\boldsymbol{x}-\boldsymbol{x}_{\alpha})\right\rangle=\frac{1}{\zeta}\sum_{\alpha}\left\langle\sum_{\beta}\boldsymbol{F}_{\alpha\beta}(\boldsymbol{q}_{\alpha}\cdot\underbrace{\boldsymbol{q}_{\alpha})\boldsymbol{q}_{\alpha}\ldots\boldsymbol{q}_{\alpha}}_{p+1}\delta(\boldsymbol{x}-\boldsymbol{x}_{\alpha})\right\rangle$$
$$\approx U_0(1-\overline{U})\sum_{\alpha}\left\langle\underbrace{\boldsymbol{q}_{\alpha}\ldots\boldsymbol{q}_{\alpha}}_{p+1}\delta(\boldsymbol{x}-\boldsymbol{x}_{\alpha})\right\rangle, \tag{4.85}$$

where the error of the approximation stems from the covariance of $\boldsymbol{F}_{\alpha\beta}\boldsymbol{q}_{\alpha}$ and $\underbrace{\boldsymbol{q}_{\alpha}\ldots\boldsymbol{q}_{\alpha}}_{p+1}$. It is notable that eq. (4.85) implies that the reduction in the speed of active convection should be similar in magnitude for all orders.

Consequently, the second term on the right-hand side of eq. (4.82) can be understood as the correlation between the collisional stress (force) and the orientation. This can be also seen by Taylor expanding $\boldsymbol{c}_{\alpha\beta}$ and rewriting the integral in the bracket as

$$-\frac{1}{2}\sum_{\alpha}\sum_{\beta}\int d\boldsymbol{\zeta}_N\,\boldsymbol{r}_{\alpha\beta}\boldsymbol{F}_{\alpha\beta}\boldsymbol{c}_{\alpha\beta}P_N=-\frac{1}{2}\sum_{\alpha}\sum_{\beta}\int d\boldsymbol{\zeta}_N\,\boldsymbol{r}_{\alpha\beta}\boldsymbol{F}_{\alpha\beta}\boldsymbol{q}_{\alpha}b_{\alpha\beta}P_N$$
$$+\nabla\cdot\left[-\frac{1}{4}\sum_{\alpha}\sum_{\beta}\int d\boldsymbol{\zeta}_N\,\boldsymbol{r}_{\alpha\beta}\boldsymbol{r}_{\alpha\beta}\boldsymbol{F}_{\alpha\beta}\boldsymbol{n}_{\alpha\beta}b'_{\alpha\beta}P_N\right], \tag{4.86}$$

where $b'_{\alpha\beta}=\int_0^1 d\lambda\int_0^1 d\lambda'\,\lambda(1-2\lambda)\delta(\boldsymbol{x}-\boldsymbol{x}_{\beta}-(\lambda+\lambda'(1-2\lambda))\boldsymbol{r}_{\alpha\beta})$. Since we close the hierarchy by truncating terms with an order of $O(k^3)$ or higher in Fourier space, the second term does not appear in our final equations. However, we demonstrate that it should broaden the predicted binodal of MIPS in appendix 4.8. Finally, the polar order flux is written as

$$\boldsymbol{j}_m=U_0\overline{U}_m\tilde{\boldsymbol{Q}}+\frac{1}{\zeta}\boldsymbol{F}^{ext}\boldsymbol{m}-D_T\nabla\boldsymbol{m}\ . \tag{4.87}$$

We perform a similar procedure to derive an evolution equation of $\tilde{\boldsymbol{Q}}$:

$$\frac{\partial\tilde{\boldsymbol{Q}}}{\partial t}+\nabla\cdot\boldsymbol{j}_{\tilde{Q}}+2dD_R\left(\tilde{\boldsymbol{Q}}-\frac{1}{d}n\boldsymbol{I}\right)=\boldsymbol{0}\,, \tag{4.88}$$

$$\boldsymbol{j}_{\tilde{Q}}=U_0\tilde{\boldsymbol{B}}+\sum_{\alpha}\int d\boldsymbol{\zeta}_N\,\frac{1}{\zeta}\sum_{\beta}\boldsymbol{F}_{\alpha\beta}\boldsymbol{q}_{\alpha}\boldsymbol{q}_{\alpha}P_N\delta(\boldsymbol{x}-\boldsymbol{x}_{\alpha})+\frac{1}{\zeta}\boldsymbol{F}^{ext}\tilde{\boldsymbol{Q}}-D_T\nabla\tilde{\boldsymbol{Q}}\ , \tag{4.89}$$

where $\tilde{\boldsymbol{B}}(\boldsymbol{x},t) = \langle \sum_\alpha \boldsymbol{q}_\alpha \boldsymbol{q}_\alpha \boldsymbol{q}_\alpha \delta(\boldsymbol{x}-\boldsymbol{x}_\alpha)\rangle$. Applying the treatment described in eqs. (4.80) and (4.81), the interparticle force term can be rewritten as

$$\sum_\alpha \int d\boldsymbol{\zeta}_N \sum_\beta \boldsymbol{F}_{\alpha\beta}\boldsymbol{q}_\alpha\boldsymbol{q}_\alpha P_N \delta(\boldsymbol{x}-\boldsymbol{x}_\alpha) = \frac{1}{2}\sum_\alpha\sum_\beta \int d\boldsymbol{\zeta}_N \, \boldsymbol{F}_{\alpha\beta}(\boldsymbol{q}_\alpha \boldsymbol{n}_{\alpha\beta} + \boldsymbol{n}_{\alpha\beta}\boldsymbol{q}_\alpha) b_{\alpha\beta} P_N + \nabla\cdot\left[-\frac{1}{2}\sum_\alpha\sum_\beta \int d\boldsymbol{\zeta}_N \, \boldsymbol{r}_{\alpha\beta}\boldsymbol{F}_{\alpha\beta}\boldsymbol{d}_{\alpha\beta}P_N\right], \tag{4.90}$$

where $\boldsymbol{d}_{\alpha\beta} = \int_0^1 d\lambda \; (\boldsymbol{q}_\beta\boldsymbol{q}_\beta + \lambda \boldsymbol{u}_{\alpha\beta})\delta(\boldsymbol{x}-\boldsymbol{x}_\beta-\lambda\boldsymbol{r}_{\alpha\beta})$. As discussed above, the first term indicates that the active convective transport of $\tilde{\boldsymbol{Q}}$ is restrained due to collisions. We model the reduction in speed of the transport as $U_0(1-\overline{U}_Q)\tilde{\boldsymbol{B}}$. The second term is assumed to be negligible due to its order of $O(k^4)$ in Fourier space. The integral inside the bracket can be shown to be related to the correlation between the collisional stress and $\tilde{\boldsymbol{Q}}$ by Taylor expanding $\boldsymbol{d}_{\alpha\beta}$ as shown in eq. (4.86). Therefore, $\tilde{\boldsymbol{Q}}$-flux is now given by

$$\boldsymbol{j}_{\tilde{Q}} = U_0\overline{U}_Q\tilde{\boldsymbol{B}} + \frac{1}{\zeta}\nabla\boldsymbol{F}^{ext}\tilde{\boldsymbol{Q}} - D_T\nabla\tilde{\boldsymbol{Q}}. \tag{4.91}$$

As we discussed in section 4.4, evolution equations for orientational moments up to the second order form the minimal set of microscopic mechanical equations to describe phase separations and boundaries without extra assumptions. By all means one can continue deriving equations for higher orientational moments following the procedure described above to include the higher order corrections that can be potentially important for extremely high activities. However, our results show that closing the hierarchy at the second order is indeed sufficient for an accurate prediction of binodals for an expansive range of activities.

For the closure we first separate orientational moments into traceless parts and remainders — a remainder includes dependency on the lower order moments: $\tilde{\boldsymbol{Q}} = \boldsymbol{Q} + n\boldsymbol{I}/d$ and $\tilde{\boldsymbol{B}} = \boldsymbol{B} + \boldsymbol{\alpha}\cdot\boldsymbol{m}/(d+2)$, where $\boldsymbol{\alpha}$ is the fourth order isotropic tensor and $\boldsymbol{Q}$ is the nematic order field. Then we close the hierarchy by assuming that terms with an order of $O(k^3)$ or higher in Fourier space are negligible at steady state. The evolution equation of $\tilde{\boldsymbol{Q}}$ is converted to that of $\boldsymbol{Q}$ by using eq. (4.73):

$$\frac{\partial \boldsymbol{Q}}{\partial t} + \nabla\cdot\boldsymbol{j}_Q + 2dD_R\boldsymbol{Q} = \boldsymbol{0}, \tag{4.92}$$

$$\boldsymbol{j}_Q = U_0\boldsymbol{m}\cdot\left(\frac{\overline{U}_Q}{d+2}\boldsymbol{\alpha} - \frac{1}{d}\boldsymbol{I}\boldsymbol{I}\right) + \frac{1}{\zeta}\boldsymbol{F}^{ext}\boldsymbol{Q} - \frac{1}{d\zeta}\nabla\cdot\boldsymbol{\sigma}^c\boldsymbol{I} - D_T\nabla\boldsymbol{Q}. \tag{4.93}$$

Finally, eqs. (4.73), (4.76), (4.78), (4.87), (4.92), and (4.93) form a closed set of equations. Now we consider a suspension of ABPs at a steady state without an imposed external potential energy. When a system has a unidirectional variation, say z-direction without loss of generality, governing equations are given by

$$j_{n,z} = U_0 m_z - \frac{1}{\zeta}\frac{d\Pi^c}{dz} - D_T\frac{dn}{dz} = 0, \tag{4.94}$$

$$\frac{d}{dz}\left(U_0\overline{U}\left(Q_{zz} + \frac{1}{d}n\right) - D_T\frac{dm_z}{dz}\right) + (d-1)D_R m_z = 0, \tag{4.95}$$

$$\frac{d}{dz}\left(\left(\frac{3\overline{U}}{d+2} - \frac{1}{d}\right)U_0 m_z + \frac{1}{d\zeta}\frac{d\Pi^c}{dz} - D_T\frac{dQ_{zz}}{dz}\right) + 2dD_R Q_{zz} = 0, \tag{4.96}$$

where Π^c is the collisional pressure defined by $\boldsymbol{\sigma}^c = -\Pi^c \boldsymbol{I}$. Here, we approxiamte $\overline{U}_m \approx \overline{U}_Q \equiv \overline{U}$ since the reduction in the active convective speed is similar for all orientational moments as discusses above.

In a recent work by Speck [60], a similar but different set of equations has been proposed to describe MIPS. The equations have two crucial differences from ours. First, the nematic order is approximated by a simplified ad hoc expression in [60]. Second, Speck simplifies the exact equation eqs. (4.73) and (4.76) by assuming that the collisional stress and the active convective term in the number density flux can be lumped as one $U_0\boldsymbol{m} + \nabla\cdot\boldsymbol{\sigma}^c \approx U_0\overline{U}\boldsymbol{m}$ as we treat fluxes of higher order moments. Consequently in [60], eq. (4.94) is approximated as

$$m_z = \frac{D_T}{U_0\overline{U}}\frac{dn}{dz}. \tag{4.97}$$

We remark that this approximation can lead to unphysical conclusions. For instance setting $U_0 = 0$ in eq. (4.97) results an equation for non-interacting colloids rather than a hard-sphere suspension. Also, it is obvious that the approximation cannot be applied to athermal ($D_T = 0$) situations. Moreover, it is notable that the assumption in [60] indeed lifts the necessity of the equation of state describing the collisional stress. This can be seen by applying the chain rule to the exact eq. (4.94)

$$m_z = \frac{1}{U_0}\left(\frac{1}{\zeta}\frac{d\Pi^c}{dz} + D_T\frac{dn}{dz}\right) = \frac{1}{U_0}\left(\frac{1}{\zeta}\frac{d\Pi^c}{dn} + D_T\right)\frac{dn}{dz}. \tag{4.98}$$

The comparison of eqs. (4.97) and (4.98) leads to the self-consistent condition for the approximation

$$\frac{d\Pi^c}{dn} = \zeta D_T\left(\frac{1}{\overline{U}} - 1\right), \tag{4.99}$$

which is not satisfied in [60]. Indeed, eq. (4.99) shows why $\int dn\, 1/\overline{U}$ instead of Π^c could have been used in [60] as an integrating factor to determine the binodal within our framework; the correct integrating factor Π^c can be expressed as the integral of $1/\overline{U}$ under aforementioned Speck's assumption.

4.8 Appendix: Effects of Correlation between Collisional Stress and Orientation

As discussed in appendix 4.7 the full $\boldsymbol{m}-$flux expresses the correlation between collisional stress and orientation. In this appendix we discuss the leading order effects of the stress-orientation correlation on the binodal. From eq. (4.86) we pose a simple form of the correlation as $\upsilon\nabla\cdot(\boldsymbol{\sigma}^c\boldsymbol{m}/n)$, where υ is a parameter that controls the significance of the term. This modifies our $\boldsymbol{m}-$field equation (4.95) as

$$\frac{d}{dz}\left(U_0\overline{U}_m\left(Q_{zz}+\frac{1}{d}n\right)-D_T\frac{dm_z}{dz}-\frac{\upsilon}{\zeta}\frac{d}{dz}\left(\frac{\Pi^c m_z}{n}\right)\right)+(d-1)D_R m_z=0. \quad (4.100)$$

We first demonstrate that the correlation broadens the predicted binodal of MIPS of athermal ABPs. From eqs. (4.94), (4.96), and (4.100) we obtain

$$\Pi^{act}-\left[\frac{3U_0^2\overline{U}}{2d(d-1)(d+2)D_R^2}\frac{d}{dz}\left(\overline{U}\frac{d\Pi^c}{dz}\right)+\frac{\upsilon}{(d-1)\zeta D_R}\frac{d}{dz}\left(\frac{\Pi^c}{n}\frac{d\Pi^c}{dz}\right)\right]=c\ \text{(const.)}, \quad (4.101)$$

where Π^{act} is the active pressure defined as a sum of the swim pressure $\Pi^{swim}=n\zeta U_0^2\overline{U}/(d(d-1)D_R)$ and the collisional pressure Π^c, $\overline{U}\equiv\overline{U}_m=\overline{U}_Q$ is the reduction in speed of the convective transports, and c is an integration constant. Eq. (4.101) implies the equality of bulk active pressures for the phase coexistence. By virtue of the homogeneity of the phase, any spatial derivatives vanish inside a bulk region. Therefore the active pressure Π^{act} deep inside any of coexisting phases should be equally c i.e. the (undetermined) integration constant c is the coexistence active pressure which is denoted as Π^{act}_{coex} in the following. In the absence of the correlation ($\upsilon=0$) the collisional pressure gradient $d\Pi^c/dz$ serves as a integrating factor of eq. (4.101) and results in the generalized Maxwell construction on the Π^{act}-Π^c-plane as described in our main text. In order to investigate effects of the correlation term we apply the same procedure. Integrating eq. (4.101) from and to

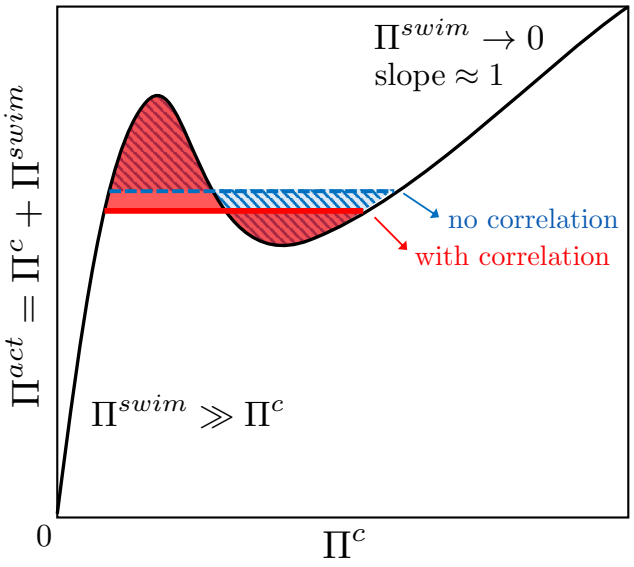

Figure 4.7: A schematic of Π^{act}-Π^c plot with a van-der Waals-like loop. The correlation between the collisional stress and orientation leads to $\int \Pi^{act} - \Pi^{act}_{coex}\, d\Pi^c > 0$ resulting in a drop in the coexistence active pressure.

bulk phases after multiplying it with $d\Pi^c/dz$ gives

$$\begin{aligned}\int_{\Pi^c_1}^{\Pi^c_2} \left[\Pi^{act} - \Pi^{act}_{coex}\right]\, d\Pi^c &= \frac{\upsilon}{2(d-1)\zeta D_R} \int_{\Pi^c_1}^{\Pi^c_2} \frac{n}{\Pi^c} \frac{d}{d\Pi^c} \left[\left(\frac{\Pi^c}{n}\frac{d\Pi^c}{dz}\right)^2\right] d\Pi^c \\ &= -\frac{\upsilon}{2(d-1)\zeta D_R} \int_{\Pi^c_1}^{\Pi^c_2} \frac{d}{d\Pi^c}\left(\frac{n}{\Pi^c}\right)\left(\frac{\Pi^c}{n}\frac{d\Pi^c}{dz}\right)^2 d\Pi^c \\ &= \frac{\upsilon}{2(d-1)\zeta D_R} \int_{\Pi^c_1}^{\Pi^c_2} \frac{d}{d\Pi^c}\left(\frac{\Pi^c}{n}\right)\left(\frac{d\Pi^c}{dz}\right)^2 d\Pi^c,\end{aligned} \tag{4.102}$$

where $\Pi^c_{1,2}$ are collisional pressures at the two points inside bulk phases and the second equation is obtained by performing the integration by parts. Since Π^c and Π^c/n are both monotonic increasing functions of the number density, the whole integrand inside the last integral is positive. The sign of the integral indicates the predicted coexistence active pressure should be lower with the collisional-stress-orientation correlation than without it as described in fig. 4.7. It follows that collisional pressures (or corresponding number densities) of the coexisting phases are also predicted to be smaller. Because the compressibility increases with the density, the effect of change in the collisional pressure on the corresponding density is larger for large density. Therefore, the decrease in the coexisting density is more prominent in the gas-like region while it is almost negligible for the dense region.

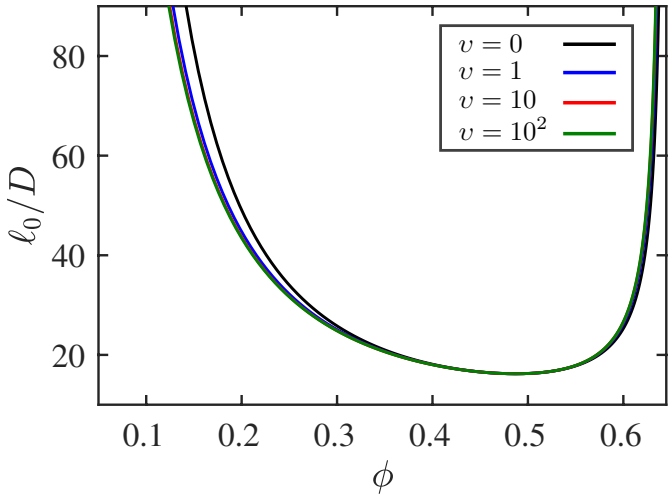

Figure 4.8: Binodals obtained by the mechanical theory for MIPS in 3D with the stress-orientation correlation $\upsilon\nabla\cdot(\boldsymbol{\sigma}^c\boldsymbol{m}/n)$ included in the polar order flux. Here, υ is a parameter used to systematically control the weight of the correlation term in the in the flux. The correlation between the stress and orientation increases the width of the binodal as predicted. However, the widening effect saturates rapidly even at $\upsilon = 1$.

Consequently, the predicted binodal on the activity-density plane has a broader binodal region due to the stretched gas-like branch in the presence of the collisional-stress-orientation correlation. Figure 4.8 shows that the correlation term broadens the binodal and confirms our prediction. The effect of the correlation between the stress and orientation saturates rapidly even at $\upsilon \approx 1$ and does not significantly alter the binodal.

References

[1] H. B. Callen, *Thermodynamics and an introduction to thermostatistics*, 1998.

[2] T. L. Hill, *Statistical mechanics: principles and selected applications*. Courier Corporation, 2013.

[3] M. Kardar, *Statistical physics of fields*. Cambridge University Press, 2007.

[4] J. Tailleur and M. Cates, "Statistical mechanics of interacting run-and-tumble bacteria," *Physical review letters*, vol. 100, no. 21, p. 218 103, 2008.

[5] M. E. Cates and J. Tailleur, "Motility-induced phase separation," *Annu. Rev. Condens. Matter Phys.*, vol. 6, no. 1, pp. 219–244, 2015.

[6] Y. Fily and M. C. Marchetti, "Athermal phase separation of self-propelled particles with no alignment," *Physical review letters*, vol. 108, no. 23, p. 235 702, 2012.

[7] J. Palacci, S. Sacanna, A. P. Steinberg, D. J. Pine, and P. M. Chaikin, "Living crystals of light-activated colloidal surfers," *Science*, vol. 339, no. 6122, pp. 936–940, 2013.

[8] S. A. Mallory, A. K. Omar, and J. F. Brady, "Dynamic overlap concentration scale of active colloids," *Physical Review E*, vol. 104, no. 4, p. 044 612, 2021.

[9] S. C. Takatori and J. F. Brady, "Towards a thermodynamics of active matter," *Physical Review E*, vol. 91, no. 3, p. 032 117, 2015.

[10] H. Row and J. F. Brady, "Reverse osmotic effect in active matter," *Physical Review E*, vol. 101, no. 6, p. 062 604, 2020.

[11] F. Schweitzer, W. Ebeling, and B. Tilch, "Complex motion of brownian particles with energy depots," *Physical Review Letters*, vol. 80, no. 23, p. 5044, 1998.

[12] W. Ebeling, F. Schweitzer, and B. Tilch, "Active brownian particles with energy depots modeling animal mobility," *BioSystems*, vol. 49, no. 1, pp. 17–29, 1999.

[13] P. Romanczuk, M. Bär, W. Ebeling, B. Lindner, and L. Schimansky-Geier, "Active brownian particles-from individual to collective stochastic dynamics p," *The European Physical Journal Special Topics*, vol. 202, 2012.

[14] S. C. Takatori and J. F. Brady, "Forces, stresses and the (thermo?) dynamics of active matter," *Curr. Opin. Colloid Interface Sci.*, vol. 21, pp. 24–33, Feb. 2016.

[15] S. C. Takatori and J. F. Brady, "Towards a thermodynamics of active matter," *Phys. Rev. E - Stat. Nonlinear, Soft Matter Phys.*, vol. 91, no. 3, p. 32 117, 2015.

[16] A. P. Solon, J. Stenhammar, M. E. Cates, Y. Kafri, and J. Tailleur, "Generalized thermodynamics of motility-induced phase separation: Phase equilibria, laplace pressure, and change of ensembles," *New Journal of Physics*, vol. 20, no. 7, p. 075 001, 2018.

[17] S. Paliwal, J. Rodenburg, R. van Roij, and M. Dijkstra, "Chemical potential in active systems: Predicting phase equilibrium from bulk equations of state?" *New Journal of Physics*, vol. 20, no. 1, p. 015 003, 2018.

[18] S. Hermann, P. Krinninger, D. de Las Heras, and M. Schmidt, "Phase coexistence of active brownian particles," *Physical Review E*, vol. 100, no. 5, p. 052 604, 2019.

[19] J. Guioth and E. Bertin, "Lack of an equation of state for the nonequilibrium chemical potential of gases of active particles in contact," *The Journal of Chemical Physics*, vol. 150, no. 9, p. 094 108, 2019.

[20] T. F. Farage, P. Krinninger, and J. M. Brader, "Effective interactions in active brownian suspensions," *Physical Review E*, vol. 91, no. 4, p. 042 310, 2015.

[21] A. P. Solon, M. E. Cates, and J. Tailleur, "Active brownian particles and run-and-tumble particles: A comparative study," *The European Physical Journal Special Topics*, vol. 224, no. 7, pp. 1231–1262, 2015.

[22] J. Tailleur and M. E. Cates, "Statistical mechanics of interacting run-and-tumble bacteria," *Phys. Rev. Lett.*, vol. 100, no. 21, p. 218 103, 2008.

[23] J. Stenhammar, A. Tiribocchi, R. J. Allen, D. Marenduzzo, and M. E. Cates, "Continuum theory of phase separation kinetics for active brownian particles," *Physical review letters*, vol. 111, no. 14, p. 145 702, 2013.

[24] R. Wittkowski, A. Tiribocchi, J. Stenhammar, R. J. Allen, D. Marenduzzo, and M. E. Cates, "Scalar $\varphi 4$ field theory for active-particle phase separation," *Nature communications*, vol. 5, no. 1, pp. 1–9, 2014.

[25] T. Speck, J. Bialké, A. M. Menzel, and H. Löwen, "Effective cahn-hilliard equation for the phase separation of active brownian particles," *Physical Review Letters*, vol. 112, no. 21, p. 218 304, 2014.

[26] J. W. Gibbs, "On the equilibrium of heterogeneous substances," 1879.

[27] J. v. Waals, "The thermodynamic theory of capillarity under the hypothesis of a continuous variation of density," *Journal of Statistical Physics*, vol. 20, no. 2, pp. 200–244, 1979.

[28] J. W. Cahn and J. E. Hilliard, "Free energy of a nonuniform system. i. interfacial free energy," *The Journal of chemical physics*, vol. 28, no. 2, pp. 258–267, 1958.

[29] A. J. Yang, P. D. Fleming III, and J. H. Gibbs, "Molecular theory of surface tension," *The Journal of Chemical Physics*, vol. 64, no. 9, pp. 3732–3747, 1976.

[30] D. Korteweg, "Archives neerl," *Sci. Exacts. Nat*, vol. 6, no. 1, 1904.

[31] E. C. Aifantis and J. B. Serrin, "The mechanical theory of fluid interfaces and maxwell's rule," *Journal of colloid and interface science*, vol. 96, no. 2, pp. 517–529, 1983.

[32] J.-P. Hansen and I. R. McDonald, *Theory of simple liquids: with applications to soft matter*. Academic press, 2013.

[33] J. Irving and J. G. Kirkwood, "The statistical mechanical theory of transport processes. iv. the equations of hydrodynamics," *The Journal of chemical physics*, vol. 18, no. 6, pp. 817–829, 1950.

[34] H. Davis and L. Scriven, "Stress and structure in fluid interfaces," *Advances in Chemical Physics*, vol. 49, pp. 357–454, 1982.

[35] J. G. Kirkwood and F. P. Buff, "The statistical mechanical theory of surface tension," *The Journal of Chemical Physics*, vol. 17, no. 3, pp. 338–343, 1949.

[36] A. K. Omar, Z.-G. Wang, and J. F. Brady, "Microscopic origins of the swim pressure and the anomalous surface tension of active matter," *Phys. Rev. E*, vol. 101, no. 1, p. 012 604, 2020.

[37] W. Noll, "The derivation of the fundamental equations of the thermomechanics of continua from statistical mechanics," *Journal of Rational Mechanics and Analysis*, vol. 4, pp. 627–646, 1955.

[38] R. B. Lehoucq and A. Von Lilienfeld-Toal, "Translation of walter noll's "derivation of the fundamental equations of continuum thermodynamics from statistical mechanics"," *Journal of Elasticity*, vol. 100, no. 1-2, pp. 5–24, 2010.

[39] W. Yan and J. F. Brady, "The force on a boundary in active matter," *Journal of Fluid Mechanics*, vol. 785, 2015.

[40] D. Saintillan and M. J. Shelley, "Theory of active suspensions," in *Complex Fluids in biological systems*, Springer, 2015, pp. 319–355.

[41] S. C. Takatori, W. Yan, and J. F. Brady, "Swim pressure: Stress generation in active matter," *Physical review letters*, vol. 113, no. 2, p. 028 103, 2014.

[42] J. M. Epstein, K. Klymko, and K. K. Mandadapu, "Statistical mechanics of transport processes in active fluids. ii. equations of hydrodynamics for active brownian particles," *The Journal of chemical physics*, vol. 150, no. 16, p. 164 111, 2019.

[43] H. H. Woodson and J. Melcher, *Electromechanical dynamics.(part2)*, 1968.

[44] A. Patch, D. M. Sussman, D. Yllanes, and M. C. Marchetti, "Curvature-dependent tension and tangential flows at the interface of motility-induced phases," *Soft matter*, vol. 14, no. 36, pp. 7435–7445, 2018.

[45] J. Bialké, J. T. Siebert, H. Löwen, and T. Speck, "Negative interfacial tension in phase-separated active brownian particles," *Physical review letters*, vol. 115, no. 9, p. 098 301, 2015.

[46] R. van Damme, J. Rodenburg, R. van Roij, and M. Dijkstra, "Interparticle torques suppress motility-induced phase separation for rodlike particles," *The Journal of Chemical Physics*, vol. 150, no. 16, p. 164 501, 2019. DOI: 10.1063/1.5086733.

[47] A. Wysocki, A. K. Dasanna, and H. Rieger, *Interacting particles in an activity landscape*, 2022. DOI: 10.48550/ARXIV.2204.01029.

[48] A. K. Omar, Y. Wu, Z.-G. Wang, and J. F. Brady, "Swimming to stability: Structural and dynamical control via active doping," *ACS nano*, vol. 13, no. 1, pp. 560–572, 2018.

[49] J. Stenhammar, R. Wittkowski, D. Marenduzzo, and M. E. Cates, "Activity-induced phase separation and self-assembly in mixtures of active and passive particles," *Physical review letters*, vol. 114, no. 1, p. 018 301, 2015.

[50] P. Dolai, A. Simha, and S. Mishra, "Phase separation in binary mixtures of active and passive particles," *Soft Matter*, vol. 14, no. 29, pp. 6137–6145, 2018.

[51] P. Hohenberg and W. Kohn, "Inhomogeneous electron gas," *Physical review*, vol. 136, no. 3B, B864, 1964.

[52] N. D. Mermin, "Thermal properties of the inhomogeneous electron gas," *Physical Review*, vol. 137, no. 5A, A1441, 1965.

[53] R. Evans, "The nature of the liquid-vapour interface and other topics in the statistical mechanics of non-uniform, classical fluids," *Advances in physics*, vol. 28, no. 2, pp. 143–200, 1979.

[54] Y. Rosenfeld, "Free-energy model for the inhomogeneous hard-sphere fluid mixture and density-functional theory of freezing," *Physical review letters*, vol. 63, no. 9, p. 980, 1989.

[55] L. Tonks, "The complete equation of state of one, two and three-dimensional gases of hard elastic spheres," *Physical Review*, vol. 50, no. 10, p. 955, 1936.

[56] A. Poncet, O. Bénichou, V. Démery, and D. Nishiguchi, "Pair correlation of dilute active brownian particles: From low-activity dipolar correction to high-activity algebraic depletion wings," *Physical Review E*, vol. 103, no. 1, p. 012 605, 2021.

[57] J. K. Dhont, G. W. Park, and W. Briels, "Motility-induced inter-particle correlations and dynamics: A microscopic approach for active brownian particles," *Soft matter*, vol. 17, no. 22, pp. 5613–5632, 2021.

[58] A. Patch, D. Yllanes, and M. C. Marchetti, "Kinetics of motility-induced phase separation and swim pressure," *Physical Review E*, vol. 95, no. 1, p. 012 601, 2017.

[59] S. Das, G. Gompper, and R. G. Winkler, "Local stress and pressure in an inhomogeneous system of spherical active brownian particles," *Scientific reports*, vol. 9, no. 1, pp. 1–11, 2019.

[60] T. Speck, "Coexistence of active brownian disks: Van der waals theory and analytical results," *Physical Review E*, vol. 103, no. 1, p. 012 607, 2021.